3D freeze printing of functional aerogels

by

Halil Tetik

B.S., Izmir Institute of Technology, 2013
M.S., Izmir Institute of Technology, 2016

AN ABSTRACT OF A DISSERTATION

submitted in partial fulfillment of the requirements for the degree

DOCTOR OF PHILOSOPHY

Department of Industrial and Manufacturing Systems Engineering
Carl R. Ice College of Engineering

KANSAS STATE UNIVERSITY
Manhattan, Kansas

2022

Abstract

Aerogels are a class of highly porous materials made from almost any material compositions. The exotic properties of the aerogels including low thermal conductivity, transparency, flexibility, extremely high porosity, low weight and density, large surface area, etc. attracted the attention of many researchers working in various fields. Incorporating 3D printing technology in aerogel fabrication provided a great freedom in the design of the final product as well as a great capability of tailoring the materials properties. Yet, the 3D printing methods used for fabrication of aerogels suffer from the printability requirements, lack of appropriate support material that can be removed without harsh chemical/thermal post-processes, and lack of ability to simultaneously engineer the macrostructure of the aerogels along with their microstructure. 3D Freeze Printing (3DFP), developed by our group, has shown a great promise to address those issues in our previous studies. However, our group's previous process investigation studies relied on only optical imaging techniques, which provided information on the material deposition, but not the solidification step. This limits the depth of information that we have about the process since solidification is a very important step. Besides, feasible materials for 3DFP method were limited with graphene and silver nanowires. Considering the wide range of materials used for 3D printed aerogels, different materials need to be introduced to 3DFP method to realize its full potential in the area. In addition, , a fully functioning device using 3DFP method has never been built and evaluated for its performance compared to the devices fabricated by other methods. Moreover, there is a need for a fabrication method which can fabricate aerogels with non-monolithic predesigned microstructures (e.g. pores of various sizes located in certain regions of the aerogels), especially for applications in the field of controlled drug-delivery, bone tissue engineering, selective liquid sorption, and so on.

In this thesis, based on the motivation listed above, 3DFP method has been studied in the course of realizing its full potential in the field. Firstly, a process investigation has been performed to simultaneously observe the material deposition and solidification (freezing) using the sophisticated X-ray imaging facilities in SLAC National Accelerator Laboratory. This investigation helped to develop a mathematical model for the geometry of the deposited material, observe the material deposition and solidification concurrently, and understand the effects of different process parameters (e.g. jetting frequency, print head speed, and substrate temperature) on the phase change as well as the quality of the printed constructs. Then, aerogels based on novel materials (cellulose nanocrystals (CNC) and MXenes) for 3DFP method were fabricated and characterized. By incorporating different additives in the ink formulation, different functionalities have been achieved for 3D printed CNC aerogels. Functional devices were developed using the 3D printed MXene aerogels, an enhancement in their performance was achieved by engineering the microstructure, and eventually their performance was compared with other reported devices fabricated by different methods. Finally, a novel method for fabrication of aerogels having non-monolithic micropore morphologies was developed. By achieving local temperature gradients on the substrate used for unidirectional freeze casting and 3DFP processes, a predesigned microstructure where the location of large and small pores can be precisely controlled is obtained. This method has a great potential for applications such as drug delivery, bone tissue engineering, photo catalysis, selective absorption, etc. where a predesigned non-monolithic micropore morphology can be an asset.

3D freeze printing of functional aerogels

by

Halil Tetik

B.S., Izmir Institute of Technology, 2013
M.S., Izmir Institute of Technology, 2016

A DISSERTATION

submitted in partial fulfillment of the requirements for the degree

DOCTOR OF PHILOSOPHY

Department of Industrial and Manufacturing Systems Engineering
Carl R. Ice College of Engineering

KANSAS STATE UNIVERSITY
Manhattan, Kansas

2022

Approved by:

Major Professor
Dr. Dong Lin

Copyright

Abstract

Aerogels are a class of highly porous materials made from almost any material compositions. The exotic properties of the aerogels including low thermal conductivity, transparency, flexibility, extremely high porosity, low weight and density, large surface area, etc. attracted the attention of many researchers working in various fields. Incorporating 3D printing technology in aerogel fabrication provided a great freedom in the design of the final product as well as a great capability of tailoring the materials properties. Yet, the 3D printing methods used for fabrication of aerogels suffer from the printability requirements, lack of appropriate support material that can be removed without harsh chemical/thermal post-processes, and lack of ability to simultaneously engineer the macrostructure of the aerogels along with their microstructure. 3D Freeze Printing (3DFP), developed by our group, has shown a great promise to address those issues in our previous studies. However, our group's previous process investigation studies relied on only optical imaging techniques, which provided information on the material deposition, but not the solidification step. This limits the depth of information that we have about the process since solidification is a very important step. Besides, feasible materials for 3DFP method were limited with graphene and silver nanowires. Considering the wide range of materials used for 3D printed aerogels, different materials need to be introduced to 3DFP method to realize its full potential in the area. In addition, , a fully functioning device using 3DFP method has never been built and evaluated for its performance compared to the devices fabricated by other methods. Moreover, there is a need for a fabrication method which can fabricate aerogels with non-monolithic predesigned microstructures (e.g. pores of various sizes located in certain regions of the aerogels), especially for applications in the field of controlled drug-delivery, bone tissue engineering, selective liquid sorption, and so on.

In this thesis, based on the motivation listed above, 3DFP method has been studied in the course of realizing its full potential in the field. Firstly, a process investigation has been performed to simultaneously observe the material deposition and solidification (freezing) using the sophisticated X-ray imaging facilities in SLAC National Accelerator Laboratory. This investigation helped to develop a mathematical model for the geometry of the deposited material, observe the material deposition and solidification concurrently, and understand the effects of different process parameters (e.g. jetting frequency, print head speed, and substrate temperature) on the phase change as well as the quality of the printed constructs. Then, aerogels based on novel materials (cellulose nanocrystals (CNC) and MXenes) for 3DFP method were fabricated and characterized. By incorporating different additives in the ink formulation, different functionalities have been achieved for 3D printed CNC aerogels. Functional devices were developed using the 3D printed MXene aerogels, an enhancement in their performance was achieved by engineering the microstructure, and eventually their performance was compared with other reported devices fabricated by different methods. Finally, a novel method for fabrication of aerogels having non-monolithic micropore morphologies was developed. By achieving local temperature gradients on the substrate used for unidirectional freeze casting and 3DFP processes, a predesigned microstructure where the location of large and small pores can be precisely controlled is obtained. This method has a great potential for applications such as drug delivery, bone tissue engineering, photo catalysis, selective absorption, etc. where a predesigned non-monolithic micropore morphology can be an asset.

Table of Contents

List of Figures

List of Tables

Acknowledgements

I would love to thank all the professors, graduate students, and researchers who helped me to conduct this research. I would love to present my special thanks to my supervisor, Dr. Dong Lin, for his support, and believing in me. Without his guidance, this work wouldn't be possible. In addition, I would love to present my gratitude to my lab mates Pedram Parandoush, Guang Yang, Keren Zhao, and Nasrullah Shah for their companionship as well as help with the experiments. I would love to thank Shuting Lei, Johanna Nelson Weker, Jafar Orangi, Majid Beidaghi, Gurpreet Singh, Shakir Bin Mujib, Fang Qian, Ying Wang, Hongli Zhu, Samuel Oxandale, Dan Feng and Zayd Leseman for their help and collaborations. I am also grateful for the guidance and support of my supervisory committee members Shuting Lei, Suprem R. Das, Shing I. Chang, Gurpreet Singh, and Byungsoo Kimi. I would love to present my sincere appreciation to my parents for being such supportive with my studies and my life. I also would love to acknowledge the financial support from Turkish Ministry of National Education.

Dedication

I dedicate this dissertation to the love of my life and to the bright future of our baby girl. Without your support and love, this would not be possible.

Chapter 1 - Introduction

Aerogels are a class of highly porous materials fabricated by replacing the liquid of a gel by air without causing a collapse of the solid network. The term was introduced by Kistler in 1931[1] when he discovered the first aerogels after a supercritical fluid drying of silica gels. The exotic properties of the aerogels including low thermal conductivity, transparency, flexibility, extremely high porosity, low weight and density, large surface area, high mechanical strength, ultralow dielectric constant, and etc. attracted the attention of many researchers working in various fields.[2] Since then, aerogels made from almost any kind of material compositions, including but not limited to metals[3], ceramics[4], biopolymers[5], and etc., have shown great promise for a variety of advanced applications such as energy storage[6], biomedical[2], thermal insulation[7], sensing[8], and so on. The synthesis of aerogels typically involves three key steps: (i) gelling step where the formation of a gel by sol–gel chemistry is achieved; (ii) aging step for the reinforcement of the gel solid network; and (iii) drying step to remove the liquid solvent without collapse.[9] Collapse-free drying of the gels has been commonly achieved through supercritical fluid drying, freeze-drying, and ambient temperature drying methods. The method used for drying of the gels without causing a collapse of the solid network is of high importance since it dictates pore dimensions and their overall textural properties.[10] Among all, freeze-drying, which was incorporated by the commonly used freeze casting method, provides variable tools to engineer the microstructure of the fabricated aerogels.

Various additive manufacturing (AM) technologies followed by an appropriate drying method has been used for fabrication of aerogels to achieve:

- Fast and accurate fabrication complex 3D constructs.
- Customized chemistry and architecture.

- Tailored and/or optimized physical properties.
- Hierarchical porosity ranging from a few hundreds of nanometers to a few millimeters.
- Different functionalities by precisely engineering structure.

The most commonly used AM technology for 3D printing of aerogels is an extrusion-based method known as direct-ink-writing. With this method, the ink, mostly in the form of gel, is selectively deposited to obtain complex 3D geometries. For the printability of the ink, the gel needs to have a shear-thinning rheology which allows the gel to be extruded from the micro-sized needle and then keep its shape after deposition. The other AM technology that has been used for 3D printing of aerogels is stereolithography, and this technology requires a liquid resin with a photo-curable chemistry for a selective solidification. The printability requirements of both methods has been a limiting factor on the range of materials, as well as the density of the final products. Besides, due to lack of an appropriate support material that can be removed from the constructs without using harsh chemical and thermal post-processes, 3D printed aerogels has always had a constant cross-sectional geometry, which limited the freedom in design and fabrication of highly irregular geometries. Furthermore, even though the AM technology provided a great capability to engineer the macro geometry of the fabricated aerogels, a simultaneous control over the microstructure that can help to engineer the materials properties is still missing.

3D Freeze Printing (3DFP) method[11,12], which was developed by our group at Kansas State University with our collaborators from University at Buffalo and Harbin Institute of Technology, has shown a great potential to address the aforementioned issues in the field of 3D printed aerogels. In the previous reports of our group[13, 14], the process investigation studies relied on only optical imaging techniques, which provided information on the material deposition, not

the solidification. This limits the depth of information that we have about the process dynamics since solidification is a very important step of the 3DFP method as well as additive manufacturing in general. Besides, the range of materials that has been proven to be feasible for 3DFP was limited to graphene[11] and silver nanowires[12]. Although fabricated aerogels (based on graphene and silver nanowires) showed promising properties for applications such as electronics, heat conduction, sensing, catalysis, energy storage, and shock damping, a functioning device has never been built and evaluated for its performance compared to the devices fabricated by other fabrication methods. In addition, freeze casting based methods (including 3DFP) can provide a good control over the micropore morphology of the final aerogel by manipulating the freezing kinetics. However, this control cannot achieve a non-monolithic predesigned microstructure (e.g. pores of various sizes located in certain regions of the aerogels), which is highly desirable by applications such as controlled drug-delivery, bone tissue engineering, selective liquid sorption, and so on.

This dissertation aims to study 3DFP method for realization of functional aerogels where the macro and microstructure of the final product can simultaneously be engineered for novel functionalities and/or enhanced performance. Based on the motivation provided above, objectives of the dissertation have been set as follows:

1. Investigation of the 3DFP process to develop a model for the deposited material, obtain quality information for phase change (solidification) along the layer and at the layer boundaries, and determine the effects of printing parameters on the quality of final product.
2. Fabrication of 3D printed aerogels using novel materials for the process, and achieving highly irregular geometries which cannot be possible by other fabrication

methods, and investigation of the effects of the microstructure on the physical properties.

3. Development of functional devices based on 3D freeze printed aerogels where the microstructure is precisely engineered to enhance the device performance.
4. Development of a novel method for fabrication of aerogels that are composed of non-monolithic predesigned micropore morphologies.

This dissertation consists of seven chapters. After a brief introduction in Chapter 1, the current literature on additive manufacturing of aerogels and porous scaffolds is presented in Chapter 2. The details of the 3DFP process as well as the studies for *in-situ* process investigation and process modelling are presented in Chapter 3. In this chapter, the results of the *in-situ* X-ray imaging experiments, which provide information of both material deposition and solidification, are presented. This chapter addresses the 1st objective of this thesis. In Chapters 4 and 5, novel materials, cellulose nanocrystals and $Ti_3C_2T_x$ MXene, are introduced to the 3DFP method. Chapter 4 discusses 3D freeze printed cellulose nanocrystal aerogels, and their functionalization with different additives. The effects of the process anisotropy on the mechanical properties of the 3D printed aerogels have also been investigated. Chapter 5 presents the studies performed for obtaining functional devices based on 3D freeze printed MXene aerogels, and methods used for tailoring the microstructure of the all-printed functional devices to enhance their performance. Chapters 4 and 5 address objectives 2 and 3 simultaneously. Chapter 6, which covers objective 4, discusses the systematic studies performed to achieve a precise control over the microstructure of the aerogels to obtain non-monolithic predesigned pore textures. Finally, Chapter 7 concludes the dissertation with a summary, and outlook to the field of additive manufacturing of aerogels.

References

[1] Kistler, S.S., Coherent expanded aerogels and jellies. Nature, 1931. 127(3211): p. 741-741.

[2] Stergar, J. and U. Maver, Review of aerogel-based materials in biomedical applications. Journal of Sol-Gel Science and Technology, 2016. 77(3): p. 738-752.

[3] Tang, Y., K.L. Yeo, Y. Chen, L.W. Yap, W. Xiong, and W. Cheng, Ultralow-density copper nanowire aerogel monoliths with tunable mechanical and electrical properties. Journal of Materials Chemistry A, 2013. 1(23): p. 6723-6726.

[4] Zu, G., J. Shen, X. Wei, X. Ni, Z. Zhang, J. Wang, and G. Liu, Preparation and characterization of monolithic alumina aerogels. Journal of non-crystalline solids, 2011. 357(15): p. 2903-2906.

[5] Zhao, S., W.J. Malfait, N. Guerrero-Alburquerque, M.M. Koebel, and G. Nyström, Biopolymer aerogels and foams: Chemistry, properties, and applications. Angewandte Chemie International Edition, 2018. 57(26): p. 7580-7608.

[6] Chhetri, K., S. Subedi, A. Muthurasu, T.H. Ko, B. Dahal, and H.Y. Kim, A review on nanofiber reinforced aerogels for energy storage and conversion applications. Journal of Energy Storage, 2022. 46: p. 103927.

[7] Hasan, M.A., R. Sangashetty, A.C.M. Esther, S.B. Patil, B.N. Sherikar, and A. Dey, Prospect of thermal insulation by silica aerogel: a brief review. Journal of The Institution of Engineers (India): Series D, 2017. 98(2): p. 297-304.

[8] Amonette, J.E. and J. Matyáš, Functionalized silica aerogels for gas-phase purification, sensing, and catalysis: A review. Microporous and Mesoporous Materials, 2017. 250: p. 100-119.

[9] Lamy-Mendes, A., R.F. Silva, and L. Durães, Advances in carbon nanostructure–silica aerogel composites: a review. Journal of Materials Chemistry A, 2018. 6(4): p. 1340-1369.

[10] Linhares, T., M.T.P. de Amorim, and L. Durães, Silica aerogel composites with embedded fibres: a review on their preparation, properties and applications. Journal of Materials Chemistry A, 2019. 7(40): p. 22768-22802.

[11] Zhang, Q., F. Zhang, S.P. Medarametla, H. Li, C. Zhou, and D. Lin, 3D printing of graphene aerogels. Small, 2016. 12(13): p. 1702-1708.

[12] Yan, P., E. Brown, Q. Su, J. Li, J. Wang, C. Xu, C. Zhou, and D. Lin, 3D printing hierarchical silver nanowire aerogel with highly compressive resilience and tensile elongation through tunable poisson's ratio. Small, 2017. 13(38): p. 1701756.

[13] Zhang, F., F. Yang, D. Lin, and C. Zhou, Parameter study of three-dimensional printing graphene oxide based on directional freezing. Journal of Manufacturing Science and Engineering, 2017. 139(3): p. 031016.

[14] Zhao, G., D. Lin, and C. Zhou, Thermal analysis of directional freezing based graphene aerogel three-dimensional printing process. Journal of Micro and Nano-Manufacturing, 2017. 5(1).

Chapter 2 - Literature Review[1]

The concept of aerogel, that designates gels in which the liquid is replaced by a gas without collapse of the gel solid network, was first introduced by Kistler in 1931.[1] When wet gels are dried by evaporation in ambient conditions, the gel shrinks and the solid net- work collapses due to the formation of liquid–vapor meniscuses at the gel pores, which creates a mechanical tension in the pore walls. Kistler's pioneering study showed that at the supercritical conditions for the liquid impregnated in the gel, the distinction between liquid and gas state as well as liquid–vapor meniscuses at the gel pores is eliminated, and gels can be dried with a very porous texture similar to the one in the wet stage without a col- lapse in the solid network.[2] Their unique microstructure in the form of pores (at the nanometer to micrometer scale) along with solid-particle mesh network provides many exotic properties such as the lowest thermal conductivity, refractive index, sound velocity, and dielectric constant measured on any solid. The density of the aerogels can even be lower than air while they exhibit fixed volumes and shapes as solid materials.[3] Since the discovery of silica aerogel by Kistler, various materials including metals,[4,5] ceramics,[6,7] polymers,[8,9] biomaterials,[10,11] and many more have been used to synthesize aerogels. Aerogels have been used in biomedical and pharmaceutical applications, electrical devices and energy storage systems, thermal insulators, fire retarders, and many other fields.[12–15]

Additive manufacturing (AM), also known as rapid prototyping or 3D printing, is the process of depositing materials layer by layer to make objects directly from 3D model data.[16,17] Since the invention of stereolithography, which was the first form of 3D printing introduced by

[1] Reprinted with permission from "Additive Manufacturing of 3D Aerogels and Porous Scaffolds: A Review" by Halil Tetik, Ying Wang, Xiao Sun, Daxian Cao, Nasrullah Shah, Hongli Zhu, Fang Qian, Dong Lin, 2021. Advanced Functional Materials, 31, 2103410. 2021 Wiley-VCH GmbH

Charles Hull in the 1980s, other techniques such as selective laser sintering, fused deposition modeling, laminated object manufacturing, electron beam melting, and many more have been developed to additively manufacture 3D objects.[18] In general, AM process starts with designing a 3D geometric model using computer aided design (CAD) software. The CAD file is then converted into a standard triangulation language (STL) file format, which is a standard input for almost all 3D printing systems. The STL file is imported into 3D printing software to adjust printing parameters and object orientation, followed by slicing the object geometry at a distance equal to layer thickness. This information is transferred to the 3D printing system to be used for AM of the part. Finally, the required post-processes such as cleaning of the object, removal of support material, and surface treatment are applied.[19]

Typical fabrication process of the aerogels consists of three key steps including solution–sol, sol–gel, and gel–aerogel transitions.[20,21] Briefly, precursor materials are dispersed in a liquid medium to obtain sol; then, depending on the nature of precursor material, transition from sol to gel is achieved via different strategies. Some materials also may require additional curing to provide mechanical strength to the aerogel network. Finally, by incorporating an appropriate drying method such as supercritical fluid drying (SCFD), freeze drying (FD), or ambient-temperature drying (AD), the gel is dried without causing a collapse in the aerogel network. Incorporating AM techniques during solution–sol or sol–gel transition steps have revolutionized the field by introducing fast and accurate fabrication of complex 3D structures.[22] Besides, AM also provided the capability of device fabrication with customized chemistry and architecture.[23] Furthermore, tuning the 3D printing parameters has been efficiently used for tailoring and optimizing the physical properties of the final aerogels.[24] The hierarchical porosity obtained after 3D printing followed by an appropriate drying method enhanced the performance of the 3D-printed

aerogels and scaffolds in many applications such as tissue engineering (TE),[25] electrochemical energy storage,[26] pollutant removal from water,[27] etc. The ability to construct sophisticated gradient structures have been proven to be beneficial for sensors and actuators.[28] Further advantages of the 3D printing over the conventional methods for aerogel fabrication are discussed later for each application.

3D Printing Methods

Additive manufacturing process of aerogels includes steps of ink synthesis, 3D printing, drying, and post-processing. 3D printing process is completed in either solution–sol or sol– gel transition steps: inks or resins in the form of solution or sol are selectively deposited or solidified to obtain gels with desired geometries. There are three main techniques used: extrusion-based printing (EBP), inkjet-based printing (IBP), and stereolithography (SLA). EBP utilizes paste-like inks with shear-thinning behavior, which are extruded through a nozzle in the form of filaments with sufficient strength to preserve their shape.[29] IBP, unlike EBP, is capable of working with Newtonian inks with relatively low viscosities. The ink is deposited in the form of droplets and needs to be solidified to keep its shape.[30] In SLA, a resin containing a photocurable material is solidified by a guided laser to achieve solidification in desired geometry.[31] Once the gels with desired geometries are 3D-printed using one of the aforementioned strategies, an appropriate drying method (SCFD, AD, or FD) that does not cause a collapse or structural damage in the solid network is applied to obtain aerogels. Finally, required post-processes are applied to provide (structural integrity), functionality, or both to the aerogels.

Typically, EBP requires inks with either high solid loading or rheology modifying agents to achieve shear-thinning behavior. In case of inks with high solid loading, 3D-printed aerogels have relatively higher densities, and accordingly, higher mechanical strengths. In case of inks with

rheology modifiers, post-drying thermal or chemical processes are applied to etch the modifiers from the structure. On the other hand, IBP can deposit Newtonian inks with relatively lower viscosity and solid loading. As a result, this process is able to achieve ultralow densities. Furthermore, with IBP, water has been used as support material to obtain 3D-printed aerogels with overhang features, which can increase the freedom in design. In contrast to EBP and IBP, SLA provides a selective solidification/gelation instead of selective material deposition. To achieve 3D-printed aerogels with SLA printing, a resin containing a monomer, a photoinitiator, and the main material of interest must be synthesized. Even though the SLA provides the lowest resolution (≈10 µm[32]) in the 3D printing process, the monomer and the photoinitiator needs to be removed from the final structure by post-processing.

EBP is the most commonly used technique for 3D print of aerogels, and this method has been used with ink formulations based on a wide range of materials. For instance, Xiong *et al.* used EBP to fabricate porous scaffolds made from biocompatible synthetic polymers for bone tissue engineering applications in 2002.[33] After this study, natural polymers such as chitosan,[34] collagen,[35] and cellulose[36] were used for fabricating biomedical devices. In 2015, graphene oxide (GO), which is one of the most common materials for 3D-printed aerogels, was used to fabricate reduced graphene oxide (rGO) aerogels.[37] Following that, an ink formulation based on pristine graphene was reported.[38] In 2018, an ink formulation based on resorcinol–formaldehyde (R-F) was developed, and 3D-printed R-F aerogels were used as precursor for carbon aerogels.[39] In 2019, MXenes, which are another 2D material like graphene, were used to 3D-printed aerogels for electrochemical energy storage applications.[40] In the same year, 3D-printed hydroxyapatite (HAP) scaffolds with hierarchical and interconnected pore morphologies were proposed for bone tissue engineering applications.[41] The list of materials tested with IBP

and SLA to fabricate 3D-printed aerogels is relatively limited when compared to EBP. The first study that reported 3D-printed silica aerogels using SLA was published in 2015.[42] Following that, SLA was used to fabricate 3D-printed aerogels made from chitosan[43] and rGO.[32] In 2016, the first aerogel that has truly 3D geometry with overhang truss features was fabricated from rGO using IBP.[30] Following that, using the same method, silver nanowire (AgNWs)[44] and composites of rGO[45] were used to synthesize inks for 3D printing of functional aerogels.

Extrusion-based 3D Printing

EBP is the most common 3D printing method to fabricate aero- gels with customized geometries. The ink used for EBP must possess a shear-thinning behavior, which enables flow of the high viscosity ink through the nozzle by a significant reduction in the ink's viscosity due to applied pressure. According to the power law of Ostwald and de Waele, the viscosity of a fluid can be defined as a function that is proportional to some power of the shear rate can be defined as[46]:

$$\eta = k \cdot \gamma^{n-1} \tag{2-1}$$

where η is the viscosity, k is consistency factor, n is the viscosity exponent, and γ is shear rate. For Newtonian inks, the value of the viscosity exponent is $n = 1$, whereas its value is $n < 1$ for the inks with shear-thinning behavior. Shear-thinning behavior of the ink is typically characterized from a plot showing the change in the apparent viscosity of the ink as a function of shear rate. The rapid decrease observed in the viscosity as the shear rate increases indicates that at rest, the ink has a stable solid-like structure, while with the applied shear rate, it behaves like fluid.[41] Furthermore, for the ink to be able to resist deformation after deposition, it must be viscoelastic with a sufficient yield stress. The viscoelastic inks are characterized by their complex shear modulus, $G^* = G' + iG''$, where G' is the storage modulus and G'' is the loss modulus.[47] The gelation point

for an ink can be defined by $G^{"}/G'$; when $G^{"}/G' < 1$, the ink has a solid-like behavior whereas $G^{"}/G' > 1$ refers to a liquid-like behavior. The viscoelastic behavior of the inks used for EBP are typically characterized using a plot that shows the storage and loss moduli as a function of shear stress. Accordingly, as the shear stress passes a yield (gelation) point, the storage moduli (G') becomes lower than the loss moduli ($G^{"}$) ($G^{"}/G' > 1$), which indicates a primary viscous (liquid-like) behavior of the ink. With low shear stress values, the storage moduli becomes higher than the loss moduli ($G^{"}/G' < 1$) representing an elastic (solid-like) behavior.[48]

Materials with high aspect ratio and surface charge can be used to tune the rheological properties for wet processing.[49] Similarly, there are several 3D-printed aerogels whose ink formulations are based on highly charged carboxymethylated cellulose nanofiber (CNF),[50] GO[26,51], and titanium carbide ($Ti_3C_2T_x$)[40] where no additives were required to achieve a good shear-thinning behavior. On the other hand, there are also proposed approaches to provide/enhance printability to suspensions of host materials. For instance, Song *et al.* used hydroxypropyl methyl cellulose (HPMC) as viscosifier, 1-octonal as defoamer, and polyethyleneimine as gelation agent for hydroxyapatite suspension to provide printability.[41] Chandrasekaran *et al.* proposed to use HPMC and fumed silica to boost the viscosity and storage modulus of R-F-based ink.[52] Jiang *et al.* incorporated $CaCl_2$ as crosslinker for GO- based inks to enhance the storage modulus and printability.[53] To enhance the materials properties and provide functionalities to the aerogels, it is also possible to use additives in the ink formulations without having a major effect on printability. Accordingly, xyloglucan was proposed as binder for cellulose nanocrystal (CNC),[54] polyamide-epichlorohydrin was used as strength additive for CNC[55] and CNF,[56] carbon nanotube (CNT) was used as a functionalization agent for CNF,[50] lithium iron phosphate and lithium titanium oxide

were used as cathode and anode active materials for GO,[57] SnO_2 quantum dots (QDs) were used as electrochemical performance additive for GO,[48] and manganese dioxide nanowires (MONWs), AgNWs, and fullerene was proposed to enhance capacitance, charge delivery, and mechanical properties of $Ti_3C_2T_x$-based aerogels.[58]

To extrude the ink from the nozzle, either a pneumatic air pressure, a mechanical piston, or a screw-based deposition system is used. Pneumatic air pressure is a simple and highly used technique; however, the accuracy of the deposition relies on the physical properties of the ink. Even though mechanical piston or screw-driven systems require relatively complex setups, they provide a large deposition force, which makes them suitable for inks with higher viscosities, and better control on the material deposition rate.[29] Accordingly, a vast majority of the studies on 3D-printed aerogels using EBP uses pneumatic pressure driven extrusion setups. Only a few studies incorporate mechanical[24,51,54,59–66] and screw-based[33,67,68] extrusion systems among more than 50 studies that report 3D-printed aerogels using an EBP setup. Commonly, ink formulations are water-based, and they do not require elevated temperatures to achieve material extrusion as in fused deposition modelling. However, when solvents with higher melting points such as 1,4 dioxane,[59] *N*-methylmorpholine-*N*-oxide,[69] *tert*-butanol,[62] phenol, or camphene[38] are used, temperature control on the ink is required to be able to extrude the material in the form of a uniform filament.

Deposited inks with proper shear-thinning behavior provided with sufficient storage modulus are able to hold their shape. However, there are ink formulations, which require extra gelation/solidification to preserve their shapes and structural integrity. Ge *et al.* reported that spraying a hydrochloric acid solution on the R-F-based ink after deposition helped them to be more self-supportive.[39] Similarly, Rees *et al.* pipetted $CaCl_2$ onto some of the layered constructs to fix CNC-

based ink by ionic crosslinking.[36] Zhu *et al.* deposited GO-based inks inside isooctane to prevent structural shrinkage and drying of the deposited ink in air before complete printing.[70,71] To keep the deposited structure wet during the printing process, Chandrasekaran *et al.* used an organic solvent (2,2,4-trimethyl-pentane) for 3D printing of RF organic aerogels. He *et al.* investigated three printing routes, including depositing in air, $CaCl_2$–glycerol solution (cross-linking medium), and pluronic F127 triblock (supporting reservoir) for 3D printing carbon nitride-based aero- gels. It was reported that printing inside $CaCl_2$–glycerol solution provided an ionic crosslinking for sodium alginate (SA), which was used as stabilizer and disperser in the ink formulation. This crosslinking provided a sufficient bonding force for filaments in the adjacent layers. In the third route, aqueous pluronic F127 triblock copolymer, which can undergo a thermo-reversible micellization process depending on both concentration and temperature, was used to induce a reversible fluid-to-gel transition. At the ambient temperature, where the deposition took place, a pluronic F127 gel matrix was used as a supporting reservoir. After 3D printing is completed, the pluronic F127 reservoir can be washed away with deionized water at 4 °C where pluronic F127 is a liquid.[72] Apart from using inks with sufficient storage modulus and/or inducing a crosslinking mechanism after the material deposition, performing the 3D printing process inside a cryogenic environment provides a fast solidification, which fixes the deposited material.[34,67,73] While 3D printing inside a cryogenic environment leads to isotropic freezing, which is similar to freeze casting[74] without mold, performing the material deposition on top of a precooled substrate is equivalent to unidirectional freeze casting.[75] Depositing the material on top of a cooled substrate fixes the ink due to rapid freezing and results in an aligned porosity along the freezing direction (from bottom to top), which is a beneficial property for tissue engineering scaffolds,[35,41,59,76,77] and energy applications.[58]

The solid strands obtained after material deposition are the building blocks of the 3D printing process, which determines the manufacturing time and resolution.[78] For EBP, the strand geometry is a function of nozzle diameter, ink rheology, and print-head speed.[79] Accordingly, Munir *et al.* investigated the dependency of the strand diameter on nozzle size, ink concentration, and print head temperature for 3D printing of polycaprolactone (PCL) scaffolds.[59] Since their process included material deposition on a freezing substrate, Kim *et al.* provided an experiment to show the effects of the substrate temperature on the size and uniformity of collagen strands.[35] The same group also investigated the relationship between strand diameter and fabrication conditions (print-head speed and substrate temperature) for fabricating chitosan aerogel scaffolds.[25] Geometrical investigation of the extruded strands can be very important for the aerogels since the pore size and porosity of the final product are influenced by the strand geometry.[35] Li *et al.* increased the scale and investigated the quality of cellulose-based aerogels instead of individual strands. They investigated the dependency of dimensional accuracy and smoothness of the aerogel surfaces on nozzle size and ink concentrations.[55]

Inkjet-Based 3D Printing

Inkjet printing, specifically drop-on-demand (DOD) printing, relies on pressure pulses to generate droplets from the ink. The method used to create pressure pulses defines the type of the print-head, such as piezoelectric, solenoid valve, thermal acoustic, electrostatic, and electrohydrodynamic.[80] Among those, the first two are employed to 3D print aerogels. Briefly, piezoelectric inkjet heads create a pressure wave by deforming a piezoelectric transducer located in the nozzle applying a voltage. With the increasing pressure inside the nozzle, a stream of liquid droplets is generated.[81] Solenoid valve inkjet heads operate through an internal piston, which

forces the valve to open and close via an induced magnetic field.[82] Once the piston is actuated and the valve is opened, pressurized ink moves to the orifice and is ejected as droplets.[83] An electrical pulse, whose length determines the opening time of the valve, is used to actuate the piston that allows or blocks ink flow.[84,85]

For IBP, the ink with a relatively low viscosity is dispensed in the form of spherical droplets on the substrate. The rheological requirements for printability of an ink are determined by Reynolds, Weber, and Ohnesorge numbers, which are dimensionless numbers related to the physical properties of the ink such as viscosity, surface tension, and density[86–89]:

$$Re = \frac{\upsilon \rho L}{\eta} \tag{2-2}$$

$$We = \frac{\upsilon^2 \rho L}{\gamma} \tag{2-3}$$

$$Oh = \frac{\sqrt{We}}{Re} = \frac{\eta}{\sqrt{\gamma \rho L}} \tag{2-4}$$

where Re is Reynolds, We is Weber, and Oh is Ohnesorge numbers, υ is droplet velocity, L is characteristic length, ρ is density, η is viscosity, and γ is surface tension. Reynolds number refers to the ratio of inertial forces to the viscous forces. Weber number on the other hand is the ratio of the inertial forces to the surface forces. Ohnesorge number provides the information on the relative importance of the viscous forces compared to inertial and surface forces.[90] For a stable drop formation, the range of $Z = 1/Oh$ should be $1 < Z < 10$ to avoid a large number of satellite droplet formation when $Z > 10$ or total dissipation of jetting energy required for droplet generation when $Z < 1$.[91, 98]

The deposited droplet deforms, spreads on the substrate, and eventually achieves an equilibrium after a brief oscillation that dissipates the energy.[87] Once the droplet reaches equilibrium after impact, it is possible to model it as a spherical cap, provided that gravitational forces are negligible.[92] Adjacent droplets tend to coalesce into a single body of liquid if the earlier droplet does not solidify before the later one is deposited. A series of droplets deposited with a sufficient inter-droplet distance forms a liquid bead. Considering fixed bead width due to contact line pinning and neglecting gravitational forces, the bead can be assumed to be uniform having a cross-section of a circular segment. Employing conservation of volume along with the previous assumptions, it is possible to develop a geometric model for the bead, which can be used to estimate maximum allowable interdroplet distance for given initial droplet diameter before the impact, the diameter of the spherical cap on the substrate, and contact angle in order to achieve a uniform cross-section.[93] When the interdroplet distance is kept above that limit, either individual droplets or scalloped lines are obtained. Decreasing the interdroplet distance below its allowable limit leads to uniform lines. When the interdroplet distance is reduced too much, below a certain limit, uniformity is lost, and bulges appear along the track.[87,88,94] Duineveld explained the formation of bulge instabilities with the contact angle of the liquid becoming larger than the advancing contact angle, which depends on substrate velocity and applied liquid volume.[95] If the earlier droplet solidifies before the adjacent droplet reaches the substrate, a line morphology that looks like stacked coins is observed. This situation occurs regardless the interdroplet distance and related to individual solidifying of the droplets.[96] When the deposited droplets solidify instead of solvent evaporation, due to lack of liquid-to-liquid interaction, droplets solidify separately as single beads. Accordingly, Tetik *et al.* investigated the effects of interdroplet distance and time lapse between successive droplets on the geometry of strands obtained after coalescence of droplets.[97]

Considering the requirements to achieve uniform lines using inkjet printing systems, Zhang *et al.*[30] fabricated ultra-light graphene aerogels using an IBP setup.[30] They Considering the requirements to achieve uniform lines using inkjet printing systems, Zhang *et al.*[30] fabricated ultra-light graphene aerogels using an IBP setup.[30] They used a low concentration aqueous GO-based solution as ink, and the material was deposited on top of a cooled substrate, which resulted in directional solidification. Depositing the ink layer by layer, frozen 3D structures with complex geometries were obtained. Water, which was completely sublimated with a subsequent freeze-drying process, was used as support material to achieve true 3D structures with overhang features. New layers deposited on top of an already frozen layer causes a partial melting, low viscosity ink fills the voids existing between layers, and both layers freeze together. This provides higher structural integrity to the 3D-printed aerogels. Using the same setup loaded with piezoelectric and solenoid valve inkjet heads, they reported ultralight aerogels from AgNWs[44], MoS_2–graphene composites,[45] MnO_2–graphene aerogels,[99] and cellulose nanocrystals.[100]

Stereolithography-Based 3D Printing

SLA, which was developed by 3D Systems in 1986, was the first commercialized 3D printing system.[101] Among other 3D printing methods, SLA is particularly versatile considering the freedom of designing structures with sub-micrometer level resolutions.[102] It is based on solidification of a liquid resin usually by a chemical crosslinking process, which was achieved through photocuring the liquid resin via scanning by a positionally programmed laser over the resin surface to initiate photopolymerization.[103] The resin consists of a monomer, a photoinitiator, and a photoabsorber. As the photoinitiator absorbs the light illuminated regions, it generates excited free radicals, which combine and react with the monomer to form larger reactive molecules. These reactive molecules keep reacting with adjacent monomers and grow until two of them combine

and terminate the reaction. The solidified polymer structure eventually forms by the entanglement and crosslinking of these polymer chains.[104] Precision of the resin curing is related to curing depth (C_d) and curing width (L_w).[103] The theoretical expressions can be derived from Beer–Lambert equations[105]:

$$C_d = D_p \ln\left(\frac{E_{max}}{E_c}\right) \tag{2-5}$$

$$L_w = W_0 \sqrt{2\frac{C_d}{D_p}} \tag{2-6}$$

where D_p is penetration depth of the resin at the laser wave- length, W_0 is the radius of the Gaussian beamE_{max}, is maximum laser exposure value, and E_c is critical laser exposure value. E_{max} is a function of the laser properties such as its power, beam radius, and scanning speed, while E_c completely depends on photoinitiator and liquid monomer used in the resin formulation.[103]

To fabricate silica aerogels by SLA, Saeed *et al.* formulated a photocurable resin composed of tetraorthosilicate (precursor for silica aerogel), hexanedioldiacrylate (monomer), Eosin Y (photoinitiator), and amine (co-initiator and pH modifier). After exposing the resin to a 2 W laser source using masks in a layer-by-layer manner, they obtained silica aerogels. They also showed the 3D printability of the resin they formulated by printing a 50 μm thick line on a glass substrate through the direct shining of the laser on the liquid mixture without any mask.[42] Morris *et al.* fabricated chitosan–poly- ethylene glycol diacrylate (PEGDA) composite scaffolds using Irgacure 819 as photoinitiator. They employed a commercially available SLA printer with a 405 nm laser to 3D print scaffold aerogels for tissue engineering purposes.[43] Hensleigh *et al.* formulated a resin based on GO dispersion mixed with photo- curable acrylates and a photo-initiator. Using a 405 nm laser light, they fabricated lightweight graphene aerogels.[32]

Drying and Post-processing

As 3D printing process is completed, structures are dried in a manner that the solid network inside the gel keeps its structural integrity with no or minimal shrinkage. Surface tension at the liquid–vapor interface, which is responsible for the col- lapse of the solid network during drying of gels, must be minimized for the solid network to keep its structural integrity and shape.[106] There are three main methods proposed to eliminate the surface tension while drying the gels: FD, SCFD, and AD. In SCFD, the solvent is kept above the supercritical temperature and pressure, where there is no distinction between the liquid and gas phase. FD briefly consists of freezing of the solvent followed by a sublimation process under vacuum. The porosity obtained after FD is a replica of the solvent crystals (which are sublimated with FD) that grow during the freezing step. Hence, it is very common to manipulate the freezing conditions in order to achieve a tailored micropore morphology as in freeze casting method.[74] To achieve a damage-free drying in ambient pressure, solid network strengthening, surface modification that reduces surface tension, or both can be used.[107–110] We provided a comparison of the common drying methods used for fabricating 3D-printed aerogels in Table 2.1.

Even though there are several reports using SCFD[39,42,52,70–72,111–113], a vast majority of the studies that reported 3D-printed aerogels employs FD to achieve a damage-free microstructure. This can be attributed to its capability of controlling micropore morphology by manipulating the freezing conditions as frequently used in freeze casting processes.[74,114,115] With isotropic freezing, which is achieved without a temperature gradient, an isotropic pore morphology that is similar to the one obtained after SCFD is obtained, yet, manipulating the freezing conditions can help tailoring the pore morphology. Hence, when a directional temperature gradient is used for freezing as in unidirectional freeze casting, microwalls and pores that are aligned along the applied

Table 2.1. Comparison of the common drying methods used for fabricating 3D-printed aerogels.

Drying Method	Drying Conditions	Duration [h]	Fabricated Aerogels	Notes
SCFD	30/40°C 7/12 MPa	3/5	Polymer, GO, RF, silica	Contains potential safety hazards due to high pressure. The conventional drying method for aerogel fabrication. Better preservation of fine solid network structure resulting in mesopores and small macropores.
FD	-76/-35°C 0.6/20 Pa	12/48	Polymer, ceramic, GO, MXene, metal,	Requires more time for complete drying of the gels. Provides a control on the micro- structure of the final aerogels. Larger pore dimensions due to the growth of solvent crystals.
AD	Room temperature, fume hood—ambient pressure	10/96	Polymer, graphene	Requires solvent exchange and/or solid network strengthening. Simplest process in exchange for a large amount of visible shrinkage.

temperature gradient are obtained. Accordingly, many studies combined unidirectional freeze casting process with 3D printing so that, the micropore structure of the resulting aerogels was aligned along the temperature gradient.[30,41,44,45,54,58,59,99] Apart from SCFD and FD, Françon *et al.* proposed an ambient temperature drying method for 3D-printed wet-stable CNF aerogel.[116] They thawed frozen gels inside ethanol and applied a solvent exchange procedure with acetone, which could presumably be easy and meet industrial requirements both in terms of energy consumption and production rate compared to SCFD and FD. Håkansson *et al.* compared the performance of different drying methods (air drying, air drying with surfactants, solvent exchange before drying, and FD) using 3D-printed CNF-based aerogels.[50] They showed that after air drying, the 3D-printed structure collapses due to gravity. Using surfactants with air drying reduced the surface tension and shrinkage obtain in a homogeneous manner. Applying a solvent exchange before air drying was quite similar to drying in air with surfactants. FD eliminated the shrinkage observed in other cases, and the printed structure kept its original geometry. Lin *et al.* proposed to use solvents

with high vapor pressure to formulate graphene-based inks.[38] Since the solvents (phenol and camphene) used in the ink formulations are solid at ambient temperature, a sublimation was possible in a fume hood at room temperature. The micropore morphologies of the 3D-printed graphene aerogels were highly dependent on the solvent and additives used in the ink formulations. Guo *et al.* added a foaming agent into the ink that is composed of tetraethyl orthosilicate (TEOS)-based aerogel powder, binder, and other additives.[117] The presence of the foaming agent in the ink formulation ensured the protected porosity of the silica aerogels after drying in the ambient conditions.

After drying the 3D-printed structures, some chemical or physical processes might be necessary to enhance the materials properties and/or provide functionalities to the final aerogels. Accordingly, 3D-printed aerogels made from polymer composites such as mesoporous bioactive glass (MBG)/sodium alginate–sodium alginate, collagen, cellulose, and polycaprolactone–gelatin were chemically crosslinked using a $CaCl_2$ solution,[118] 1-ethyl-(3-3-dimethylaminopropyl) hydrochloride solution,[35] polyamide-epichlorohydrin,[55,56] and glutaraldehyde solution,[62] respectively. When ceramics are used as building materials, sintering is used after drying to consolidate and densify the structure.[41] GO-based aerogels are commonly treated by chemical[51,53,64,70,119–121] or thermal[24,26,30,32,37,51,57,63,71,119,122–124] reduction methods to obtain conductive rGO. Other reported pyrolysis procedures are applied to convert resorcinol–formaldehyde into carbon,[39] and ammonium thiomolybdate into black MoS_2–rGO.[45] Ma *et al.* proposed to use 3D-printed rGO aerogels as a skeleton inside a reactor that contained a mixture of $KMnO_4$ and HCl, which subsequently yielded MnO_2/rGO aerogels after a thermal treatment.[99] Similarly, Yao *et al.* fabricated MnO_2/rGO aerogels by electrodepositing MnO_2 nanosheets on a rGO aerogel scaffold.[123]

Applications of 3D-Printed Aerogels

Electrochemical Energy Storage Systems

Electrochemical energy storage devices, such as supercapacitors and batteries, are widely applied in portable electronics and devices.[125] As an essential part of electrochemical energy storage devices, electrode is where electrochemical reactions happen. In supercapacitors, charges accumulate at the electrode-electrolyte interface as an electrical double layer or they are partially stored by faradaic reaction at the surface of electrodes. While in batteries, electrochemical reactions occur at the bulky electrodes. Therefore, electrodes play a critical role in determining the energy storage performances. Among various electrodes, conductive aerogels are promising candidates for both supercapacitors and batteries due to their porous structures and high surface areas. Such microstructure maximizes the electrochemical reaction area, endows high ion accessibilities, and shortens ion diffusion paths that enhance the rate performance for energy storage.[126,127] In the fabrication of aerogels-based electrodes, compared with traditional methods, such as chemically derived approach and freeze casting, 3D printing provides unique advantages: 1) electrodes can be fabricated in customization for versatile application; 2) the electrodes usually own a high aspect ratio (height to cross-section area) contributing to enhancing areal energy density; 3) possibly eliminated steps of device assembling and packaging can reduce the cost during device manufacturing; and 4) the operation is efficient, safe, low-cost, and environmentally friendly since no excess material is wasted and complex fabrication procedures are eliminated.[23,128] Therefore, in this section, the application of 3D-printed aerogel electrodes for supercapacitors and batteries is reviewed.

3D-Printed Aerogel Electrodes for Supercapacitor Applications

Supercapacitors safely providing fast charging, high power density, and excellent cycle stability capture lots of attention from academic researchers, industrial manufacturing, and practical applications. However, the modest energy density of supercapacitors limited their application. To address this dilemma, extensive efforts have been devoted to studying novel electrode materials and optimizing structures of electric double layer capacitor (EDLC) electrodes and pseudocapacitive electrodes.[129] Electrodes with interconnected structures were highly suggested since they can provide a continuous charge transport pathway and result in a good specific capacity.[130] 3D printing is an efficient method to fabricate customized aerogels owning interconnected structures. Meanwhile, in addition to the high specific area and controllable pore size, 3D-printed aerogels are highlighted with predefined and stable spatial orientations and optimal interspaces.[131] All these characters contribute to an enhanced energy density. Table 2.2 summarizes supercapacitors utilizing 3D-printed aerogel electrodes from the aspects of starting materials, printing method, postprocessing, and electrochemical performances. The table shows that rGO-based materials and extrusion- based 3D printing methods are the most widely used material and printing method to fabricate 3D-printed aerogel. Also, researchers prefer thermal reduction (TR) or chemical reduction (CR) to treat the printed materials after printing. In short, this section will detail the benefits of 3D-printed supercapacitor electrodes, review the available inks, as well as introduce the development of 3D-printed pseudocapacitive electrodes in recent years. 3D-printing is an excellent alternative approach to fabricate aerogel electrodes and even all 3D-printed supercapacitors. First, 3D-printed aerogels provide an ultrahigh porosity and an open structure benefiting the introduction of function groups and enhanced pseudocapacitive

Table 2.2. Summary of the 3D-printed aerogel supercapacitor electrodes and devices.

Refs.	Materials	Deposition	Postprocessing	Max specific capacitance	Cyclic stability
40	$Ti_3C_2T_x$//$Ti_3C_2T_x$	EBP (pneumatic)	-	2100 mF cm^{-2} at 1.7 mA cm^{-2}	90.36% at 1 A g^{-1} for 10000 cycles
53	GO–Ca^{2+}//GO–Ca^{2+}	EBP (pneumatic)	CR of GO	213 F g^{-1} at 0.5 A g^{-1}	90% at 10 A g^{-1} for 50000 cycles
58	$Ti_3C_2T_x$–AgNW–MnONW–C60//$Ti_3C_2T_x$–AgNW–MnONW–C60	EBP (pneumatic)	-	216.2 mF cm^{-2} at 10 mV s^{-1}	85% at 200 mV s^{-1} for 10000 cycles
64	rGO–MWCNT	EBP (mechanical)	CR of GO	639.56 mF cm^{-2} at 4 mA cm^{-2}	90% at 40 mA cm^{-2} for 10000 cycles
24	SFrGO	EBP (mechanical)	CR of GO, surface functionalization	252.4 F g^{-1} at 5 mA cm^{-2}	-
	rGO–MnO_2//SFrGO	EBP (mechanical)	CR of GO, surface functionalization, electrodeposition of MnO_2	853.3 mF cm^{-2} at 5 mA cm^{-2}	93% at 100 mV s^{-1} for 100000 cycles
65	CMrGO	EBP (mechanical)	TR of GO	16 F g^{-1} at 2 mV s^{-1}	-
	CMrGO//CMrGO	EBP (mechanical)	TR of GO	140 F g^{-1} at 3 A g^{-1}	80% at 15 A g^{-1} for 10000 cycles
68	rGO–ZnV_2O_6//rGO–VN	EBP (screw)	TR of GO	149.71 F g^{-1} at 0.5 A g^{-1}	95.5% at 1 A g^{-1} for 10000 cycles
70	rGO–GNP	EBP (pneumatic)	TR of GO, chemical etching of silica fillers	~72 F g^{-1} at 0.5 A g^{-1}	-
	rGO–GNP//rGO–GNP	EBP (pneumatic)	TR of GO, chemical etching of silica fillers	4.76 F g^{-1} at 0.4 A g^{-1}	95.5% at 200 mV s^{-1} for 10000 cycles
99	rGO–MnO_2	IBP	TR of GO, MnO_2 coating	213 F g^{-1} at 2 A g^{-1}	-
	rGO–MnO_2//rGO–MnO_2	IBP	TR of GO, MnO_2 coating	95 F g^{-1} at 1 A g^{-1}	78% at 5 A g^{-1} for 1000 cycles
116	CNF–alginate–PEDOT	EBP (pneumatic)	PEDOT functionalization	78 F g^{-1} at 0.1 A g^{-1}	-
121	rGO–AgNW–MONW//rGO–AgNW–MONW	EBP (pneumatic)	CR of GO	426 mF cm^{-2} at 2.27 mA cm^{-2}	97.4% at 200 mV s^{-1} for 1000 cycles
123	rGO–MnO_2	EBP (pneumatic)	TR of GO, electrodeposition of MnO_2	1874 mF cm^{-2} at 0.1 mA cm^{-2}	-

	rGO–MnO_2//rGO–MnO_2	EBP (pneumatic)	TR of GO, electrodeposition of MnO_2	1874 mF cm^{-2} at 0.1 mA cm^{-2}	92.9 at 20 mV s^{-1} for 20000 cycles
124	rGO–PPy	EBP (pneumatic)	TR of GO, chemical deposition of PPy	540 F g^{-1} at 0.1 A g^{-1}	-
	rGO–PPy//rGO–PPy	EBP (pneumatic)	TR of GO, chemical deposition of PPy	1100 mF cm^{-2} at 0.5 mA cm^{-2}	75% at 200 mV s^{-1} for 5000 cycles
139	rGO–NiCoS	EBP (pneumatic)	CR of GO	217.6 mAh g^{-1} at 1 A g^{-1}	-
	rGO–NiCoS// rGO–MWCNT	EBP (pneumatic)	CR of GO	746 mF cm^{-2} at 10 mA cm^{-2}	87.6% at 100 mA cm^{-2} for 10000 cycles
134	rGO//rGO	EBP (pneumatic)	CR of GO	56.7 mF cm^{-2} at 5 mV s^{-1}	~100% after 10000 cycles
136	rGO–VO_2//rGO–VO_2	EBP (pneumatic)	CR of GO	133.2 mF cm^{-2} at 0.43 mA cm^{-2}	-
	rGO–VNQDs//rGO–VNQDs	EBP (pneumatic)	CR of GO	98.8 mF cm^{-2} at 0.65 mA cm^{-2}	-
	rGO–VO2//rGO–VNQDs	EBP (pneumatic)	CR of GO	207.9 mF cm^{-2} at 0.63 mA cm^{-2}	65% at 6 mA cm^{-2} for 8000 cycles
140	GO–PAA	EBP (pneumatic)	TR of GO and carbonization of PAA	870.3 mF cm^{-2} at 4.6 mA cm^{-2}	81% at 1.2 mA cm^{-2} for 20000 cycles

performances. The enlarged specific surface area maximizes the functionalization effect. The open structure contributes to enhanced ion accessibility to the surface functional groups even at high current densities.[24] Second, 3D printing can fabricate supercapacitors with complex architecture for portable and wearable electronics.[58,124,132–134] 3D printing enables the aerogel being precisely patterned within a range of 100 μm^2 to 1 m^2 with a minimum feature size of 1 μm.[135] Third, 3D printing could save cost in supercapacitor fabrication through removing device parts assembly steps. An all 3D-printed asymmetric microsupercapacitor is fabricated from a graphene–vanadium nitride quantum dots (VNQDs) with rGO (G–VNQDs/rGO) anode, a V_2O_5/rGO construct cathode, and a gel-like electrolyte.[136] No extra assembly process is needed. The current collector can also be

printed to eliminate the assembly steps. Rocha *et al.*[65] printed the current collector (copper) and chemically modified reduced graphene oxide (CMrGO), and then they sintered the 3D-printed Cu and the 3D-printed CMrGO simultaneously for supercapacitors.

Fabricating printable inks is the most critical issue for 3D printing. As discussed in Section 2.2, suitable rheological behaviors are critical for 3D printable inks. Adding additives in ink is a common method to fulfill the rheological requirement for 3D printing in EDLC. However, when applied in supercapacitors, the additives such as polymers or inorganic nanoparticles may cause negative effects including decreased strength and electrical conductivity. A complex postprocess is needed to remove these additives.[53] Therefore, printable ink formulations consisting of highly electronically conductive materials, such as multiwalled carbon nanotubes[64] and vanadium nitride (VN),[68,136] prefer to optimize the rheological behaviors of inks. Except for these expensive materials, Jiang *et al.*[53] introduced trace Ca^{2+} as a gelator into rGO to fabricate (rGO–Ca^{2+}) ink to modify the rheological properties of the printable ink. Com- pared with rGO–GNP (63.6 F g^{-1}) adding inorganic nanoparticles as gelators,[70] and CMrGO (≈60 F g^{-1}) using a polymer as the binder,[65] Jang's design dramatically enhanced the specific capacitance of rGO–Ca^{2+} to achieve 200 F g^{-1} at 10 A g^{-1}.

In addition to direct printing of mixture inks in 3D-printed pseudocapacitive electrodes, aerogel can be printed as a scaffold for loading active materials by EBP to boost the electrochemical performance.[24,99,116,123,124] Currently, cathode thickening with large mass loading is employed to improve the energy density and capacitance of pseudocapacitive electrodes. However, sluggish electron transport and ion diffusion result in drastic capacitance loss with increasing electrode thickness in pseudocapacitive electrodes.[137] Fortunately, these drawbacks can be tackled via utilizing

high-surface-area 3D-printed aerogels as a scaffold in electrodes, by which higher loading of active materials and thick electrodes can be achieved.[70,138] For example, Yao *et al.*[123] loaded 182.2 mg cm^{-2} MnO_2 by electrodeposition onto a 3D-printed porous carbon aerogel scaffold (rGO–MnO_2), achieving about 25 times higher areal capacitance than that of bare annealed graphene aerogel electrode. A similar excellent performance was achieved by loading MnO_2 onto 3D-printed rGO using hydrothermal growth.[99] Some scaffolds used to fabricate pseudocapacitive electrodes, including MnO_2-based 3D-printed rGO (rGO–Mn_2O),[99,123] a novel surface-functionalized 3D-printed rGO (SFrGO),[24] poly(3,4- ethylenedioxythiophene):tosylate (PEDOT:TOS)-functionalized CNFs and alginate aerogel,[116] and polypyrrole-coated rGO (rGO–PPy).[124] All these electrodes are proved with remarkable electrochemical behaviors, as summarized in Table 2.2.

3D-Printed Aerogel Batteries

3D-printed aerogel electrodes are also employed in batteries to boost the energy density. Generally, increasing the thickness of electrodes with a high-volume ratio of active materials is an interesting approach for enhancing the areal energy density of batteries.[141] However, the traditional slurry-coated thick electrode brings increased charge transfer distance, deteriorated reaction kinetics, and risks of electrode fracture and delamination, leading to unsatisfactory performances. The 3D structural aerogel electrodes are promising to alleviate these negative effects since the porous structure results in short ion diffusion pathways enhancing the ion transport. There are four generally accepted approaches to get the 3D porous structure: self- assembled framework, template-assisted foams, electrospun fibers, and 3D printing.[142] Comparing with other methods, 3D printing is able to precisely predict and control the final structure of the porous electrodes. Meantime, 3D-printed conductive aerogels have the characteristics of ordered macropore structure with stable spatial orientations, and optimal interspaces nano- structure, these structure properties

further enhance capacity retention and cyclability.[26] Besides, 3D printing is being utilized to design, optimize, and fabricate microbattery owning engineered porous architectures. For instance, Fu *et al.*[57] printed GO-based interdigitated cell occupies 3 mm × 7 mm in size for Li-ion batteries. In addition, they fabricated an all-3D-printed Li-ion battery, demonstrating the possibility of eliminating the battery assembly step. According to these advantages, 3D printing has been extensively researched in the battery field, such as Li-ion battery,[57] Li–S battery,[122] Li–O_2 battery,[26] Li metal battery,[143] and Na-ion battery.[45,144]

3D-printed aerogel electrodes have been widely reported in application of Li ion batteries in past decade. In 2016, Fu *et al.*[57] first proposed rGO-based electrode inks for a 3D-printed Li-ion battery. They mixed rGO with active materials, $LiFePO_4$ (LFP) and $Li_4Ti_5O_{12}$ (LTO) nanoparticles, as the cathode (rGO–LFP) and anode (rGO–LTO), respectively. The electrical conductivity of 3D-printed battery electrodes were significantly improved from 10^{-4} (LFP) and 10^{-6} (LTO) S cm^{-1} to 31.6 S cm^{-1} (rGO– LFP) and 3.1 S cm^{-1} (LTO/rGO). Furthermore, an all 3D-printed Li-ion battery was designed and assembled with rGO–LFP as the cathode, rGO–LTO as the anode, and a polymer composite ink containing poly(vinylidenefluoride)-*co*-hexafluoro-propylene (PVDF-*co*-HFP) and Al_2O_3 nanoparticles as an electrically insulated separator as well as the gel polymer electrolyte.[57] That means 3D printing can minimum the complex assembly steps. Later, Zhang *et al.*[48] replaced rGO–LTO with the composite of SnO_2 quantum dots and rGO (rGO–SnO_2) to improve the electrochemical performance for lithium storage by increasing active sites, shortening ion diffusion length, and minimizing the volume change. Inspired by these works, sulfur copolymer–graphene architecture was proposed to suppress a shuttle effect, in which a cathode ink, containing a mixture of sulfur particles, 1,3-disso- propenylbenzene (DIB) and

condensed GO (rGO–S–DIB), was utilized for Li–S batteries.[122] In addition, a 2D nanomaterials with a complex hierarchical porous structure, holey graphene oxide (hGO) electrode, was produced. The multiple levels of porosity (from macroscale to nanoscale) of 3D-printed rGO allow pathways for electrolyte and oxygen gas transfer for Li–O_2 cells and enhance their electrochemical performance.[26]

3D-printed aerogel electrodes also enables high performance Li metal batteries. Compared with conventional Li-ion batteries, Li metal batteries possess higher energy density due to Li metal anode owning ultrahigh specific capacity (3860 mAh g^{-1}) and lowest reduction potential (–3.04 V vs standard hydrogen electrode). However, it is hard to directly produce 3D Li metal through 3D printing owning to the high chemical reactivity of Li metal and liquid-like melting Li metal. Cao *et al.*[143] first eliminated this predicament using a Li-infused porous c-CNF scaffold as an anode (c-CNF–Li) and c-CNF–LFP as a cathode to fabricate a 3D-printed Li metal battery. Moreover, 3D printing provides the possibilities for miniaturization and autonomous shaping of Li metal anode based on excellent rheological properties of as-prepared CNF/LFP ink. The plateau of the loss modulus (G'') is one order of magnitude lower than that of the storage modulus (G'), which indicates the predominant elastic behavior of the solid-like nature of these inks. More importantly, in contrast to the traditional planar Li metal electrode, the highly porous c-CNF–Li anode structure ensured uniform electrolyte distribution and Li metal plating on the electrode surface. Compared with Li foil anode, whose voltage profile was stable for 80 h, the c-CNF–Li cell exhibited excellent stability with a low voltage hysteresis for 300 h. Furthermore, outstanding cycling stability is achieved in the c-CNF–LPF/c-CNF–Li full cell, the charge/ discharge. A high capacity (80 mAh g^{-1}) was delivered at a charge/discharge rate of 10C with 85% capacity retention after 3000 cycles, which can be attributed to 1) c-CNF enhancing the electrical conductivity and

Table 2.3. Summary of the 3D-printed aerogel electrodes of batteries.

Refs.	Materials	Deposition	Postprocessing	Initial Capacity	Cyclic stability
57	rGO–LFP	EBP (pneumatic)	TR of GO	168/164 mAh g^{-1} at 10 mA g^{-1}	~170 mAh g^{-1} in the 20 cycles
	rGO–LTO			184/185 mAh g^{-1} at 10 mA g^{-1}	169–198 mAh g^{-1} in the 20 cycles
	rGO–LFP// rGO–LTO			117/91 mAh g□1 at 50 mA g□1	110–108 mAh g^{-1} in the 10 cycles
143	CNF–LFP	EBP (pneumatic)	Thermal carbonization of CNF	167/140 mAh g^{-1} at 34 mA g^{-1}	–
	c-CNF–Li			2346 mAh g^{-1} at 100 mA g^{-1}	–
	c-CNF–LFP//c-CNF–Li			137 mAh g^{-1} at 0.2C	85% of initial capacity after3000 cycles
122	rGO–S–DIB	EBP (pneumatic)	TR of GO	812.8 mAh g^{-1} at 50 mA g^{-1}	43.4% after 50 cycles
145	$Ti_3C_2T_x$	EBP (pneumatic)	Li plating	127.6 mAh g^{-1} at 10C with LFP cathode	99.4% at 1C after 300 cycles
26	rGO mesh	EBP (pneumatic)	TR of GO	13.3 mAh cm^{-2} (3879 mAh g^{-1}) at 0.1 mA cm^{-2}	–
144	rGO–NVP	EBP (pneumatic)	TR of GO	1.26 mAh cm^{-2} at 0.2C	90.1% at 1C after 900 cycles
45	rGO–MoS_2	IBP	TR of GO and pyrolysis	800 mAh g^{-1} at 100 mA g□1	429 mAh g^{-1} in the 10 cycles
48	rGO–SnO_2	EBP (pneumatic)	TR of GO	991.6 mAh g^{-1} at 50 mA g^{-1}	1004.9 mAh g^{-1} after 50 cycles
146	rGO–CNT	EBP (pneumatic)	TR of GO	101.1 mAh g^{-1} at 100 mA g^{-1}	67.6 mAh g^{-1} at 100 mA g^{-1} after 100 cycles

improving the performance at high rates; 2) the 3D porous structure having good contact with the electrolyte and accelerating the charge transfer; 3) Li dendrite inhibition stabilizing Li plating and striping. Furthermore, MXene arrays and lattices were printed as an alternative to c-CNF for metal-based electrodes.[145] These printed electrodes are capable of guiding the deposition of Li and preventing Li dendrites growth via unifying distributions of Li-ion flux and electric field.

Apart from lithium batteries, two excellent outcomes were achieved in 3D-printed aerogel sodium-ion batteries.[45,144] In traditional highly condensed GO or GO-contained compact frameworks, the

compact construction inhibited electrolyte infiltration and big size sodium ions (1.02 Å) diffusion. Ding *et al.*[144] first utilized 3D-printed hierarchical porous GO-contained frameworks to overcome these issues. The as-prepared frameworks with continuous filaments and hierarchical multi-hole gridding structures could facilitate sodium ion transport. Later, Brown *et al.*[45] proposed a MoS_2@rGO anode in Na-ion battery by 3D freeze-printing technique.[30] The aqueous ink droplets were rapidly frozen at –30°C on a cold substrate plate. Through this method, MoS_2 nanoparticles were anchored on the surface of rGO nanosheets and can be applied as anode for Na-ion batteries.

Electrical Energy Generator

Besides energy storage applications, 3D-printed aerogels were also proposed to fabricate devices that generate electrical energy. Triboelectric nanogenerators (TENGs) can convert mechanical motions into electricity based on the coupling effects of triboelectrification and electrostatic induction. These devices have experienced dramatic development since their invention in 2012.[147] It has been shown that the increased surface area by introducing micro- and nanoscale topographies on the material surface provides an enhanced power output.[148] Aerogels having ultralow density and high specific surface area have been promising materials and attracted the interest of researchers working on TENGs.[149] Furthermore, additively manufactured aerogels, due to their hierarchical micro/nano- structures, provides better performance than their traditionally molded counterparts.[150] For instance, Peng *et al.* 3D-printed graphene aerogels and showed their potential as a compressible, high performance TENG electrode.[151] In another study, Qian *et al.* utilized 3D-printed CNF aerogels to fabricate TENGs with 3D micro/nanohierarchically patterned structure.[150] They benefit from the hierarchical micro/nano-3D structure obtained after 3D

printing and subsequent drying to enhance the effectivity in utilizing the structure and contribute to the contact area, surface roughness, and mechanical resilience of the device, which consequently contributes to improving the triboelectric response with a higher voltage output than the traditional molding TENG counterpart. Ma *et al.* further explored the integration of a contact mode TENG and an rGO–MnO_2-based supercapacitor into a self-powered system that is capable of converting mechanical signals into electrical power and further storing such scavenged power.[99] The discharge specific capacitances of the rGO–MnO_2 are 95 F g^{-1} at 1 A g^{-1} and 45 F g^{-1} at 10 A g^{-1}. The measured open-circuit voltage, short-circuit current, and transfer charge of TENG indicate that it is necessary to rectify the direct electrical outputs from the TENG. When the external load matches the internal impendence of TENG about 200 MΩ here, the highest instantaneous powder output will achieve about 2.5 μW. Mechanical inputs from finger pressing can be successfully harvested by the TENG and conversed mechanical energy to electrical energy. The holistic integration of energy harvesting and storage units promises the implementation of self-powered wearable devices with greater intelligence that can scavenge and store environmental energy through sustainable pathways for ubiquitous electronics in societally pervasive applications.

Biomedical Applications

TE, which is the most common biomedical application of 3D-printed aerogel scaffolds, aims to develop appropriate replacements for damaged tissues and organs.[33] The dam- aged tissues are regenerated by attaching and culturing cells on appropriate scaffolds and grafting back into the patient.[152] Scaffold and its architecture has an important role in tissue regeneration since it preserves the tissue volume, provides temporary mechanical function, and delivers biofactors required for cell life.[153] The scaffold should possess interconnecting pores to favor tissue integration and

vascularization. They also should be biodegradable and biocompatible, provided with an appropriate surface chemistry for cell attachment, differentiation, and proliferation. Mechanical strength along with ease of fabrication in custom shapes are also required.[154] Implementation of 3D printing into tissue engineering applications provides fabricating patient-specific scaffolds with high reproducibility and compositional variation.[155] Combination of 3D printing with aerogel fabrication techniques such as FD or SCFD provided fabrication of hierarchical scaffolds with improved cellular behavior.[25]

Using porous scaffolds for tissue engineering purposes is a highly developed field, and there are many published reviews discussing the different aspects of the application.[154,156–163] Here, we aimed to present the scaffolds fabricated by 3D printing followed by a drying (FD, SCFD, or AD). A summary of these studies is provided in Table 2.4. The majority of TE reports focused on bone tissue regeneration using scaffolds based on MBG/SA,[118] poly(l-lactic acid) (PLLA)/tricalcium phos- phate (TCP),[33] PCL/gelatin,[62] chitosan,[25] chitosan/HAP,[164] and HAP.[41] The most important structural properties of the scaffolds fabricated for TE are their porosity and mechanical characteristics. Most of the 3D-printed aerogel scaffolds require an extra crosslinking or sintering process to enhance the mechanical strength while keeping the porosity in 72–95% range. The biocompatibility of the scaffolds is tested in vitro by seeding human bone marrow-derived mesenchymal stem cells (MSCs),[41,118] mouse preosteoblastic cells (MC3T3-E1),[62] and osteoblast.[25,164] Furthermore, Xiong *et al.*, evaluated the biocompatibility of the scaffolds loaded with bovine bone morphogenic protein by implanting them to repair segmental defects in canine radiuses.[33] Besides bone tissue engineering, Hsieh *et al.* fabricated waterborne biodegradable polyurethane (PU) composite scaffold aerogels for trachea tissue engineering

Table 2.4. Summary of 3D-printed aerogel scaffolds fabricated for tissue engineering applications.

Refs.	Materials	Deposition	Gelation/ solidification	Post processing	Porosity [%]	Strength [MPa]	Modulus [MPa]	Test type	In vitro	In vivo
118	SA-based	EBP (pneumatic)	–	Crosslinking	72–84	2.3–7.5	–	Comp*	MSC	–
62	PCL/gelatin	EBP (mechanical)	–	Crosslinking	79.32	–	30.5	Comp	MC3T3-E1	–
25	Chitosan	EBP (pneumatic)	Directional freezing	Crosslinking	85	0.09	0.92	Tens**	Osteoblast	–
					90	0.07	0.8	Tens		
164	Chitosan/ HAP	EBP (pneumatic)	NaOH–ethanol medium	–	–	–	–	–	Osteoblast	–
41	HAP	EBP (pneumatic)	Directional freezing	Sintering	–	22	–	Comp	MSC	–
33	PLLA/TCP	EBP (screw)	Cryogenic chamber	–	89.6	12.1	–	Bend***	–	Repair segmental defects in canine radiuses
						4.71	60.11	Comp		
76	PU	EBP (pneumatic)	Directional freezing	–	–	–	0.0102	Bend	MSC	Scaffolds implanted in nude mice
						4.6	0.0211	Tens		
						–	0.11–0.78	Comp		
35	Collagen	EBP (pneumatic)	Directional freezing	Crosslinking	95.3	2.8	28.1	Tens	KFCM	–
165	PCL	EBP (mechanical)	Directional freezing	Infused with PCL	–	–	0.05	Comp	MSC	–
43	Chitosan/ PEGDA	SLA	–	–	–	–	1.125	Comp	MSC	–

purposes.[76] Scaffolds' biocompatibility was tested in vitro with seeded human umbilical cord-derived MSCs. Furthermore, in vivo studies were performed by implanting seeded scaffolds in nude mice. It was seen that six weeks after the implantation, scaffolds showed a compression modulus similar to that of the native trachea. Kim *et al.* tested the biocompatibility of collagen scaffolds for skin tissue engineering in vitro using keratinocyte/fibroblast coculture method (KFCM).[35] Munir *et al.* combined EBP and electrospinning to develop multizone scaffolds that mimic the complex architecture of the native cartilage.[165] They evaluated the biocompatibility of PCL scaffolds in vitro with MSC culture. Morris *et al.* used SLA to fabricate scaffolds form chitosan/ PEGDA composite.[43] Scaffolds were tested in vitro using MSC culture. In summary, 3D-printed aerogel scaffolds made from biocompatible ceramics and polymers are commonly used for TE applications. Since the mechanical properties of these scaffolds are crucial for their function, a thermal densification or a chemical crosslinking procedure is applied to enhance the strength of the scaffolds. Commonly, the biocompatibility of the 3D-printed scaffolds is tested through cell culture experiments, and there are several studies reporting the performance of the scaffolds after implanting into animal subjects.

Besides TE, 3D-printed aerogel scaffolds were also proposed for controlled drug delivery and wound dressing applications. Controlled drug delivery systems manage how the drugs are available to the target cells and tissues over time and in space in order to increase the efficacy and reduce the toxicity of the drugs.[166] Biocompatible aerogels are promising materials for drug delivery systems due to their large surface area and open porous structure.[167] Incorporating the additive manufacturing technologies (especially multimaterial printing) in the fabrication process of the biocompatible aerogels, enabled drug delivery systems with controllable release behaviors for multiple drugs.[118] To achieve 3D-printed aerogel-based drug delivery systems for the

treatment of asthma and chronic obstructive pulmonary disease, López-Iglesias *et al.* fabricated alginate aerogel microspheres loaded with salbutamol sulfate (SS) by using a thermal inkjet head.[111] SS was dissolved in the gelation bath and loaded in the microspheres during the gelation process. The SS loading in the microspheres was measured as 3% and a modified release profile, where 10% of the loaded drug was suddenly released during the first 15–30 min, followed by a slow release of the remaining SS load. Controlled drug delivery is also required in TE applications since local delivery and prolonged exposition of the bioactive molecules are necessary to minimize the release of the agent to nontarget sites and support tissue regeneration, which normally occurs in long time frames.[168] Furthermore, in order to avoid infection and inflammation, scaffolds with controllable multidrug release properties are desired. Accordingly, Fu *et al.* proposed to load the composite scaffolds fabricated for bone tissue engineering purposes with bovine serum albumin (BSA) and ibuprofen (IBU).[118] BSA and IBU were separately loaded in SA and MBG–SA layers and released with different rates, where 82% of BSA was released within 24 h while only 70% of IBU was released within 168 h. For the treatment of chronic wounds that do not heal normally, wound dressing devices are used for healing. These devices are expected to provide a moist environment which offers a protection from infections, and thermal insulation free from particulate or toxic contaminants allows adequate gaseous exchange. Furthermore, an elastic and non-antigenic structure with a nontraumatic removal capability is desired.[169] For wound dressing applications, Chinga-Carrasco *et al.* fabricated 3D-printed aerogels based on CNF, which were ultrapure with low level of endotoxins and thus complied with the above-mentioned criteria as well as FDA requirements for biomedical devices.[60] Similarly, Rees *et al.* proposed 3D-printed CNC-based aerogels for wound healing applications due to their structure that does not support bacterial growth.[36]

Sensors and Actuators

Piezoresistivity refers to a phenomenon when the electrical resistance of material changes in response to mechanical stress.[170] Piezoresistive sensors converting stress/strain data into a resistance signal are widely used in applications such as sport motion monitoring, electronic skin, rehabilitation, health-care monitoring, etc.[171] Aerogels based on conductive materials are promising active materials for piezoresistive sensors due to their highly porous nature with a great impact on the structure and resilience when under pressure.[172] 3D printing of aerogels can provide a freedom in the device design and help customization/personalization of the piezoresistive sensors.[100] Accordingly, 3D-printed aerogels based on AgNWs[44] and GO[30] were fabricated using IBP method and proposed to be used as strain sensors. The electrical resistance of the 3D-printed aerogels was highly constant over multiple cycles of compression, which indicates a significant structure resilience. Furthermore, the change in the resistivity with respect to the compressive strain showed a linear behavior and a recoverable resistivity response without hysteresis. Using a similar piezoresistivity behavior, Françon *et al.* used EBP to fabricate CNF aerogels functionalized with conducting PEDOT:TOS polymer as pressure sensors.[116] After compression, the resistance of the composite aerogels decreased to 10 from 20 Ω, and drastically increased to 60 Ω after unloading. The increase in the resistance from 20 to 60 Ω was attributed to the mechanical damage inflicted to the PEDOT structure during the first cycle. However, repeated tests showed that the resistance reversibly cycles between 10 and 60 Ω at compressed and released states, respectively. The same aerogels were also proposed to detect moisture by using hygroscopicity of cellulose. The electrical resistance of the composite aerogel decreased from 20 to 15 Ω when the relative humidity (RH) was increased from 20% to 90%. The increase in the RH caused swelling of the aerogel, which led

to an increase in the contact area between PEDOT covered surfaces. As the RH was decreased to 20% again, the aerogel shrank, and resistivity increased again. The hysteresis was attributed to the short duration of each RH step used in the experiment despite more time was required for cellulose to reach an equilibrium. Sensing capabilities of the 3D-printed aerogels are also tested in actual real-world applications. For instance, Guo *et al.* pro- posed to use 3D-printed GO–CNT composite aerogels as a new generation strain sensor due to the resistance-change-pattern of the aerogels being nearly identical in cyclic deformation states.[119] The ternary response of the aerogel sensors was used to monitor the movement and orientation of a snake-like robot. In another study, An *et al.* used EBP to fabricate wearable sensors from 3D-printed GO-based aerogels.[120] The change in the resistance of the aerogel devices with changing gestures of the fingers was investigated by principal component analysis (PCA) and hierarchical cluster analysis (HCA). Using these analyses, gestures of fingers can clearly be classified, and 3D-printed flexible graphene aerogels can be used as sensors to monitor the movement of joints, which can be beneficial, especially for the treatment of muscle atrophy or Parkinson's disease.

Instead of using piezoresistivity as a detecting tool, Li and co-workers proposed to exploit the solvent swelling properties of poly(glycerol sebacate) (PGS) thermosets to detect vapors of polar organic solvents, such as hexafluoroisopropanol (HFIP), tetrahydrofuran (THF), and acetone.[28] 3D-printed aerogels experienced a reversibly recoverable deformation after being exposed to vapors of the aforementioned solvent vapors. When3D-printed aerogel sensors were exposed to HFIP vapor from one side, due to gradual swelling from the surface to the back layer, exclusive curling to the back side was observed. The response of the aerogel to HFIP vapor was stable upon alternating exposure cycles and showed different bending angles to different solvent vapors. They also proposed to use the response of the aerogels as a soft actuator by employing a gradient structure,

which will provide an asymmetric swelling. Since the dense layer absorbed more solvent than the loose layer, swelling observed in the dense layer was also superior. The difference in the swelling response yielded an exclusive closing toward the loose surface, which was recovered after evaporation of the solvent.

Environmental Applications

Aerogels have widely been developed and proposed for environmental remedial applications such as CO_2 absorption from atmospheric air or absorptive removal of contaminants from water resources.[173] For instance, filters made from highly porous aerogels possessing 3D network structure, large open pores, and extremely low densities with special wettability are considered to be one of the most efficient methods for oil/ water separation.[174] Accordingly, Mohammed *et al.* benefited from EBP 3D printing to create covalent organic framework–GO aerogels with a hierarchically connected porosity for obtaining a rapid and efficient removal of pollutants from water.[27] In another study, He *et al.* proposed 3D-printed Au nanobipyramid–g-C_3N_4 nanosheets (CNNS)–SA hybrid aero- gels for solar wastewater remediation.[72] Aerogels were tested for their methylene blue, rhodamine B, and methyl orangephotodegradation capabilities under visible-light irradiation ($\lambda > 420$ nm) and showed a superior solar wastewater remediation activity with excellent cyclic stability and easy manipulation features. Moreover, the activity of the 3D-printed sample was about 2.5 times that of the contrast sample, attributing to the enhanced liquid velocity and solution diffusion efficiency because of the 3D-printed structure. Instead of an absorption- based water remediation strategy, Li *et al.* fabricated devices which are capable of generating solar steam for distillation of water.[175] Aerogel steam generation device (3D-CG/GN) was fabricated through an EBP strategy using CNT–GO and GO–CNF composites due to their efficient broadband solar absorption with excellent photothermal conversion and ability to transport

water from the bottom by capillary effects, respectively. Due to the high energy conversion efficiency under the illumination of the sun, the surface temperature of the 3D-CG/GN increases rapidly to 36.5°C while the surface temperature of water increases only 2°C. After an initial transient slow increase stage, the cumulative weight loss of the water under the 3D-CG/GN showed a steady evaporation rate. The efficiency of the 3D-CG/GN was calculated as 85.6%, which is one of the highest compared with other reported evaporators. Yang *et al.* 3D-printed carbon aerogels based on R-F ink and showed how the macroscopic pores affect the solar steam generation performance.[66] The 3D-printed carbon aerogels had a water evaporation rate of 1.57 kg m^{-2} under 1 sun illumination, and evaporation efficiency of 88.38%. The significantly high evaporation rate and efficiency is attributed to the better contact between the aerogel and light achieved after macroscopic porosity introduced by 3D printing technology.

An improved energy efficiency, which will help to reduce the total energy consumption, can be achieved by using high- performance insulation systems in buildings.[176] Aerogels, which reportedly have the lowest thermal conductivity values, has undergone a great progress as a thermal superinsulation material.[177] Due to their low thermal conductivity, noise abatement capability, and optical transparency, aerogels are highly used for thermal insulation applications in buildings, window panes, and solar collector covers.[176] Even though silica aerogels fabricated by conventional methods has been found to possess the lowest thermal conductivity value of any reported insulator, due to their brittleness and poor mechanical properties, machining by conventional subtractive manufacturing has been a great challenge.[178] A couple of very recent studies have addressed this issue and synthesized inks based on silica aerogel particles. Fabricating silica aerogels by additive manufacturing provided the ability of object development in different size and shape along with a macroporosity; which enables their use as insulating layers in electronics

and further reduces their thermal conductivities respectively.[112,117] Zhao *et al.* fabricated miniaturized silica aerogels achieved via an EBP method with an ultralow thermal conductivity of 15.9 mW m^{-1} K^{-1}.[112] In another study, Guo *et al.* successfully 3D-printed silica aerogels dried under ambient conditions, which eliminated the need for FD or SCFD.[117] The thermal conductivity of the reported aero-gels were as low as 53 mW m^{-1} K^{-1}, provided with a 56% reduction in the processing time compared to the aerogels dried using FD.

References

[1] Kistler, S.S., Coherent expanded aerogels and jellies. Nature, 1931. 127(3211): p. 741-741.

[2] Pierre, A.C., History of aerogels, in Aerogels Handbook. 2011, Springer. p. 3-18.

[3] Long, L.-Y., Y.-X. Weng, and Y.-Z. Wang, Cellulose aerogels: Synthesis, applications, and prospects. Polymers, 2018. 10(6): p. 623.

[4] Qian, F., P.C. Lan, M.C. Freyman, W. Chen, T. Kou, T.Y. Olson, C. Zhu, M.A. Worsley, E.B. Duoss, and C.M. Spadaccini, Ultralight conductive silver nanowire aerogels. Nano letters, 2017. 17(12): p. 7171-7176.

[5] Tang, Y., K.L. Yeo, Y. Chen, L.W. Yap, W. Xiong, and W. Cheng, Ultralow-density copper nanowire aerogel monoliths with tunable mechanical and electrical properties. Journal of Materials Chemistry A, 2013. 1(23): p. 6723-6726.

[6] Si, Y., X. Wang, L. Dou, J. Yu, and B. Ding, Ultralight and fire-resistant ceramic nanofibrous aerogels with temperature-invariant superelasticity. Science advances, 2018. 4(4): p. eaas8925.

[7] Pradeep, V., D. Ayana, M. Graczyk-Zajac, G. Soraru, and R. Riedel, High rate capability of SiOC ceramic aerogels with tailored porosity as anode materials for Li-ion batteries. Electrochimica Acta, 2015. 157: p. 41-45.

[8] Zhang, X., D. Chang, J. Liu, and Y. Luo, Conducting polymer aerogels from supercritical CO2 drying PEDOT-PSS hydrogels. Journal of Materials Chemistry, 2010. 20(24): p. 5080-5085.

[9] Meador, M.A.B., C.R. Alemán, K. Hanson, N. Ramirez, S.L. Vivod, N. Wilmoth, and L. McCorkle, Polyimide aerogels with amide cross-links: a low cost alternative for mechanically strong polymer aerogels. ACS applied materials & interfaces, 2015. 7(2): p. 1240-1249.

[10] Bhandari, J., H. Mishra, P.K. Mishra, R. Wimmer, F.J. Ahmad, and S. Talegaonkar, Cellulose nanofiber aerogel as a promising biomaterial for customized oral drug delivery. International journal of nanomedicine, 2017. 12: p. 2021.

[11] Lee, S., M.-J. Jeong, and K.-Y. Kang, Preparation of cellulose aerogels as a nano-biomaterial from lignocellulosic biomass. Journal of the Korean Physical Society, 2015. 67(4): p. 738-741.

[12] Dash, R., Y. Li, and A.J. Ragauskas, Cellulose nanowhisker foams by freeze casting. Carbohydrate polymers, 2012. 88(2): p. 789-792.

[13] Donius, A.E., A. Liu, L.A. Berglund, and U.G. Wegst, Superior mechanical performance of highly porous, anisotropic nanocellulose–montmorillonite aerogels prepared by freeze casting. Journal of the mechanical behavior of biomedical materials, 2014. 37: p. 88-99.

[14] Wicklein, B., A. Kocjan, G. Salazar-Alvarez, F. Carosio, G. Camino, M. Antonietti, and L. Bergström, Thermally insulating and fire-retardant lightweight anisotropic foams based on nanocellulose and graphene oxide. Nature nanotechnology, 2015. 10(3): p. 277-283.

[15] Munier, P., K. Gordeyeva, L. Bergström, and A.B. Fall, Directional freezing of nanocellulose dispersions aligns the rod-like particles and produces low-density and robust particle networks. Biomacromolecules, 2016. 17(5): p. 1875-1881.

[16] Standard, A., Standard terminology for additive manufacturing technologies. ASTM International F2792-12a, 2012.

[17] Huang, S.H., P. Liu, A. Mokasdar, and L. Hou, Additive manufacturing and its societal impact: a literature review. The International Journal of Advanced Manufacturing Technology, 2013. 67(5): p. 1191-1203.

[18] Wong, K.V. and A. Hernandez, A review of additive manufacturing. International scholarly research notices, 2012. 2012.

[19] Negi, S., S. Dhiman, and R.K. Sharma, Basics, applications and future of additive manufacturing technologies: A review. Journal of Manufacturing Technology Research, 2013. 5(1/2): p. 75.

[20] Salimian, S., A. Zadhoush, M. Naeimirad, R. Kotek, and S. Ramakrishna, A review on aerogel: 3D nanoporous structured fillers in polymer-based nanocomposites. Polymer Composites, 2018. 39(10): p. 3383-3408.

[21] Du, A., B. Zhou, Z. Zhang, and J. Shen, A special material or a new state of matter: a review and reconsideration of the aerogel. Materials, 2013. 6(3): p. 941-968.

[22] Barrios, E., D. Fox, Y.Y. Li Sip, R. Catarata, J.E. Calderon, N. Azim, S. Afrin, Z. Zhang, and L. Zhai, Nanomaterials in advanced, high-performance aerogel composites: A review. Polymers, 2019. 11(4): p. 726.

[23] Tian, X., J. Jin, S. Yuan, C.K. Chua, S.B. Tor, and K. Zhou, Emerging 3D-printed electrochemical energy storage devices: a critical review. Advanced Energy Materials, 2017. 7(17): p. 1700127.

[24] Yao, B., S. Chandrasekaran, H. Zhang, A. Ma, J. Kang, L. Zhang, X. Lu, F. Qian, C. Zhu, and E.B. Duoss, 3D-printed structure boosts the kinetics and intrinsic capacitance of pseudocapacitive graphene aerogels. Advanced Materials, 2020. 32(8): p. 1906652.

[25] Lee, H. and G. Kim, Cryogenically fabricated three-dimensional chitosan scaffolds with pore size-controlled structures for biomedical applications. Carbohydrate polymers, 2011. 85(4): p. 817-823.

[26] Lacey, S.D., D.J. Kirsch, Y. Li, J.T. Morgenstern, B.C. Zarket, Y. Yao, J. Dai, L.Q. Garcia, B. Liu, and T. Gao, Extrusion-based 3D printing of hierarchically porous advanced battery electrodes. Advanced Materials, 2018. 30(12): p. 1705651.

[27] Mohammed, A.K., S. Usgaonkar, F. Kanheerampockil, S. Karak, A. Halder, M. Tharkar, M. Addicoat, T.G. Ajithkumar, and R. Banerjee, Connecting microscopic structures, mesoscale assemblies, and macroscopic architectures in 3D-printed hierarchical porous covalent organic framework foams. Journal of the American Chemical Society, 2020. 142(18): p. 8252-8261.

[28] Lei, D., Y. Yang, Z. Liu, S. Chen, B. Song, A. Shen, B. Yang, S. Li, Z. Yuan, and Q. Qi, A general strategy of 3D printing thermosets for diverse applications. Materials Horizons, 2019. 6(2): p. 394-404.

[29] Ning, L. and X. Chen, A brief review of extrusion-based tissue scaffold bio-printing. Biotechnology journal, 2017. 12(8): p. 1600671.

[30] Zhang, Q., F. Zhang, S.P. Medarametla, H. Li, C. Zhou, and D. Lin, 3D printing of graphene aerogels. Small, 2016. 12(13): p. 1702-1708.

[31] Wang, X., M. Jiang, Z. Zhou, J. Gou, and D. Hui, 3D printing of polymer matrix composites: A review and prospective. Composites Part B: Engineering, 2017. 110: p. 442-458.

[32] Hensleigh, R.M., H. Cui, J.S. Oakdale, C.Y. Jianchao, P.G. Campbell, E.B. Duoss, C.M. Spadaccini, X. Zheng, and M.A. Worsley, Additive manufacturing of complex micro-architected graphene aerogels. Materials Horizons, 2018. 5(6): p. 1035-1041.

[33] Xiong, Z., Y. Yan, S. Wang, R. Zhang, and C. Zhang, Fabrication of porous scaffolds for bone tissue engineering via low-temperature deposition. Scripta Materialia, 2002. 46(11): p. 771-776.

[34] Pham, C.B., K.F. Leong, T.C. Lim, and K.S. Chian, Rapid freeze prototyping technique in bio-plotters for tissue scaffold fabrication. Rapid Prototyping Journal, 2008.

[35] Kim, G., S. Ahn, H. Yoon, Y. Kim, and W. Chun, A cryogenic direct-plotting system for fabrication of 3D collagen scaffolds for tissue engineering. Journal of Materials Chemistry, 2009. 19(46): p. 8817-8823.

[36] Rees, A., L.C. Powell, G. Chinga-Carrasco, D.T. Gethin, K. Syverud, K.E. Hill, and D.W. Thomas, 3D bioprinting of carboxymethylated-periodate oxidized nanocellulose constructs for wound dressing applications. BioMed research international, 2015. 2015.

[37] García-Tuñon, E., S. Barg, J. Franco, R. Bell, S. Eslava, E. D'Elia, R.C. Maher, F. Guitian, and E. Saiz, Printing in three dimensions with graphene. Advanced materials, 2015. 27(10): p. 1688-1693.

[38] Lin, Y., F. Liu, G. Casano, R. Bhavsar, I.A. Kinloch, and B. Derby, Pristine graphene aerogels by room-temperature freeze gelation. Advanced Materials, 2016. 28(36): p. 7993-8000.

[39] Ge, Y., T. Zhang, B. Zhou, H. Wang, Z. Zhang, J. Shen, and A. Du, Nanostructured resorcinol-formaldehyde ink for 3D direct writing. Journal of Materials Research, 2018. 33(14): p. 2052-2061.

[40] Yang, W., J. Yang, J.J. Byun, F.P. Moissinac, J. Xu, S.J. Haigh, M. Domingos, M.A. Bissett, R.A. Dryfe, and S. Barg, 3D printing of freestanding MXene architectures for current-collector-free supercapacitors. Advanced materials, 2019. 31(37): p. 1902725.

[41] Song, X., H. Tetik, T. Jirakittsonthon, P. Parandoush, G. Yang, D. Lee, S. Ryu, S. Lei, M.L. Weiss, and D. Lin, Biomimetic 3D printing of hierarchical and interconnected porous hydroxyapatite structures with high mechanical strength for bone cell culture. Advanced Engineering Materials, 2019. 21(1): p. 1800678.

[42] Saeed, S., R.M. Al-Sobaihi, M.F. Bertino, L.S. White, and K.M. Saoud, Laser induced instantaneous gelation: aerogels for 3D printing. Journal of Materials Chemistry A, 2015. 3(34): p. 17606-17611.

[43] Morris, V.B., S. Nimbalkar, M. Younesi, P. McClellan, and O. Akkus, Mechanical properties, cytocompatibility and manufacturability of chitosan: PEGDA hybrid-gel scaffolds by stereolithography. Annals of biomedical engineering, 2017. 45(1): p. 286-296.

[44] Yan, P., E. Brown, Q. Su, J. Li, J. Wang, C. Xu, C. Zhou, and D. Lin, 3D printing hierarchical silver nanowire aerogel with highly compressive resilience and tensile elongation through tunable poisson's ratio. Small, 2017. 13(38): p. 1701756.

[45] Brown, E., P. Yan, H. Tekik, A. Elangovan, J. Wang, D. Lin, and J. Li, 3D printing of hybrid MoS2-graphene aerogels as highly porous electrode materials for sodium ion battery anodes. Materials & Design, 2019. 170: p. 107689.

[46] Michaeli, W. and C. Hopmann, Extrusion dies for plastics and rubber. 2016: Hanser Publishers Munich.

[47] M'barki, A., L. Bocquet, and A. Stevenson, Linking rheology and printability for dense and strong ceramics by direct ink writing. Scientific reports, 2017. 7(1): p. 1-10.

[48] Zhang, C., K. Shen, B. Li, S. Li, and S. Yang, Continuously 3D printed quantum dot-based electrodes for lithium storage with ultrahigh capacities. Journal of Materials Chemistry A, 2018. 6(41): p. 19960-19966.

[49] Akuzum, B., K. Maleski, B. Anasori, P. Lelyukh, N.J. Alvarez, E.C. Kumbur, and Y. Gogotsi, Rheological characteristics of 2D titanium carbide (MXene) dispersions: a guide for processing MXenes. ACS nano, 2018. 12(3): p. 2685-2694.

[50] Håkansson, K.M., I.C. Henriksson, C. de la Peña Vázquez, V. Kuzmenko, K. Markstedt, P. Enoksson, and P. Gatenholm, Solidification of 3D printed nanofibril hydrogels into functional 3D cellulose structures. Advanced Materials Technologies, 2016. 1(7): p. 1600096.

[51] Ma, J., P. Wang, L. Dong, Y. Ruan, and H. Lu, Highly conductive, mechanically strong graphene monolith assembled by three-dimensional printing of large graphene oxide. Journal of colloid and interface science, 2019. 534: p. 12-19.

[52] Chandrasekaran, S., B. Yao, T. Liu, W. Xiao, Y. Song, F. Qian, C. Zhu, E.B. Duoss, C.M. Spadaccini, and Y. Li, Direct ink writing of organic and carbon aerogels. Materials Horizons, 2018. 5(6): p. 1166-1175.

[53] Jiang, Y., Z. Xu, T. Huang, Y. Liu, F. Guo, J. Xi, W. Gao, and C. Gao, Direct 3D printing of ultralight graphene oxide aerogel microlattices. Advanced Functional Materials, 2018. 28(16): p. 1707024.

[54] Kam, D., M. Chasnitsky, C. Nowogrodski, I. Braslavsky, T. Abitbol, S. Magdassi, and O. Shoseyov, Direct CRYO writing of aerogels via 3D Printing of aligned cellulose nanocrystals inspired by the plant cell wall. Colloids and Interfaces, 2019. 3(2): p. 46.

[55] Li, V.C.-F., C.K. Dunn, Z. Zhang, Y. Deng, and H.J. Qi, Direct ink write (DIW) 3D printed cellulose nanocrystal aerogel structures. Scientific reports, 2017. 7(1): p. 1-8.

[56] Li, V.C., A. Mulyadi, C.K. Dunn, Y. Deng, and H.J. Qi, Direct ink write 3D printed cellulose nanofiber aerogel structures with highly deformable, shape recoverable, and functionalizable properties. ACS Sustainable Chemistry & Engineering, 2018. 6(2): p. 2011-2022.

[57] Fu, K., Y. Wang, C. Yan, Y. Yao, Y. Chen, J. Dai, S. Lacey, Y. Wang, J. Wan, and T. Li, Graphene oxide-based electrode inks for 3D-printed lithium-ion batteries. Advanced Materials, 2016. 28(13): p. 2587-2594.

[58] Li, X., H. Li, X. Fan, X. Shi, and J. Liang, 3D-printed stretchable micro-supercapacitor with remarkable areal performance. Advanced Energy Materials, 2020. 10(14): p. 1903794.

[59] Munir, N., R. Larsen, and A. Callanan, Fabrication of 3D cryo-printed scaffolds using low-temperature deposition manufacturing for cartilage tissue engineering. Bioprinting, 2018. 10: p. e00033.

[60] Chinga-Carrasco, G., N.V. Ehman, D. Filgueira, J. Johansson, M.E. Vallejos, F.E. Felissia, J. Håkansson, and M.C. Area, Bagasse—A major agro-industrial residue as potential resource for nanocellulose inks for 3D printing of wound dressing devices. Additive Manufacturing, 2019. 28: p. 267-274.

[61] Huan, S., R. Ajdary, L. Bai, V. Klar, and O.J. Rojas, Low solids emulsion gels based on nanocellulose for 3D-printing. Biomacromolecules, 2018. 20(2): p. 635-644.

[62] Yu, Y., S. Hua, M. Yang, Z. Fu, S. Teng, K. Niu, Q. Zhao, and C. Yi, Fabrication and characterization of electrospinning/3D printing bone tissue engineering scaffold. RSC advances, 2016. 6(112): p. 110557-110565.

[63] Garcia-Tunon, E., E. Feilden, H. Zheng, E. D'Elia, A. Leong, and E. Saiz, Graphene oxide: an all-in-one processing additive for 3D printing. ACS applied materials & interfaces, 2017. 9(38): p. 32977-32989.

[64] Tang, X., H. Zhou, Z. Cai, D. Cheng, P. He, P. Xie, D. Zhang, and T. Fan, Generalized 3D printing of graphene-based mixed-dimensional hybrid aerogels. ACS nano, 2018. 12(4): p. 3502-3511.

[65] Rocha, V.G., E. Garcia-Tunon, C. Botas, F. Markoulidis, E. Feilden, E. D'Elia, N. Ni, M. Shaffer, and E. Saiz, Multimaterial 3D printing of graphene-based electrodes for electrochemical energy storage using thermoresponsive inks. ACS applied materials & interfaces, 2017. 9(42): p. 37136-37145.

[66] Yang, J., H. Wang, B. Zhou, J. Shen, Z. Zhang, and A. Du, Versatile Direct Writing of Aerogel-Based Sol–Gel Inks. Langmuir, 2021. 37(6): p. 2129-2139.

[67] Liu, L., Z. Xiong, Y. Yan, R. Zhang, X. Wang, and L. Jin, Multinozzle low-temperature deposition system for construction of gradient tissue engineering scaffolds. Journal of Biomedical Materials Research Part B: Applied Biomaterials: An Official Journal of The Society for Biomaterials, The Japanese Society for Biomaterials, and The Australian Society for Biomaterials and the Korean Society for Biomaterials, 2009. 88(1): p. 254-263.

[68] Zhao, J., Y. Zhang, X. Zhao, R. Wang, J. Xie, C. Yang, J. Wang, Q. Zhang, L. Li, and C. Lu, Direct ink writing of adjustable electrochemical energy storage device with high gravimetric energy densities. Advanced Functional Materials, 2019. 29(26): p. 1900809.

[69] Li, L., Y. Zhu, and J. Yang, 3D bioprinting of cellulose with controlled porous structures from NMMO. Materials Letters, 2018. 210: p. 136-138.

[70] Zhu, C., T. Liu, F. Qian, T.Y.-J. Han, E.B. Duoss, J.D. Kuntz, C.M. Spadaccini, M.A. Worsley, and Y. Li, Supercapacitors based on three-dimensional hierarchical graphene aerogels with periodic macropores. Nano letters, 2016. 16(6): p. 3448-3456.

[71] Zhu, C., T. Han, E.B. Duoss, A.M. Golobic, J.D. Kuntz, C.M. Spadaccini, and M.A. Worsley, Highly compressible 3D periodic graphene aerogel microlattices. Nature communications, 2015. 6(1): p. 1-8.

[72] He, P., X. Tang, L. Chen, P. Xie, L. He, H. Zhou, D. Zhang, and T. Fan, Patterned carbon nitride–based hybrid aerogel membranes via 3D printing for broadband solar wastewater remediation. Advanced Functional Materials, 2018. 28(29): p. 1801121.

[73] Liu, D., C. Chen, Y. Zhou, Y. Bao, R. Wang, Y. Liu, S. He, H. Huang, C. Zhang, and B. Foster, 3D-Printed, High-Porosity, High-Strength Graphite Aerogel. Small Methods, 2021. 5(7): p. 2001188.

[74] Scotti, K.L. and D.C. Dunand, Freeze casting–A review of processing, microstructure and properties via the open data repository, FreezeCasting. net. Progress in Materials Science, 2018. 94: p. 243-305.

[75] Zhou, Y., S. Fu, Y. Pu, S. Pan, and A.J. Ragauskas, Preparation of aligned porous chitin nanowhisker foams by directional freeze–casting technique. Carbohydrate polymers, 2014. 112: p. 277-283.

[76] Hsieh, C.-T., C.-Y. Liao, N.-T. Dai, C.-S. Tseng, B.L. Yen, and S.-h. Hsu, 3D printing of tubular scaffolds with elasticity and complex structure from multiple waterborne polyurethanes for tracheal tissue engineering. Applied Materials Today, 2018. 12: p. 330-341.

[77] Liao, C.-Y., W.-J. Wu, C.-T. Hsieh, C.-S. Tseng, N.-T. Dai, and S.-h. Hsu, Design and development of a novel frozen-form additive manufacturing system for tissue engineering applications. 3D Printing and Additive Manufacturing, 2016. 3(4): p. 216-225.

[78] Serdeczny, M.P., R. Comminal, D.B. Pedersen, and J. Spangenberg, Experimental validation of a numerical model for the strand shape in material extrusion additive manufacturing. Additive Manufacturing, 2018. 24: p. 145-153.

[79] Lewis, J.A., J.E. Smay, J. Stuecker, and J. Cesarano, Direct ink writing of three-dimensional ceramic structures. Journal of the American Ceramic Society, 2006. 89(12): p. 3599-3609.

[80] Li, J., F. Rossignol, and J. Macdonald, Inkjet printing for biosensor fabrication: combining chemistry and technology for advanced manufacturing. Lab on a Chip, 2015. 15(12): p. 2538-2558.

[81] Eshkalak, S.K., A. Chinnappan, W. Jayathilaka, M. Khatibzadeh, E. Kowsari, and S. Ramakrishna, A review on inkjet printing of CNT composites for smart applications. Applied Materials Today, 2017. 9: p. 372-386.

[82] Sun, J., J.Y. Fuh, E. Thian, G.S. Hong, Y. Wong, R. Yang, and K.K. Tan, Fabrication of electronic devices with multi-material drop-on-demand dispensing system. International Journal of Computer Integrated Manufacturing, 2013. 26(10): p. 897-906.

[83] Rose, D., Microdispensing technologies in drug discovery. Drug discovery today, 1999. 4(9): p. 411-419.

[84] Wang, C., R.I. Tomov, R. Vasant Kumar, and B.A. Glowacki, Inkjet printing of gadolinium-doped ceria electrolyte on NiO-YSZ substrates for solid oxide fuel cell applications. Journal of materials science, 2011. 46(21): p. 6889-6896.

[85] Wang, C., S.C. Hopkins, R.I. Tomov, R.V. Kumar, and B.A. Glowacki, Optimisation of CGO suspensions for inkjet-printed SOFC electrolytes. Journal of the European Ceramic Society, 2012. 32(10): p. 2317-2324.

[86] Nayak, L., S. Mohanty, S.K. Nayak, and A. Ramadoss, A review on inkjet printing of nanoparticle inks for flexible electronics. Journal of Materials Chemistry C, 2019. 7(29): p. 8771-8795.

[87] Derby, B., Inkjet printing ceramics: From drops to solid. Journal of the European Ceramic Society, 2011. 31(14): p. 2543-2550.

[88] Cummins, G. and M.P. Desmulliez, Inkjet printing of conductive materials: a review. Circuit world, 2012.

[89] Derby, B., Inkjet printing of functional and structural materials: fluid property requirements, feature stability, and resolution. Annual Review of Materials Research, 2010. 40: p. 395-414.

[90] Guo, Y., H.S. Patanwala, B. Bognet, and A.W. Ma, Inkjet and inkjet-based 3D printing: connecting fluid properties and printing performance. Rapid Prototyping Journal, 2017.

[91] Reis, N. and B. Derby, Ink jet deposition of ceramic suspensions: Modeling and experiments of droplet formation. MRS Online Proceedings Library (OPL), 2000. 625.

[92] van Dam, D.B. and C. Le Clerc, Experimental study of the impact of an ink-jet printed droplet on a solid substrate. Physics of Fluids, 2004. 16(9): p. 3403-3414.

[93] Stringer, J. and B. Derby, Formation and stability of lines produced by inkjet printing. Langmuir, 2010. 26(12): p. 10365-10372.

[94] Moon, Y.J., H. Kang, S.H. Lee, K. Kang, Y.J. Cho, J.Y. Hwang, and S.J. Moon, Effect of contact angle and drop spacing on the bulging frequency of inkjet-printed silver lines on FC-coated glass. Journal of Mechanical Science and Technology, 2014. 28(4): p. 1441-1448.

[95] Duineveld, P.C., The stability of ink-jet printed lines of liquid with zero receding contact angle on a homogeneous substrate. Journal of Fluid Mechanics, 2003. 477: p. 175-200.

[96] Soltman, D. and V. Subramanian, Inkjet-printed line morphologies and temperature control of the coffee ring effect. Langmuir, 2008. 24(5): p. 2224-2231.

[97] Tetik, H., G. Yang, W. Tan, A. Fong, S. Lei, J.N. Weker, and D. Lin, High speed in-situ X-ray imaging of 3D freeze printing of aerogels. Additive Manufacturing, 2020. 36: p. 101513.

[98] Noguera, R., M. Lejeune, and T. Chartier, 3D fine scale ceramic components formed by ink-jet prototyping process. Journal of the European Ceramic Society, 2005. 25(12): p. 2055-2059.

[99] Ma, C., R. Wang, H. Tetik, S. Gao, M. Wu, Z. Tang, D. Lin, D. Ding, and W. Wu, Hybrid nanomanufacturing of mixed-dimensional manganese oxide/graphene aerogel macroporous hierarchy for ultralight efficient supercapacitor electrodes in self-powered ubiquitous nanosystems. Nano Energy, 2019. 66: p. 104124.

[100] Tetik, H., K. Zhao, N. Shah, and D. Lin, 3D freeze-printed cellulose-based aerogels: Obtaining truly 3D shapes, and functionalization with cross-linking and conductive additives. Journal of Manufacturing Processes, 2021. 68: p. 445-453.

[101] Vaezi, M., H. Seitz, and S. Yang, A review on 3D micro-additive manufacturing technologies. The International Journal of Advanced Manufacturing Technology, 2013. 67(5): p. 1721-1754.

[102] Melchels, F.P., J. Feijen, and D.W. Grijpma, A review on stereolithography and its applications in biomedical engineering. Biomaterials, 2010. 31(24): p. 6121-6130.

[103] Manapat, J.Z., Q. Chen, P. Ye, and R.C. Advincula, 3D printing of polymer nanocomposites via stereolithography. Macromolecular Materials and Engineering, 2017. 302(9): p. 1600553.

[104] Zheng, X., J. Deotte, M.P. Alonso, G.R. Farquar, T.H. Weisgraber, S. Gemberling, H. Lee, N. Fang, and C.M. Spadaccini, Design and optimization of a light-emitting diode projection micro-stereolithography three-dimensional manufacturing system. Review of Scientific Instruments, 2012. 83(12): p. 125001.

[105] Jacobs, P.F. Fundamentals of stereolithography. in 1992 International Solid Freeform Fabrication Symposium. 1992.

[106] Anderson, A.M. and M.K. Carroll, Hydrophobic silica aerogels: review of synthesis, properties and applications. Aerogels handbook, 2011: p. 47-77.

[107] Maleki, H., L. Durães, and A. Portugal, An overview on silica aerogels synthesis and different mechanical reinforcing strategies. Journal of Non-Crystalline Solids, 2014. 385: p. 55-74.

[108] Lamy-Mendes, A., R.F. Silva, and L. Durães, Advances in carbon nanostructure–silica aerogel composites: a review. Journal of Materials Chemistry A, 2018. 6(4): p. 1340-1369.

[109] Dorcheh, A.S. and M. Abbasi, Silica aerogel; synthesis, properties and characterization. Journal of materials processing technology, 2008. 199(1-3): p. 10-26.

[110] Gurav, J.L., I.-K. Jung, H.-H. Park, E.S. Kang, and D.Y. Nadargi, Silica aerogel: synthesis and applications. Journal of Nanomaterials, 2010. 2010.

[111] Lopez-Iglesias, C., A.M. Casielles, A. Altay, R. Bettini, C. Alvarez-Lorenzo, and C.A. García-González, From the printer to the lungs: Inkjet-printed aerogel particles for pulmonary delivery. Chemical Engineering Journal, 2019. 357: p. 559-566.

[112] Zhao, S., G. Siqueira, S. Drdova, D. Norris, C. Ubert, A. Bonnin, S. Galmarini, M. Ganobjak, Z. Pan, and S. Brunner, Additive manufacturing of silica aerogels. Nature, 2020. 584(7821): p. 387-392.

[113] Cheng, Q., Y. Liu, J. Lyu, Q. Lu, X. Zhang, and W. Song, 3D printing-directed auxetic Kevlar aerogel architectures with multiple functionalization options. Journal of Materials Chemistry A, 2020. 8(28): p. 14243-14253.

[114] Deville, S., Ice-templating, freeze casting: Beyond materials processing. Journal of Materials Research, 2013. 28(17): p. 2202-2219.

[115] Li, W., K. Lu, and J. Walz, Freeze casting of porous materials: review of critical factors in microstructure evolution. International materials reviews, 2012. 57(1): p. 37-60.

[116] Françon, H., Z. Wang, A. Marais, K. Mystek, A. Piper, H. Granberg, A. Malti, P. Gatenholm, P.A. Larsson, and L. Wågberg, Ambient-Dried, 3D-Printable and Electrically Conducting Cellulose Nanofiber Aerogels by Inclusion of Functional Polymers. Advanced Functional Materials, 2020. 30(12): p. 1909383.

[117] Guo, Z., R. Yang, T. Wang, L. An, S. Ren, and C. Zhou, Cost-effective additive manufacturing of ambient pressure-dried silica aerogel. Journal of Manufacturing Science and Engineering, 2021. 143(1).

[118] Fu, S., X. Du, M. Zhu, Z. Tian, D. Wei, and Y. Zhu, 3D printing of layered mesoporous bioactive glass/sodium alginate-sodium alginate scaffolds with controllable dual-drug release behaviors. Biomedical Materials, 2019. 14(6): p. 065011.

[119] Guo, F., Y. Jiang, Z. Xu, Y. Xiao, B. Fang, Y. Liu, W. Gao, P. Zhao, H. Wang, and C. Gao, Highly stretchable carbon aerogels. Nature communications, 2018. 9(1): p. 1-9.

[120] An, B., Y. Ma, W. Li, M. Su, F. Li, and Y. Song, Three-dimensional multi-recognition flexible wearable sensor via graphene aerogel printing. Chemical Communications, 2016. 52(73): p. 10948-10951.

[121] Liu, S., X. Shi, X. Li, Y. Sun, J. Zhu, Q. Pei, J. Liang, and Y. Chen, A general gelation strategy for 1D nanowires: dynamically stable functional gels for 3D printing flexible electronics. Nanoscale, 2018. 10(43): p. 20096-20107.

[122] Shen, K., H. Mei, B. Li, J. Ding, and S. Yang, 3D printing sulfur copolymer-graphene architectures for Li-S batteries. Advanced Energy Materials, 2018. 8(4): p. 1701527.

[123] Yao, B., S. Chandrasekaran, J. Zhang, W. Xiao, F. Qian, C. Zhu, E.B. Duoss, C.M. Spadaccini, M.A. Worsley, and Y. Li, Efficient 3D printed pseudocapacitive electrodes with ultrahigh MnO2 loading. Joule, 2019. 3(2): p. 459-470.

[124] Qi, Z., J. Ye, W. Chen, J. Biener, E.B. Duoss, C.M. Spadaccini, M.A. Worsley, and C. Zhu, 3D-Printed, Superelastic Polypyrrole–Graphene Electrodes with Ultrahigh Areal Capacitance for Electrochemical Energy Storage. Advanced Materials Technologies, 2018. 3(7): p. 1800053.

[125] Pires, V.F., E. Romero-Cadaval, D. Vinnikov, I. Roasto, and J. Martins, Power converter interfaces for electrochemical energy storage systems–A review. Energy conversion and management, 2014. 86: p. 453-475.

[126] Zhao, H. and Y. Lei, 3D Nanostructures for the Next Generation of High-Performance Nanodevices for Electrochemical Energy Conversion and Storage. Advanced Energy Materials, 2020. 10(28): p. 2001460.

[127] Li, F., L. Xie, G. Sun, Q. Kong, F. Su, Y. Cao, J. Wei, A. Ahmad, X. Guo, and C.-M. Chen, Resorcinol-formaldehyde based carbon aerogel: Preparation, structure and applications in energy storage devices. Microporous and Mesoporous Materials, 2019. 279: p. 293-315.

[128] Pang, Y., Y. Cao, Y. Chu, M. Liu, K. Snyder, D. MacKenzie, and C. Cao, Additive manufacturing of batteries. Advanced Functional Materials, 2020. 30(1): p. 1906244.

[129] Shao, Y., M.F. El-Kady, J. Sun, Y. Li, Q. Zhang, M. Zhu, H. Wang, B. Dunn, and R.B. Kaner, Design and mechanisms of asymmetric supercapacitors. Chemical reviews, 2018. 118(18): p. 9233-9280.

[130] Ke, Q. and J. Wang, Graphene-based materials for supercapacitor electrodes–A review. Journal of Materiomics, 2016. 2(1): p. 37-54.

[131] Zhao, H. and Y. Lei, 3D Nanostructures for the Next Generation of High-Performance Nanodevices for Electrochemical Energy Conversion and Storage. Advanced Energy Materials, 2020. 10(28): p. 2001460.

[132] Chen, Q., R. Xu, Z. He, K. Zhao, and L. Pan, Printing 3D gel polymer electrolyte in lithium-ion microbattery using stereolithography. Journal of The Electrochemical Society, 2017. 164(9): p. A1852.

[133] Meng, Q., H. Wu, Y. Meng, K. Xie, Z. Wei, and Z. Guo, High-Performance All-Carbon Yarn Micro-Supercapacitor for an Integrated Energy System. Advanced Materials, 2014. 26(24): p. 4100-4106.

[134] Li, W., Y. Li, M. Su, B. An, J. Liu, D. Su, L. Li, F. Li, and Y. Song, Printing assembly and structural regulation of graphene towards three-dimensional flexible micro-supercapacitors. Journal of Materials Chemistry A, 2017. 5(31): p. 16281-16288.

[135] Sun, K., T.S. Wei, B.Y. Ahn, J.Y. Seo, S.J. Dillon, and J.A. Lewis, 3D printing of interdigitated Li-Ion microbattery architectures. Advanced materials, 2013. 25(33): p. 4539-4543.

[136] Shen, K., J. Ding, and S. Yang, 3D printing quasi-solid-state asymmetric micro-supercapacitors with ultrahigh areal energy density. Advanced Energy Materials, 2018. 8(20): p. 1800408.

[137] He, Y., W. Chen, X. Li, Z. Zhang, J. Fu, C. Zhao, and E. Xie, Freestanding three-dimensional graphene/MnO2 composite networks as ultralight and flexible supercapacitor electrodes. ACS nano, 2013. 7(1): p. 174-182.

[138] Lu, X., T. Zhai, X. Zhang, Y. Shen, L. Yuan, B. Hu, L. Gong, J. Chen, Y. Gao, and J. Zhou, WO3–x@ Au@ MnO2 core–shell nanowires on carbon fabric for high-performance flexible supercapacitors. Advanced materials, 2012. 24(7): p. 938-944.

[139] Tang, X., C. Zhu, D. Cheng, H. Zhou, X. Liu, P. Xie, Q. Zhao, D. Zhang, and T. Fan, Architectured leaf-inspired Ni0. 33Co0. 66S2/graphene aerogels via 3D printing for high-performance energy storage. Advanced Functional Materials, 2018. 28(51): p. 1805057.

[140] Yuan, S., W. Fan, D. Wang, L. Zhang, Y.-E. Miao, F. Lai, and T. Liu, 3D printed carbon aerogel microlattices for customizable supercapacitors with high areal capacitance. Journal of Materials Chemistry A, 2021. 9(1): p. 423-432.

[141] Kuang, Y., C. Chen, D. Kirsch, and L. Hu, Thick electrode batteries: principles, opportunities, and challenges. Advanced Energy Materials, 2019. 9(33): p. 1901457.

[142] Sun, H., J. Zhu, D. Baumann, L. Peng, Y. Xu, I. Shakir, Y. Huang, and X. Duan, Hierarchical 3D electrodes for electrochemical energy storage. Nature Reviews Materials, 2019. 4(1): p. 45-60.

[143] Cao, D., Y. Xing, K. Tantratian, X. Wang, Y. Ma, A. Mukhopadhyay, Z. Cheng, Q. Zhang, Y. Jiao, and L. Chen, 3D printed high-performance lithium metal microbatteries enabled by nanocellulose. Advanced Materials, 2019. 31(14): p. 1807313.

[144] Ding, J., K. Shen, Z. Du, B. Li, and S. Yang, 3D-printed hierarchical porous frameworks for sodium storage. ACS applied materials & interfaces, 2017. 9(48): p. 41871-41877.

[145] Shen, K., B. Li, and S. Yang, 3D printing dendrite-free lithium anodes based on the nucleated MXene arrays. Energy Storage Materials, 2020. 24: p. 670-675.

[146] Yan, J., G. Zhi, D. Kong, H. Wang, T. Xu, J. Zang, W. Shen, J. Xu, Y. Shi, and S. Dai, 3D printed rGO/CNT microlattice aerogel for a dendrite-free sodium metal anode. Journal of Materials Chemistry A, 2020. 8(38): p. 19843-19854.

[147] Wu, C., H. Tetik, J. Cheng, W. Ding, H. Guo, X. Tao, N. Zhou, Y. Zi, Z. Wu, and H. Wu, Electrohydrodynamic jet printing driven by a triboelectric nanogenerator. Advanced Functional Materials, 2019. 29(22): p. 1901102.

[148] Mi, H.-Y., X. Jing, Q. Zheng, L. Fang, H.-X. Huang, L.-S. Turng, and S. Gong, High-performance flexible triboelectric nanogenerator based on porous aerogels and electrospun nanofibers for energy harvesting and sensitive self-powered sensing. Nano Energy, 2018. 48: p. 327-336.

[149] Torres, F.G. and G.E. De-la-Torre, Polysaccharide-based triboelectric nanogenerators: a review. Carbohydrate Polymers, 2021. 251: p. 117055.

[150] Qian, C., L. Li, M. Gao, H. Yang, Z. Cai, B. Chen, Z. Xiang, Z. Zhang, and Y. Song, All-printed 3D hierarchically structured cellulose aerogel based triboelectric nanogenerator for multi-functional sensors. Nano Energy, 2019. 63: p. 103885.

[151] Peng, M., Z. Wen, L. Xie, J. Cheng, Z. Jia, D. Shi, H. Zeng, B. Zhao, Z. Liang, and T. Li, 3D printing of ultralight biomimetic hierarchical graphene materials with exceptional stiffness and resilience. Advanced Materials, 2019. 31(35): p. 1902930.

[152] Yang, S., K.-F. Leong, Z. Du, and C.-K. Chua, The design of scaffolds for use in tissue engineering. Part I. Traditional factors. Tissue engineering, 2001. 7(6): p. 679-689.

[153] Hollister, S.J., Porous scaffold design for tissue engineering. Nature materials, 2005. 4(7): p. 518-524.

[154] Sachlos, E. and J. Czernuszka, Making tissue engineering scaffolds work. Review: the application of solid freeform fabrication technology to the production of tissue engineering scaffolds. Eur Cell Mater, 2003. 5(29): p. 39-40.

[155] Hutmacher, D.W., M. Sittinger, and M.V. Risbud, Scaffold-based tissue engineering: rationale for computer-aided design and solid free-form fabrication systems. TRENDS in Biotechnology, 2004. 22(7): p. 354-362.

[156] Dhandayuthapani, B., Y. Yoshida, T. Maekawa, and D.S. Kumar, Polymeric scaffolds in tissue engineering application: a review. International journal of polymer science, 2011. 2011.

[157] Suh, J.-K.F. and H.W. Matthew, Application of chitosan-based polysaccharide biomaterials in cartilage tissue engineering: a review. Biomaterials, 2000. 21(24): p. 2589-2598.

[158] Van Vlierberghe, S., P. Dubruel, and E. Schacht, Biopolymer-based hydrogels as scaffolds for tissue engineering applications: a review. Biomacromolecules, 2011. 12(5): p. 1387-1408.

[159] Peltola, S.M., F.P. Melchels, D.W. Grijpma, and M. Kellomäki, A review of rapid prototyping techniques for tissue engineering purposes. Annals of medicine, 2008. 40(4): p. 268-280.

[160] Armentano, I., M. Dottori, E. Fortunati, S. Mattioli, and J. Kenny, Biodegradable polymer matrix nanocomposites for tissue engineering: a review. Polymer degradation and stability, 2010. 95(11): p. 2126-2146.

[161] Collins, M.N. and C. Birkinshaw, Hyaluronic acid based scaffolds for tissue engineering—A review. Carbohydrate polymers, 2013. 92(2): p. 1262-1279.

[162] Lee, K., E.A. Silva, and D.J. Mooney, Growth factor delivery-based tissue engineering: general approaches and a review of recent developments. Journal of the Royal Society Interface, 2011. 8(55): p. 153-170.

[163] Venkatesan, J., I. Bhatnagar, P. Manivasagan, K.-H. Kang, and S.-K. Kim, Alginate composites for bone tissue engineering: a review. International journal of biological macromolecules, 2015. 72: p. 269-281.

[164] Ang, T., F. Sultana, D. Hutmacher, Y.S. Wong, J. Fuh, X. Mo, H.T. Loh, E. Burdet, and S.-H. Teoh, Fabrication of 3D chitosan–hydroxyapatite scaffolds using a robotic dispensing system. Materials science and engineering: C, 2002. 20(1-2): p. 35-42.

[165] Munir, N., A. McDonald, and A. Callanan, A combinatorial approach: Cryo-printing and electrospinning hybrid scaffolds for cartilage tissue engineering. Bioprinting, 2019. 16: p. e00056.

[166] Li, J. and D.J. Mooney, Designing hydrogels for controlled drug delivery. Nature Reviews Materials, 2016. 1(12): p. 1-17.

[167] Esquivel-Castro, T.A., M. Ibarra-Alonso, J. Oliva, and A. Martínez-Luévanos, Porous aerogel and core/shell nanoparticles for controlled drug delivery: a review. Materials Science and Engineering: C, 2019. 96: p. 915-940.

[168] Biondi, M., F. Ungaro, F. Quaglia, and P.A. Netti, Controlled drug delivery in tissue engineering. Advanced drug delivery reviews, 2008. 60(2): p. 229-242.

[169] Babu, M., Collagen based dressings—a review. Burns, 2000. 26(1): p. 54-62.

[170] Kumar, S.S. and B. Pant, Design principles and considerations for the 'ideal'silicon piezoresistive pressure sensor: a focused review. Microsystem technologies, 2014. 20(7): p. 1213-1247.

[171] Zhai, T., L. Verdolotti, S. Kacilius, P. Cerruti, G. Gentile, H. Xia, M. Stanzione, G.G. Buonocore, and M. Lavorgna, High piezo-resistive performances of anisotropic composites realized by embedding rGO-based chitosan aerogels into open cell polyurethane foams. Nanoscale, 2019. 11(18): p. 8835-8844.

[172] Yang, C., W. Liu, N. Liu, J. Su, L. Li, L. Xiong, F. Long, Z. Zou, and Y. Gao, Graphene aerogel broken to fragments for a piezoresistive pressure sensor with a higher sensitivity. ACS applied materials & interfaces, 2019. 11(36): p. 33165-33172.

[173] Maleki, H., Recent advances in aerogels for environmental remediation applications: A review. Chemical Engineering Journal, 2016. 300: p. 98-118.

[174] Dai, J., Q. Tian, Q. Sun, W. Wei, J. Zhuang, M. Liu, Z. Cao, W. Xie, and M. Fan, TiO2-alginate composite aerogels as novel oil/water separation and wastewater remediation filters. Composites Part B: Engineering, 2019. 160: p. 480-487.

[175] Li, Y., T. Gao, Z. Yang, C. Chen, W. Luo, J. Song, E. Hitz, C. Jia, Y. Zhou, and B. Liu, 3D-printed, all-in-one evaporator for high-efficiency solar steam generation under 1 sun illumination. Advanced Materials, 2017. 29(26): p. 1700981.

[176] Riffat, S.B. and G. Qiu, A review of state-of-the-art aerogel applications in buildings. International Journal of Low-Carbon Technologies, 2013. 8(1): p. 1-6.

[177] Cuce, E., P.M. Cuce, C.J. Wood, and S.B. Riffat, Toward aerogel based thermal superinsulation in buildings: a comprehensive review. Renewable and Sustainable Energy Reviews, 2014. 34: p. 273-299.

[178] Hasan, M.A., R. Sangashetty, A. Esther, S.B. Patil, B.N. Sherikar, and A. Dey, Prospect of thermal insulation by silica aerogel: a brief review. Journal of The Institution of Engineers (India): Series D, 2017. 98(2): p. 297-304.

Chapter 3 - High Speed *In-situ* X-Ray Imaging of 3D Freeze Printing of Aerogels[2]

Aerogels are gels in which the liquid phase has been replaced by air without significant shrinkage and collapse in the microstructure.[1] They exhibit unique properties such as ultra-low density, high and tunable porosity, large surface area, low thermal conductivity, refractive index, and dielectric constant, which makes them suitable for many different applications.[2–5] Replacement of the liquid by air is achieved through several methods including supercritical fluid drying, solvent-replaced ambient drying, surface-modified ambient drying, freeze drying, and so on.[2] Among these, freeze drying is utilized by a freeze-casting method, which is a well-established process for fabricating aerogels from ceramics[6–10], metals[11–15], carbon-based materials[16–18], nanocomposites[19–22], etc. for many different applications such as energy storage and conversion[23–25], photo catalysis[26], liquid chromatography[27], sensors[28–30], and bioengineering[31,32]. Advantages of freeze casting include but are not limited to its simple procedure, environmental-friendly nature, and ability to tailor the microstructure of the final product.[33] In freeze casting, the precursor, which is composed of a liquid solvent and solute particles, is frozen inside a mold to provide the desired shape (Figure 3.1a). Then solidified solvent crystals are sublimated under low pressure and temperature conditions.[34–37] During freezing, the solute particles are rejected by growing crystals of solvent, which results in a tightly packed network of solute particles (Figure 3.1b). Once the solvent crystals are sublimated by freeze drying,

[2] Reprinted with permission from "High Speed *In-situ* X-ray Imaging of 3D Freeze Printing of Aerogels" by Halil Tetik, Guang Yang, Wenda Tan, Anthony Fong, Shuting Lei, Johanna Nelson Weker, and Dong Lin, 2020. Additive Manufacturing, 36, 101513. 2020 Elsevier B.V.

a porous structure whose morphology is a replica of the solvent crystals is obtained.[34] Growth of the solvent crystals can be oriented with an applied-temperature gradient as seen in unidirectional and bidirectional freeze casting.[38] Many factors can be used to tailor the microstructure of the freeze-casted aerogels such as size of the solute particles, solid loading of the precursor, type and concentration of the additives used, freezing rate, rheology of the liquid precursor, etc.[39–41] Even though freeze casting has many ways to manipulate the microstructure of the final product, the macrostructure relies heavily on the geometry of the mold used during the process.

Our group has recently developed a 3D freeze-printing (3DFP) process with our collaborators, which is a novel method of combining unidirectional freeze casting with DOD printing to eliminate the need for a mold and increase the customization capabilities of the freeze casting process.[42–45] With 3DFP, droplets of liquid precursors are generated using a DOD dispenser and are deposited on top of a substrate whose temperature is well below the freezing point of the solvent used in the liquid precursor (Figure 3.1c). As droplets have contact with the precooled substrate, the solvents experience an immediate freezing which allows them to preserve their shape. With the reduced distance and time between separate droplets, uniform lines can be obtained after the coalescence of droplets. Using these lines, complex 3D frozen structures can be achieved without using a mold. Frozen structures with desired shapes are freeze dried, which sublimates the solvent crystals, and a porous aerogel is obtained. Since 3DFP involves freeze casting, the micro-structure of the final aerogel can be manipulated by the freezing kinetics. As in the unidirectional freeze-casting process, solvent crystals grow from bottom to top along the temperature gradient (Figure 3.1b) and controlling the substrate temperature offers control of the average pore-size distribution. Additives that will not affect the printability of the precursor can be used for manipulating the solvent crystal morphology. Besides its ability to tailor the

microstructure of the final aerogel, 3DFP is also capable of fabricating true 3D structures with overhang features by using water as support material (Figure 3.1c). Deposited ink at room temperature ($N+1^{th}$ layer - Figure 3.1d) causes a partial melting on top of the previously deposited and frozen ink (N^{th} layer - Figure 3.1d). Since the ink's viscosity is low, it fills the possible voids that could occur between layers by the help of surface tension and gravitational forces. And finally, partially melted part of N^{th} layer fuses with the not yet frozen $N+1^{th}$ layer and they both freeze together. This eliminates insufficient bonding, interfacial boundaries, and voids between layers and yields aerogels with ultralow densities. To demonstrate the capabilities of the 3DFP process, we fabricated an aerogel with overhang feature as given in Figure 3.1e. More details can be found in our previous publication on 3D printing of graphene aerogels with overhang features.[45] Once 3DFP process is completed, supporting ice is completely sublimated with the following freeze drying process. The micrographs show the alignment of the pores along the freezing direction (from bottom to top) as well as the void-free interfacial boundaries, which two of the most important advantages of the 3DFP process.

Freeze-casting processes have widely been investigated *in-situ* using optical[46–49] and X-ray[50–53] imaging systems to identify unknown aspects of the process. However, X-ray imaging, which is one of the most informative methods to investigate the morphology of freeze casted structures[50], provides some advantages over optical imaging methods. These advantages include elimination of the requirement to use optically transparent materials, ability to observe inside of the material, eliminating the need for suspensions composed of single and large particles to provide clearer observations, and higher spatial resolution.[52–54] Therefore, X-ray imaging techniques have been used to investigate the process dynamics of several 3D printing processes including laser powder-bed fusion[55–59], powder-blown laser-additive manufacturing[60], and binder jetting

Figure 3.1. a) Schematics of the unidirectional freeze casting process. b) Growth of ice crystals along the temperature gradient in directional freezing process. c) Schematics of the 3DFP processes using water as support material to fabricate 3D structures with overhang features. d) Schematics illustrating the partial melting that already frozen ink (N^{th} layer) experiences after depositing liquid ink ($N+1^{th}$ layer) on top of it. e) 3DFP of a truly 3D structure from SiO_2-PVA ink using water as support material. f) SEM micrographs showing void-free interfacial boundary obtained by 3DFP process.

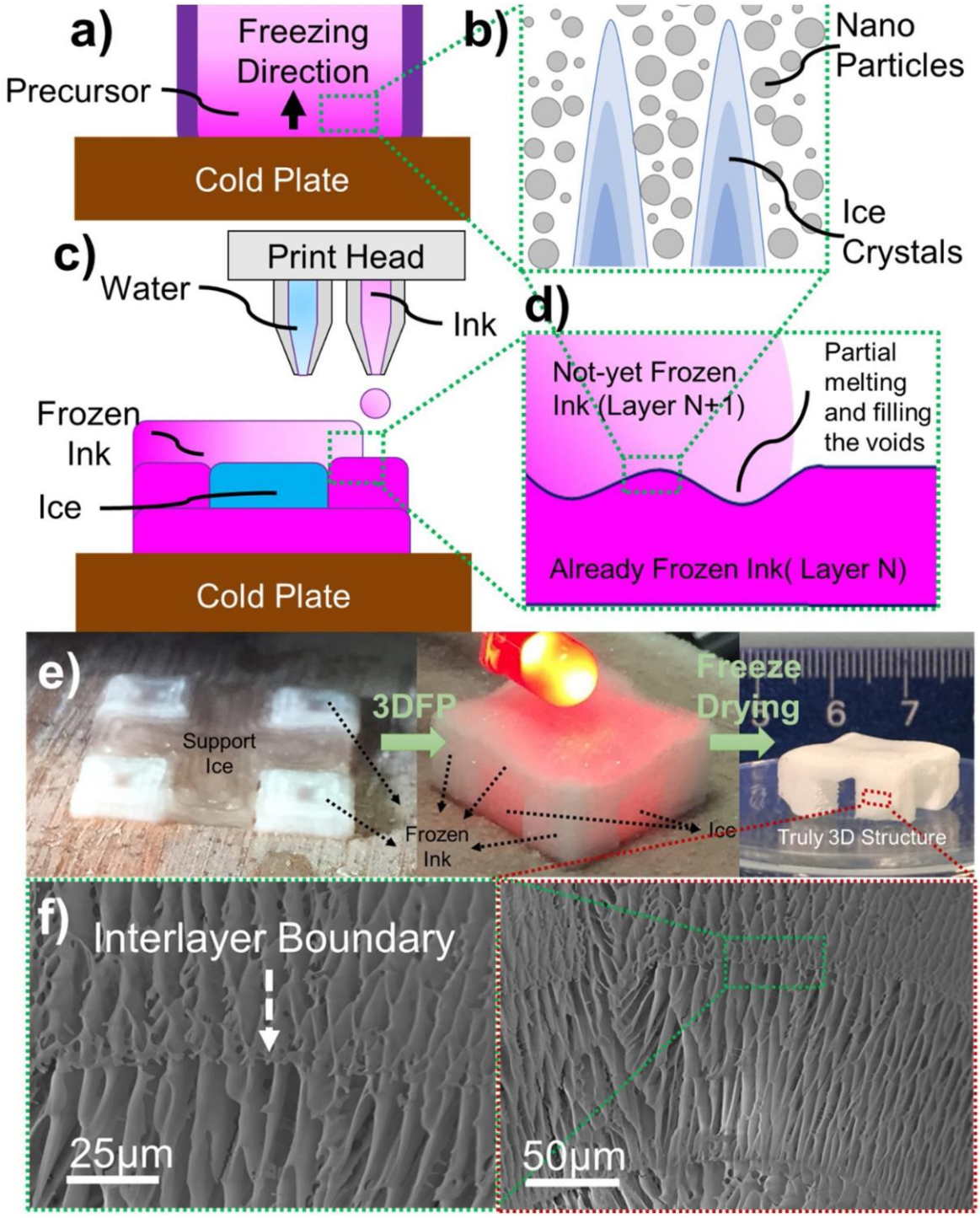

additive manufacturing[61]. Since 3DFP is a hybrid process in which DOD printing was followed by freeze drying and a subsequent heat treatment (when required), investigation of final products thereafter the complete process does not provide quality information regarding the "3DFP" part of the process, which plays a crucial role in the product quality. To understand the relation between substrate temperature, which controls the freezing rate of the deposited material, and deposition rate of the material, and the ice crystal growth mechanism along the interfacial boundaries, which ensures a good fusion of subsequent layers, we performed the *in-situ* investigation of the process using X-ray imaging techniques. Using the setup given in Figure 3.2 we performed *in-situ* X-ray imaging of separate droplets, lines obtained after coalescence of droplets and three consecutive lines deposited layer by layer. We showed that achieving uniform lines from separate droplets depends on a careful balance between material deposition and freezing (solidification) rates. With the advantages provided by the X-ray imaging techniques, we were able to observe freeze front, deposited material, and growing ice crystals simultaneously. To the best of our knowledge, this is the first study reporting an *in-situ* X-ray imaging experiment investigating material deposition and freezing processes simultaneously.

Experimental

Materials

For the *in-situ* X-ray imaging experiments, a 15 wt. % colloidal silica suspension with an average particle size of 4−6 nm (Nyacol, MA, USA) was used as ink. Schematics of the 3D freeze printing setup is given in Figure 3.2. Briefly, a three-axis motion stage (Panowin Technologies, Shanghai, China) was used to manipulate the DOD print-head, which was composed of a syringe barrel (Nordson EFD, RI, USA) and a solenoid micro dispenser (The Lee Co, CT, USA) loaded with a nozzle tip having a diameter of 190 μm. Solenoid micro dispensers operate through an

internal piston, which forces the valve to open and close via an induced magnetic field.[62] Once the piston is actuated and the valve is opened, pressurized ink moves to the orifice and is ejected as droplets.[63] An electrical pulse, whose length determines the opening time of the valve, is used to actuate the piston that allows or blocks ink flow.[64,65] A pneumatic fluid dispenser (Nordson EFD, RI, USA) was used to control the pressure inside the syringe barrel. Solenoid micro dispenser was used to generate fine droplets of colloidal silica ink with desired jetting frequencies. A liquid-nitrogen (L-N_2)-operated hot/cold plate (Instec, CO, USA) was used to control the temperature of the substrate.

Methods

In-situ investigation of the 3DFP process using white light synchrotron X-rays was performed at bending magnet beamline 2−2 of Stanford Synchrotron Radiation Lightsource, SLAC National Accelerator Laboratory in CA, USA. Using the setup given in Figure 3.2, the material was deposited along y axis for 10 mm, at a single x coordinate. By tuning the print-head speed and jetting frequency, we performed the material deposition as separate droplets, uniform lines obtained after coalescence of droplets, and three consecutive lines deposited layer by layer (Figure 3.2). The image of the deposited material, which was hit by the Xray, was recorded by a camera chip. By adjusting the DOD print-head speed and jetting frequency, we controlled the distance between the successive droplets and investigated the freezing process of separate droplets, as well as single layer uniform lines and three consecutive lines deposited layer by layer.

X-ray images were collected using a scintillator-based optical system with a 100 μm YAG:Ce scintillator crystal (Crytur Ltd.) coated in 120 nm of Al on the upstream side, high reflectance mirror (Thorlabs) to bend the visible light 90˚ off-axis to the X-rays into a 4x long working distance infinity corrected objective lens (Nikon), infinity-corrected tube lens (Thorlabs),

Figure 3.2. Schematics of the experimental setup used in the synchrotron radiation light source facility and deposited structures (separate droplets, uniform lines, and three consecutive lines deposited layer by layer) investigated in-situ.

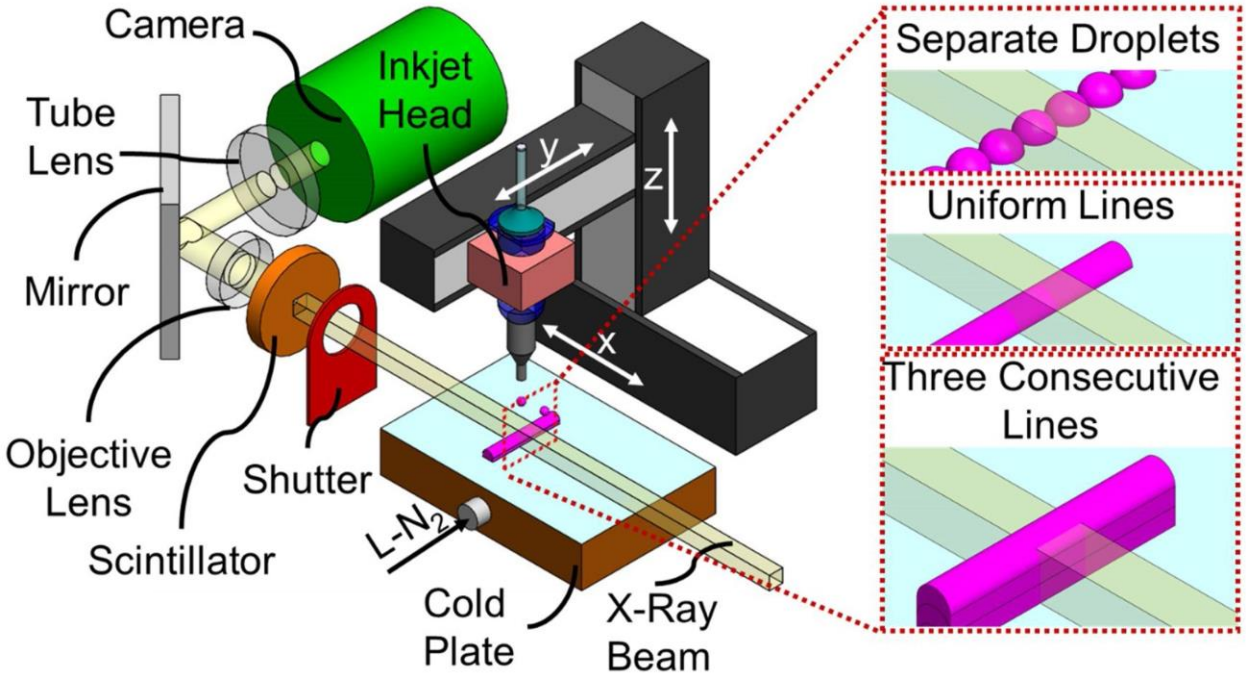

and high speed CMOS camera pco.dimax S4 (PCO). With these optical components, the effective pixel size is 2.4 μm for a field of view of 4.8 mm x 2.4 mm and images were captured at 500 Hz. The stroboscopic images showing the droplet-generation process were obtained using a CCD camera (Sentech) synchronized with an LED bulb.

Images showing the top view of deposited material (Figure 3.5) were obtained using an optical microscope (Olympus). Samples in these images were prepared by depositing the colloidal silica ink on top of a silicon wafer substrate at given temperatures. 3D freeze printed samples demonstrated in Figure 3.1e were fabricated after adding a weighted amount of PVA into the colloidal silica ink used in *in-situ* experiments since colloidal silica requires additional binding agents and further sintering after 3DFP to protect the structural integrity of the aerogels.[52] 3D freeze printed samples were treated by a subsequent freeze drying process for 48 h where the temperature was -35 ℃ and the pressure was 0.2 mbar.

Results and Discussion

3DFP employs a DOD printing system for several reasons. DOD printing generates droplets of low-concentration inks that yield aerogels with ultra-low densities. It can use water as a supporting material to fabricate true 3D structures with overhang structures. Ability of low viscosity inks to fill the voids under surface tension and gravity eliminates voids and insufficient bonding between subsequent layers unlike most of other traditional 3D printing methods.[45] The rheological requirements for printability of an ink are determined by Reynolds, Weber, and Ohnesorge numbers, which are dimensionless numbers related to the physical properties of the ink such as viscosity, surface tension, and density.[66–69] A solenoid micro dispenser was employed in this study due to its robustness and allowing more flexibility for the ink formulation and process.[70] After adjusting the pressure of the ink, opening time of the solenoid micro dispenser, and diameter of the nozzle tip, we generated satellite-free droplets from the colloidal silica ink as presented with the stroboscopic optical images given in Figure 3.3a. The stroboscopic images were taken by a CCD camera with a 30-fps frame rate and a strobed LED behind the droplets. To freeze the droplet images and capture different phases of the droplet-generation process, we used various delay times between the drop ejection and LED strobe. The diameter of the spherical droplets was measured as approximately $d_0 \cong 190$ μm, which is approximately equal to the diameter of the nozzle tip used for the experiments. The volume of the ejected droplets was calculated as approximately ~3.6 nL.

Van Dam and Clerc[71] proposed to model the deposited droplets as spherical caps, schematically explained in Figure 3.3b. This spherical cap has a height of h, bead width of w, polar angle of θ, and radius of r. Considering a volumetric conservation, the volume of the spherical droplet before the deposition should be equal to the volume of the spherical cap right after the deposition. Following the deposit of the generated droplet on the substrate, we measured

the dimensions of five adjacent droplets and calculated the average dimensions of the spherical cap as w = 380.78 μm, and h = 59.98 μm, where h is the height of the spherical cap after it had been deposited (before formation of the conical tip). Measured dimensions of the spherical cap correspond to an initial volume of $V = (\pi h/6)(3(w/2)^2 + h^2) = 3.59$ nL, which is consistent in terms of volumetric conservation.

However, Van Dam and Clerc's spherical cap model does not consider a phase change after the deposition. It has been shown that when droplets of water are deposited on a cold plate, a conical tip is formed as the freeze front reaches to the top of the droplet.[72–74] (as shown in Figure 3.3c). This transformation of the droplet shape is attributed to the thermal expansion that water experiences after freezing.[73] Since the colloidal silica suspension that we used for the experiments is water-based, we also observed a shape change and a volumetric expansion in the droplets after complete freezing. As seen in Figure 3.3d, at the instant a droplet was deposited on the substrate, it had a spherical cap shape. As the time passed and the droplet froze, it experienced a thermal expansion and a conical tip formed at the top (pointed with the red arrow in Figure 3.3d). Using the *in-situ* X-ray images we obtained, we measured the bead width (w) and height (h) of five different droplets along the freezing process. To reduce the noise in the raw images, we processed them and increased their contrasts so that the distinction between the droplets and their surroundings is clear (Figure 3.3d). Measurements were done using ImageJ software by defining a pixel to μm scale ratio (0.42 pixels μm^{-1}), manually drawing lines along the width/height of the droplets, and recoding the corresponding dimensions. We measured the dimensions of five consecutive droplets from the initial frame at which the droplet was deposited (t = 0 s) to the final frame at which the droplet reached to its maximum height value (t = 0.14 s). Average values of the dimensions for five different droplets are provided in Figure 3.3e. We observed the average

Figure 3.3. a) Stroboscopic optical images showing the phases of droplet formation process using colloidal silica ink without any satellite formation. b) Schematics of a single droplet (before and after impact) and formed line after coalescence of multiple droplets. c) Schematics of a single droplet after experiencing the thermal expansion leading to formation of a conical tip on top of the spherical cap shape. d) In-situ X-ray images showing growth of conical tip on top of the spherical cap shaped droplet after experiencing a thermal expansion. The scale bar is 100 μm. e) The change in the dimensions of a single droplet due to thermal expansion.

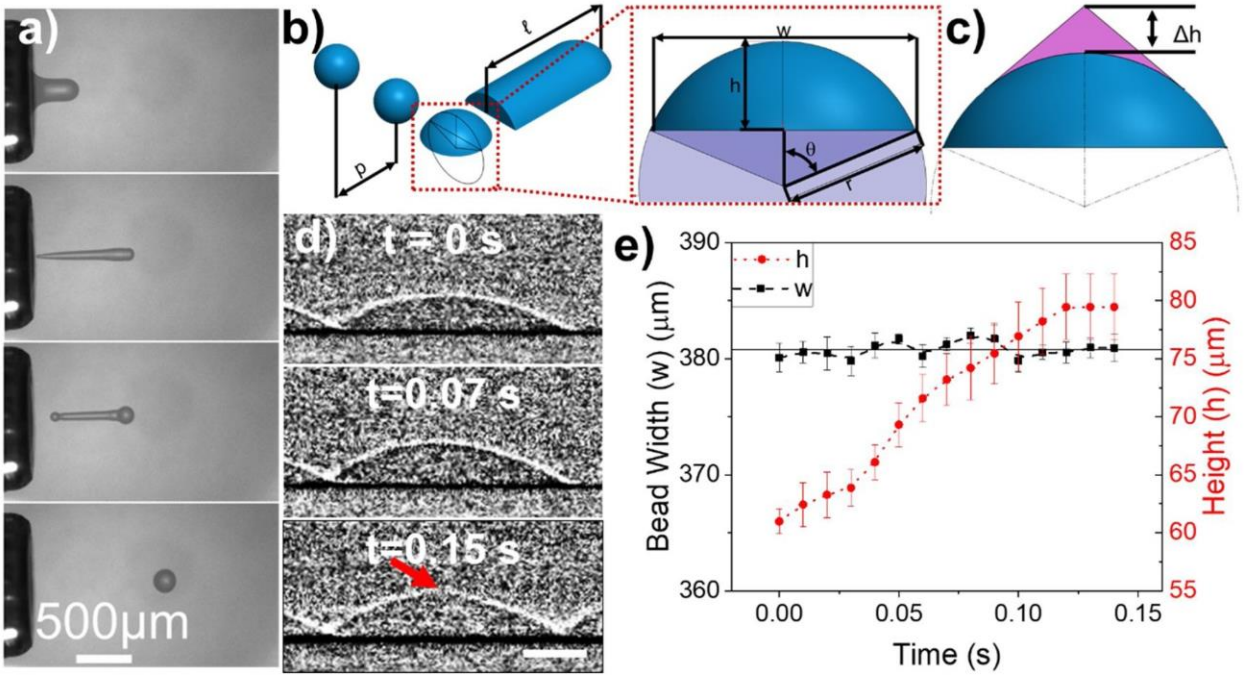

value of the bead width (w) value remained closed to an average value of 380.78 μm, while the average height of the droplets increased from 59.9 μm to 79.9 μm, which corresponds to an increase of Δh = 33.4 %. We used the amount of increase in the height of droplets after complete freezing to estimate the height of a line in the next subsection.

In order to achieve aerogels with complex 3D geometries, separate droplets need to coalesce so they can form a continuous line to build 3D geometries. Obtaining continuous lines depends on a well-adjusted balance between print-head speed (v), jetting frequency (f), and the diameter of the droplet before impact (d_0). The pitch distance between successive droplets is a function of the jetting frequency and print-head speed ($p = v/f$). The geometry of these continuous lines can be modelled as beads with a constant cross section of a circular segment as

proposed by Stringer and Derby.[75] Assuming a uniform line with a length of ℓ as given in Figure 3.3b, and considering volumetric conservation, total volume of the deposited droplets is equal to the volume of the line with constant cross section of a circular segment:

$$N\left(\frac{\pi}{6}d_0^3\right) = \left(r^2\theta - \frac{wr\cos\theta}{2}\right)\ell \qquad (3\text{-}1)$$

where N is the number of droplets required for the length of $\ell = pN$, $r = ((w/2)^2 + h^2)/2h$, and $\theta = \sin^{-1}(w/2r)$. The left-hand side of equation A-1 corresponds to the total volume of spherical droplets with the quantity of N. The right-hand side corresponds to the volume of a line having the cross-section of a spherical cap, which would be obtained without any phase change due to freezing. Equation 3-1 can be solved for h, with given d_0 and w, which will not include the thermal expansion in the calculation observed after freezing. To take it into account, we added a correction factor of c = 1.334, which corresponds to an average increase of 33.4 % in the height of single droplets after freezing. It was found by calculating the mean of measured increase in the height of five successive droplets. By multiplying the obtained height from equation A-1 with the correction factor, we were able to estimate the height of lines obtained after coalescence of droplets with different pitch distances. In order to validate this theory, we printed lines with different pitch distances (Figure 3.4a) and their height were measured (Figure 3.4b). The estimated values for the line heights with and without the correction factor were also provided in the plot, which shows that including the correction factor in the estimation of line heights provides a better agreement with the measured heights. This showed us that the geometrical model of Stringer and Derby for a line obtained after coalescence of droplets can be used to model the geometry of the 3D freeze printed lines after considering a correction factor due to the thermal expansion of water. Measurements of the line height with different pitch-distance values were performed using the X-ray images (Figure 3.4a), which were obtained using a print-head speed of v = 10 mm·s^{-1}.

Figure 3.4. a) Formation of lines after successive deposition of droplets with different pitch distances. The print head speed for all pitch distances is 10 mm s^{-1}. The scale bar is 250 µm. b) Comparison of calculated (with and without correction factor due to thermal expansion and shape change) and measured values of the layer heights as a function of pitch distance.

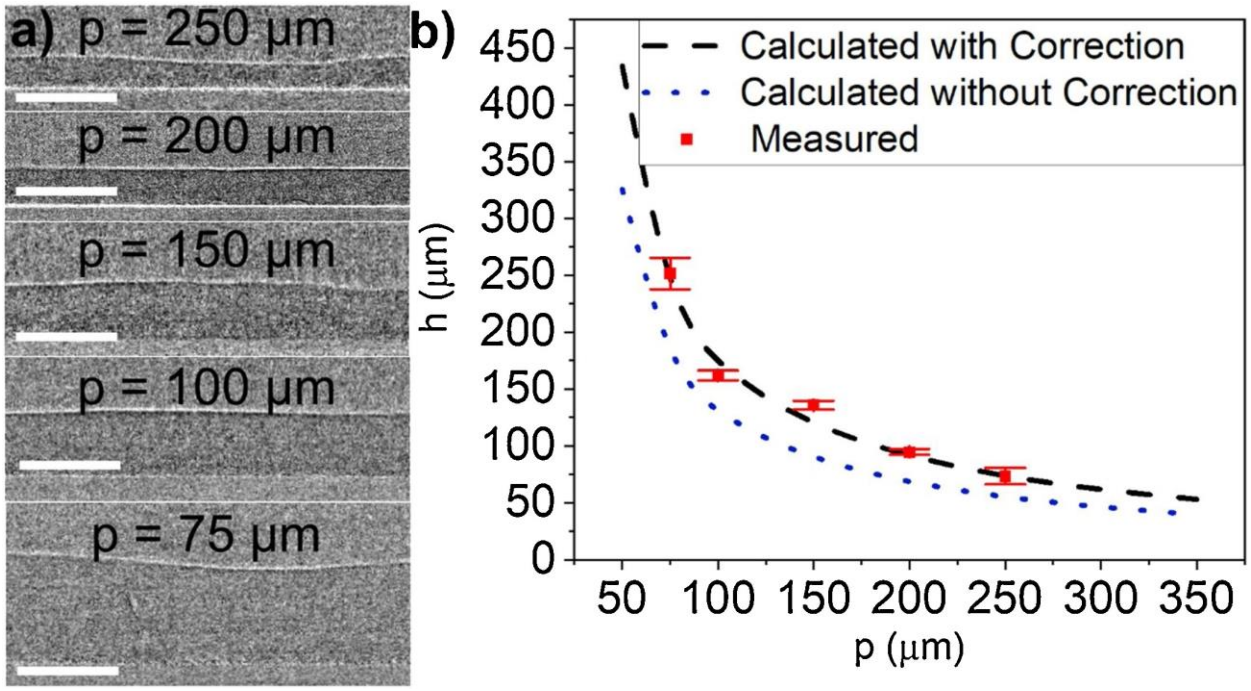

In the 3DFP process, uniformity of a line fabricated by coalescence of multiple droplets not only depends on the pitch distance, but also the time between two successive droplets (τ). Because droplets experience rapid solidification after impact, τ must be short enough to provide liquid-to-liquid interaction between adjacent droplets to achieve coalescence. Accordingly, Mingirulli *et al.*, previously showed that molten wax deposited by a DOD dispenser cannot achieve a smooth coalescence when τ is too high. Instead of continuous uniform lines, they observed each droplet separately solidified (frozen).[76] Furthermore, Sukhotskiy *et al.*, reported a simulation study for molten metal DOD printing, showing adjacent droplets cannot achieve a smooth coalescence as the time between the impact of successive droplets increases by reducing the jetting frequency, even though the inter-droplet pitch distance is kept the same.[77] To show the effects of different τ on the morphology of the printed lines, we fabricated lines with different print-head

Figure 3.5. Investigation of line-formation process using a constant pitch distance of 250 μm and a print head speed of a) 1 mm s^{-1} and b) 10 mm s^{-1}. Side view images were obtained using in-situ X-ray, and top view images were obtained using an optical microscope after freeze dying of the deposited lines. c) X-ray images obtained in-situ showing a good relationship between the freeze-front velocity and print head speed. The print head speed in this figure is 10 mm s^{-1} and the pitch distance is 75 μm. All scale bars are 250 μm.

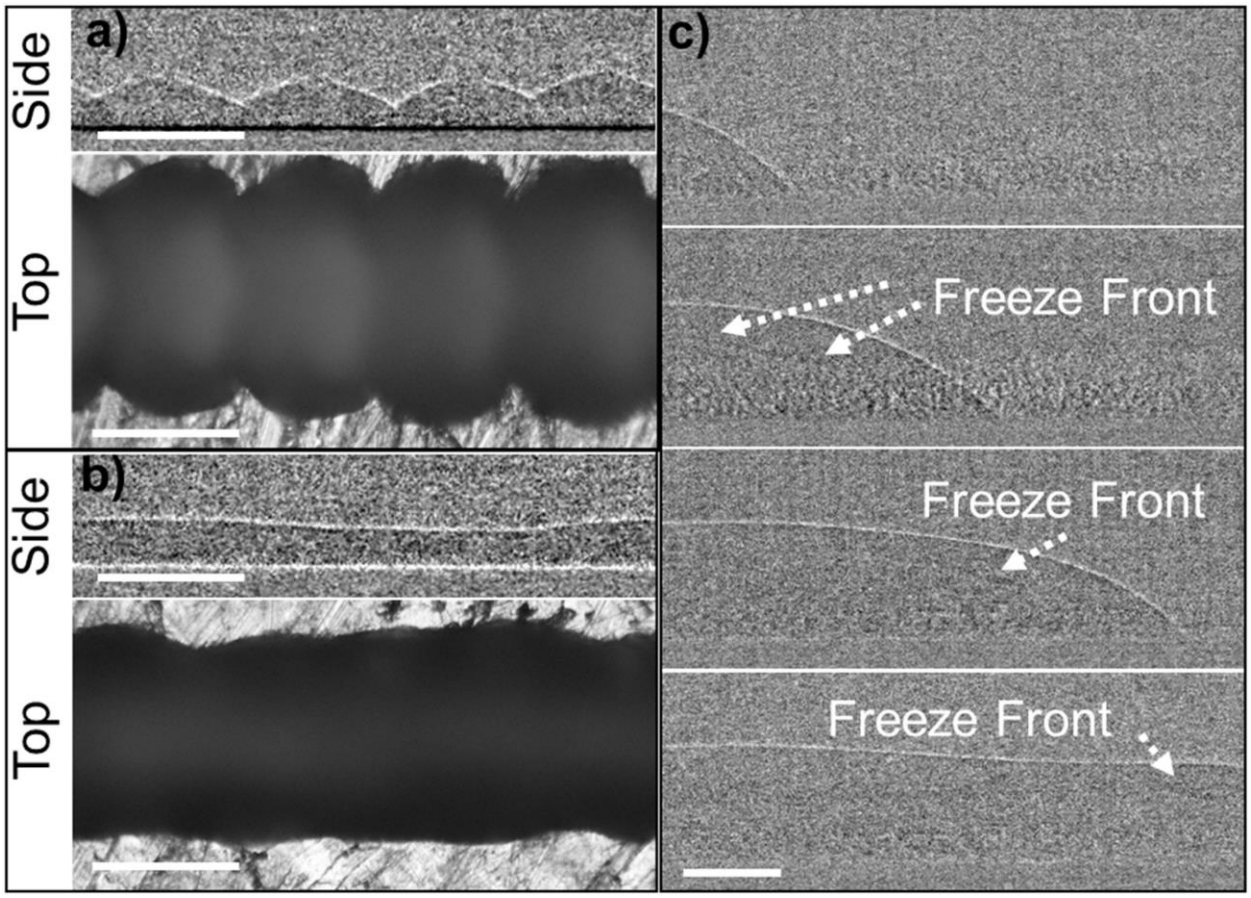

speeds (Figure 3.5). Figure 3.5a presents side- and top view images of the deposited droplets obtained by *in-situ* X-ray imaging and optical microscopy, respectively. In this figure, the print-head speed was v = 1 mm·s^{-1} and the jetting frequency was f = 4 Hz, which yields a pitch distance of p = 250 μm and an inter-droplet duration of τ = 250 ms. In this configuration the earlier droplet was fully solidified before the deposition of the adjacent droplet. However, when the printhead speed was increased to v = 10 mm·s^{-1}, using the same pitch distance (f = 40 Hz, p = 250 μm, and τ = 25 ms), time lapse was short enough for the droplets to achieve coalescence before the complete solidification of the previous droplet (Figure 3.5b). To better visualize the coalescence of separate

droplets under the effect of freezing, we decreased the pitch distance to p = 75 μm and observed the freezing. When time and distance between two successive droplets are appropriate, the freeze front is observed before the tip of the line printed and a uniform line is formed after coalescence of separate droplets (Figure 3.5c).

One of the main advantages of 3DFP is its ability to use low-viscosity inks which instantly fill the possible voids between layers observed in most of other 3D-printing techniques under surface tension and gravity such as extrusion-based 3D printing. Furthermore, when liquid suspension is deposited on top of a previously frozen layer, the not-yet-frozen material melts the already-frozen surface. These two materials (previously frozen and not-yet frozen) are mixed and refreeze together.[45] To understand the fusion of subsequent layers and ice crystal growing mechanism along the interfacial boundaries, we deposited three consecutive lines layer by layer and investigated the interfacial regions *in-situ* using X-ray (Figure 3.6). The print-head speed in these experiments was v = 10 mm·s^{-1}, the pitch distance was p = 100 μm. When the substrate temperature was set to T_{subs} = −30°C, the rate of freezing was fast enough for the deposited ink to preserve the shape, and slow enough to allow filling of voids for a sufficient interfacial bonding. There is no visible void or interfacial boundary exists between consecutive layers (Figure 3.6a). Furthermore, ice crystals that grew during the freezing were visible in the X-ray images. It was observed that those ice crystals penetrate from the second layer to the third layer without any formation of a visible boundary (Figure 3.6b). This penetration generates interconnected pores in the printed layers. This demonstrates that when the required conditions (e.g., substrate temperature, environment temperature, and relative humidity) are supplied, 3DFP is capable of eliminating the interfacial boundaries observed in most of the 3D printing techniques. When the substrate temperature was reduced to T_{subs} = −70 °C (Figure 3.6c), the rate of freezing increased

Figure 3.6. In-situ X-ray images showing three consecutive lines deposited layer by layer fabricated with a substrate temperature of −30℃. b) In-situ X-ray images showing growth of ice crystals along two consecutive layers when the substrate temperature was −30℃. c) Three consecutive lines deposited layer by layer fabricated with a substrate temperature of −70℃.

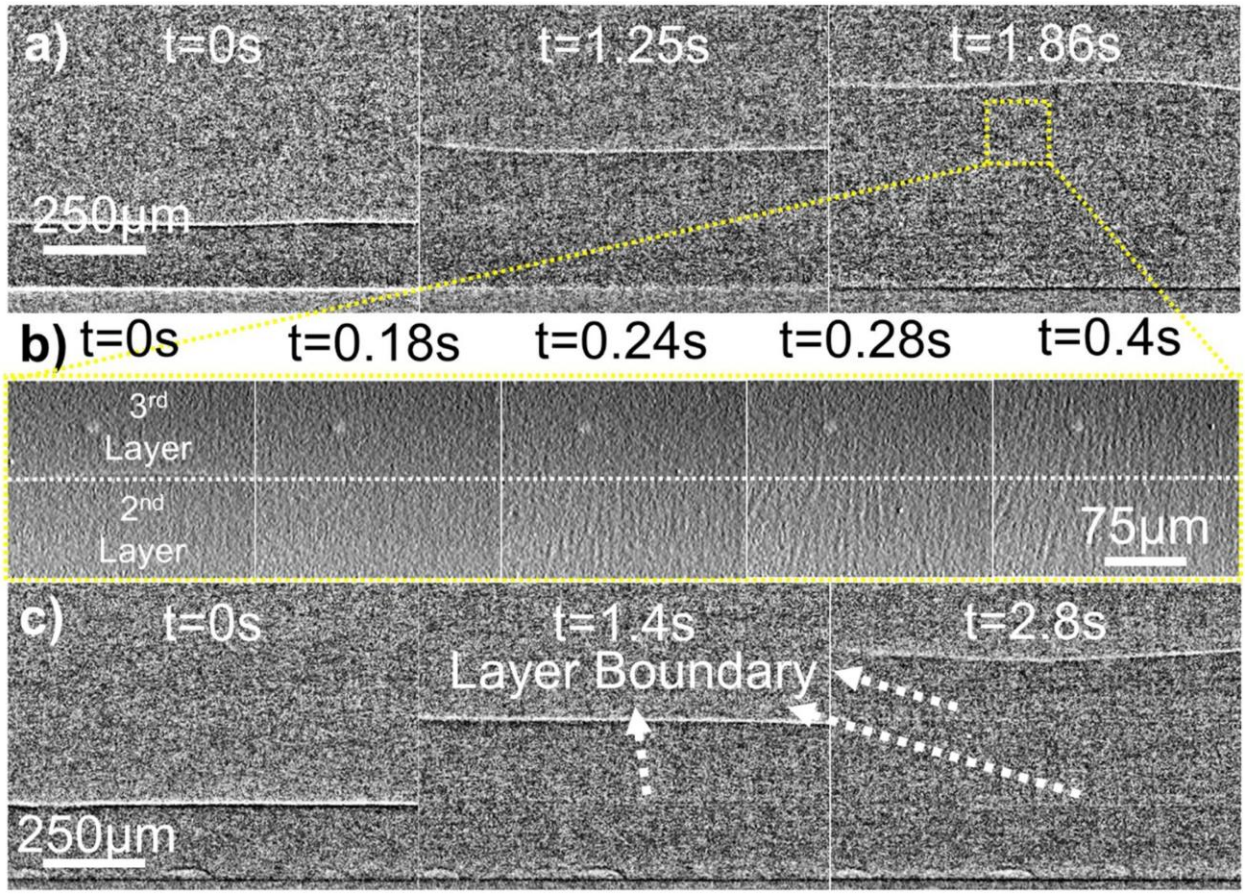

tremendously and the deposited ink did not have enough time to fill the voids before completely solidifying. This yielded to formation of interfacial boundaries between consecutive layers, which were possible to detect using *in-situ* X-ray images.

Conclusion

3DFP is a method used for fabricating customized aerogels for different applications including supercapacitor electrodes, sodium-ion battery anodes, electro-mechanical sensors, flexible electronics, etc. The ability of this printing method on eliminating voids and interfacial

boundaries between layers is exceptional when compared to most of other 3D-printing techniques. The other conclusions we have drawn from the experiments can be categorized as follows:

1. Dimensions of uniform lines formed after the coalescence of single droplets can be estimated from the droplet volume and measuring just one dimension of the spherical cap (after deposition). Also, since deposited droplets experience a phase change, thermal expansions/retractions should be considered for applying the conservation of volume in order to estimate the dimensions of the formed line.

2. Using the 3DFP process, the formation of uniform lines not only depends on the pitch distance between two successive droplets, but also the inter-droplet duration. If the former droplet totally freezes before the later droplet reaches the substrate, there is not enough time for coalescence. To ensure a maximum product quality, a well-adjusted balance between the material deposition and freezing rate must be achieved as confirmed by the *in-situ* observation of the freeze front following the tip of the printed line.

3. 3DFP provides an exceptional capability of fabricating aerogels without formation of voids and boundaries in between consecutive layers. This is achieved by partial melting of the already-frozen layer and employing low-viscosity inks, which fill the existing voids under surface tension and gravitational forces. *In-situ* experiments showed that ice crystals grow continuously along the interfacial boundaries without allowing any void or boundary formation between consecutive layers confirming the elimination of layer boundaries in 3DFP process.

References

[1] S.S. Kistler, Coherent expanded aerogels and jellies, Nature 127 (3211) (1931) p. 741-741.
[2] Du, B. Zhou, Z. Zhang, J. Shen, A special material or a new state of matter: a review and reconsideration of the aerogel, Materials 6 (3) (2013) 941–968.
[3] G. Gorgolis, C. Galiotis, Graphene aerogels: a review, 2D Mater. 4 (3) (2017) 032001.
[4] J. Stergar, U. Maver, Review of aerogel-based materials in biomedical applications, J. Solgel Sci. Technol. 77 (3) (2016) 738–752.

[5] T.A. Esquivel-Castro, M. Ibarra-Alonso, J. Oliva, A. Martínez-Luévanos, Porous aerogel and core/shell nanoparticles for controlled drug delivery: a review, Mater. Sci. Eng. C 96 (2019) 915–940.
[6] K. Araki, J.W. Halloran, New freeze-casting technique for ceramics with sublimable vehicles, J. Am. Ceram. Soc. 87 (10) (2004) 1859–1863.
[7] S.W. Sofie, F. Dogan, Freeze casting of aqueous alumina slurries with glycerol, J. Am. Ceram. Soc. 84 (7) (2001) 1459–1464.
[8] T. Waschkies, R. Oberacker, M.J. Hoffmann, Control of lamellae spacing during freeze casting of ceramics using double-side cooling as a novel processing route, J. Am. Ceram. Soc. 92 (2009) S79–S84.
[9] J. Han, C. Hong, X. Zhang, J. Du, W. Zhang, Highly porous ZrO2 ceramics fabricated by a camphene-based freeze-casting route: microstructure and properties, J. Eur. Ceram. Soc. 30 (1) (2010) 53–60.
[10] L. Hu, C.-A. Wang, Y. Huang, C. Sun, S. Lu, Z. Hu, Control of pore channel size during freeze casting of porous YSZ ceramics with unidirectionally aligned channels using different freezing temperatures, J. Eur. Ceram. Soc. 30 (16) (2010) 3389–3396.
[11] H.-D. Jung, S.-W. Yook, H.-E. Kim, Y.-H. Koh, Fabrication of titanium scaffolds with porosity and pore size gradients by sequential freeze casting, Mater. Lett. 17 (63) (2009) 1545–1547.
[12] G. Gouws, N. Shortt, Microstructured silver surfaces produced by freeze casting for enhanced phase change heat transfer, Journal of Physics: Conference Series, IOP Publishing, 2015.
[13] F. Qian, P.C. Lan, M.C. Freyman, W. Chen, T. Kou, T.Y. Olson, C. Zhu, M.A. Worsley, E.B. Duoss, C.M. Spadaccini, Ultralight conductive silver nanowire aerogels, Nano Lett. 17 (12) (2017) 7171–7176.
[14] Y. Tang, K.L. Yeo, Y. Chen, L.W. Yap, W. Xiong, W. Cheng, Ultralow-density copper nanowire aerogel monoliths with tunable mechanical and electrical properties, J. Mater. Chem. A 1 (23) (2013) 6723–6726.
[15] A.I. Ramos, D.C. Dunand, Preparation and characterization of directionally freezecast copper foams, Metals 2 (3) (2012) 265–273.
[16] C. Wang, X. Chen, B. Wang, M. Huang, B. Wang, Y. Jiang, R.S. Ruoff, Freeze-casting produces a graphene oxide aerogel with a radial and centrosymmetric structure, ACS Nano 12 (6) (2018) 5816–5825.
[17] W. Gao, N. Zhao, W. Yao, Z. Xu, H. Bai, C. Gao, Effect of flake size on the mechanical properties of graphene aerogels prepared by freeze casting, RSC Adv. 7 (53) (2017) 33600–33605.
[18] J. Bai, Y. Huang, Q. Gong, X. Liu, Y. Li, J. Gan, M. Zhao, Y. Shao, D. Zhuang, J. Liang, Preparation of porous carbon nanotube/carbon composite spheres and their adsorption properties, Carbon 137 (2018) 493–501.
[19] B. Wicklein, A. Kocjan, G. Salazar-Alvarez, F. Carosio, G. Camino, M. Antonietti, L. Bergström, Thermally insulating and fire-retardant lightweight anisotropic foams based on nanocellulose and graphene oxide, Nat. Nanotechnol. 10 (3) (2015) 277.
[20] P.K. Sahoo, N. Kumar, S. Thiyagarajan, D. Thakur, H.S. Panda, Freeze-Casting of multifunctional cellular 3D-graphene/Ag nanocomposites: synergistically affect supercapacitor, catalytic, and antibacterial properties, ACS Sustain. Chem. Eng. 6 (6) (2018) 7475–7487.

[21] S.M.H. Ghazanfari, A. Zamanian, Phase transformation, microstructural and mechanical properties of hydroxyapatite/alumina nanocomposite scaffolds produced by freeze casting, Ceram. Int. 39 (8) (2013) 9835–9844.
[22] W. Li, K. Lu, J.Y. Walz, Formation, Structure and Properties of Freeze-Cast Kaolinite–Silica Nanocomposites, J. Am. Ceram. Soc. 94 (4) (2011) 1256–1264.
[23] C.-C. Ji, M.-W. Xu, S.-J. Bao, C.-J. Cai, Z.-J. Lu, H. Chai, F. Yang, H. Wei, Selfassembly of three-dimensional interconnected graphene-based aerogels and its application in supercapacitors, J. Colloid Interface Sci. 407 (2013) 416–424.
[24] P. Zuo, W. Zhang, J. Hua, Y. Ma, C. Du, X. Cheng, Y. Gao, G. Yin, A novel onedimensional reduced graphene oxide/sulfur nanoscroll material and its application in lithium sulfur batteries, Electrochim. Acta 222 (2016) 1861–1869.
[25] C. Stolze, T. Janoschka, S. Flauder, F.A. Müller, M.D. Hager, U.S. Schubert, Investigation of ice-templated porous electrodes for application in organic batteries, ACS Appl. Mater. Interfaces 8 (36) (2016) 23614–23623.
[26] C. Suwanchawalit, A.J. Patil, R.K. Kumar, S. Wongnawa, S. Mann, Fabrication of ice-templated macroporous TiO 2–chitosan scaffolds for photocatalytic applications, J. Mater. Chem. 19 (44) (2009) 8478–8483.
[27] M. Barrow, A. Eltmimi, A. Ahmed, P. Myers, H. Zhang, Frozen polymerization for aligned porous structures with enhanced mechanical stability, conductivity, and as stationary phase for HPLC, J. Mater. Chem. 22 (23) (2012) 11615–11620.
[28] J. Kuang, L. Liu, Y. Gao, D. Zhou, Z. Chen, B. Han, Z. Zhang, A hierarchically structured graphene foam and its potential as a large-scale strain-gauge sensor, Nanoscale 5 (24) (2013) 12171–12177.
[29] C. Hou, H. Wang, Q. Zhang, Y. Li, M. Zhu, Highly conductive, flexible, and compressible all-graphene passive electronic skin for sensing human touch, Adv. Mater. 26 (29) (2014) 5018–5024.
[30] J. Kuang, Z. Dai, L. Liu, Z. Yang, M. Jin, Z. Zhang, Synergistic effects from graphene and carbon nanotubes endow ordered hierarchical structure foams with a combination of compressibility, super-elasticity and stability and potential application as pressure sensors, Nanoscale 7 (20) (2015) 9252–9260.
[31] J.J. Campbell, A. Husmann, R.D. Hume, C.J. Watson, R.E. Cameron, Development of three-dimensional collagen scaffolds with controlled architecture for cell migration studies using breast cancer cell lines, Biomaterials 114 (2017) 34–43.
[32] Y. Zhu, K. Song, S. Jiang, J. Chen, L. Tang, S. Li, J. Fan, Y. Wang, J. Zhao, T. Liu, Numerical simulation of mass transfer and three-dimensional fabrication of tissueengineered cartilages based on chitosan/gelatin hybrid hydrogel scaffold in a rotating bioreactor, Appl. Biochem. Biotechnol. 181 (1) (2017) 250–266.
[33] T. Fukasawa, M. Ando, T. Ohji, S. Kanzaki, Synthesis of porous ceramics with complex pore structure by freeze-dry processing, J. Am. Ceram. Soc. 84 (1) (2001) 230–232.
[34] S. Deville, Freeze-casting of porous ceramics: a review of current achievements and issues, Adv. Eng. Mater. 10 (3) (2008) 155–169.
[35] M. Naviroj, S. Miller, P. Colombo, K. Faber, Directionally aligned macroporous SiOC via freeze casting of preceramic polymers, J. Eur. Ceram. Soc. 35 (8) (2015) 2225–2232.
[36] Macchetta, I.G. Turner, C.R. Bowen, Fabrication of HA/TCP scaffolds with a graded and porous structure using a camphene-based freeze-casting method, Acta Biomater. 5 (4) (2009) 1319–1327.

[37] R. Dash, Y. Li, A.J. Ragauskas, Cellulose nanowhisker foams by freeze casting, Carbohydr. Polym. 88 (2) (2012) 789–792.
[38] K.L. Scotti, D.C. Dunand, Freeze casting–A review of processing, microstructure and properties via the open data repository, Freeze Cast. Net. Prog. Mater. Sci. 94 (2018) 243–305.
[39] M.M. Porter, R. Imperio, M. Wen, M.A. Meyers, J. McKittrick, Bioinspired scaffolds with varying pore architectures and mechanical properties, Adv. Funct. Mater. 24 (14) (2014) 1978–1987.
[40] L. Yan, J. Wu, L. Zhang, X. Liu, K. Zhou, B. Su, Pore structures and mechanical properties of porous titanium scaffolds by bidirectional freeze casting, Mater. Sci. Eng. C 75 (2017) 335–340.
[41] Y. Zhang, K. Zuo, Y.-P. Zeng, Effects of gelatin addition on the microstructure of freeze-cast porous hydroxyapatite ceramics, Ceram. Int. 35 (6) (2009) 2151–2154.
[42] E. Brown, P. Yan, H. Tekik, A. Elangovan, J. Wang, D. Lin, J. Li, 3D printing of hybrid MoS2-graphene aerogels as highly porous electrode materials for sodium ion battery anodes, Mater. Des. 170 (2019) 107689.
[43] C. Ma, R. Wang, H. Tetik, S. Gao, M. Wu, Z. Tang, D. Lin, D. Ding, W. Wu, Hybrid nanomanufacturing of mixed-dimensional manganese oxide/graphene aerogel macroporous hierarchy for ultralight efficient supercapacitor electrodes in selfpowered ubiquitous nanosystems, Nano Energy 66 (2019) 104124.
[44] P. Yan, E. Brown, Q. Su, J. Li, J. Wang, C. Xu, C. Zhou, D. Lin, 3D printing hierarchical silver nanowire aerogel with highly compressive resilience and tensile elongation through tunable poisson's ratio, Small 13 (38) (2017) 1701756.
[45] Q. Zhang, F. Zhang, S.P. Medarametla, H. Li, C. Zhou, D. Lin, 3D printing of graphene aerogels, Small 12 (13) (2016) 1702–1708.
[46] J. Sekhar, R. Trivedi, Solidification microstructure evolution in the presence of inert particles, Mater. Sci. Eng. A 147 (1) (1991) 9–21.
[47] S.S. Peppin, M.G. Worster, J. Wettlaufer, Morphological instability in freezing colloidal suspensions, Proc. Royal Soc. A: Mathe. Phy. Eng. Sci. 463 (2079) (2007) 723–733.
[48] S. Peppin, J. Elliott, M.G. Worster, Solidification of colloidal suspensions, J. Fluid Mech. 554 (2006) 147–166.
[49] T. Waschkies, R. Oberacker, M. Hoffmann, Investigation of structure formation during freeze-casting from very slow to very fast solidification velocities, Acta Mater. 59 (13) (2011) 5135–5145.
[50] B. Delattre, H. Bai, R.O. Ritchie, J. De Coninck, A.P. Tomsia, Unidirectional freezing of ceramic suspensions: in situ X-ray investigation of the effects of additives, ACS Appl. Mater. Interfaces 6 (1) (2014) 159–166.
[51] S. Deville, J. Adrien, E. Maire, M. Scheel, M. Di Michiel, Time-lapse, three-dimensional in situ imaging of ice crystal growth in a colloidal silica suspension, Acta Mater. 61 (6) (2013) 2077–2086.
[52] S. Deville, E. Maire, A. Lasalle, A. Bogner, C. Gauthier, J. Leloup, C. Guizard, In situ X-ray radiography and tomography observations of the solidification of aqueous alumina particle suspensions—part i: initial instants, J. Am. Ceram. Soc. 92 (11) (2009) 2489–2496.
[53] S. Deville, E. Maire, A. Lasalle, A. Bogner, C. Gauthier, J. Leloup, C. Guizard, In situ X-Ray radiography and tomography observations of the solidification of aqueous alumina particles suspensions. Part II: Steady State, J. Am. Ceramic Soc. 92 (11) (2009) 2497–2503.

[54] S. Deville, E. Maire, G. Bernard-Granger, A. Lasalle, A. Bogner, C. Gauthier, J. Leloup, C. Guizard, Metastable and unstable cellular solidification of colloidal suspensions, Nat. Mater. 8 (12) (2009) 966–972.
[55] N.P. Calta, J. Wang, A.M. Kiss, A.A. Martin, P.J. Depond, G.M. Guss, V. Thampy, A.Y. Fong, J.N. Weker, K.H. Stone, An instrument for in situ time-resolved X-ray imaging and diffraction of laser powder bed fusion additive manufacturing processes, Rev. Sci. Instrum. 89 (5) (2018) 055101.
[56] A.A. Martin, N.P. Calta, S.A. Khairallah, J. Wang, P.J. Depond, A.Y. Fong, V. Thampy, G.M. Guss, A.M. Kiss, K.H. Stone, Dynamics of pore formation during laser powder bed fusion additive manufacturing, Nat. Commun. 10 (1) (2019) 1–10.
[57] Q. Guo, C. Zhao, M. Qu, L. Xiong, S.M.H. Hojjatzadeh, L.I. Escano, N.D. Parab, K. Fezzaa, T. Sun, L. Chen, In-situ full-field mapping of melt flow dynamics in laser metal additive manufacturing, Addit. Manuf. 31 (2020) 100939.
[58] C. Zhao, K. Fezzaa, R.W. Cunningham, H. Wen, F. De Carlo, L. Chen, A.D. Rollett, T. Sun, Real-time monitoring of laser powder bed fusion process using high-speed Xray imaging and diffraction, Sci. Rep. 7 (1) (2017) 1–11.
[59] N.D. Parab, C. Zhao, R. Cunningham, L.I. Escano, K. Fezzaa, W. Everhart, A.D. Rollett, L. Chen, T. Sun, Ultrafast X-ray imaging of laser–metal additive manufacturing processes, J. Synchrotron Radiat. 25 (5) (2018) 1467–1477.
[60] S.J. Wolff, H. Wu, N. Parab, C. Zhao, K.F. Ehmann, T. Sun, J. Cao, In-situ high-speed X-ray imaging of piezo-driven directed energy deposition additive manufacturing, Sci. Rep. 9 (1) (2019) 1–14.
[61] N.D. Parab, J.E. Barnes, C. Zhao, R.W. Cunningham, K. Fezzaa, A.D. Rollett, T. Sun, Real time observation of binder jetting printing process using high-speed X-ray imaging, Sci. Rep. 9 (1) (2019) 1–10.
[62] J. Sun, J. Ng, J. Fuh, Y. Wong, E. Thian, R. Yang, K.K. Tan, Fabrication of electronics devices with multi-material drop-on-demand dispensing system, 2010 International Conference on Manufacturing Automation, IEEE, 2010.
[63] D. Rose, Microdispensing technologies in drug discovery, Drug Discov. Today 4 (9) (1999) 411–419.
[64] C. Wang, R.I. Tomov, R.V. Kumar, B.A. Glowacki, Inkjet printing of gadoliniumdoped ceria electrolyte on NiO-YSZ substrates for solid oxide fuel cell applications, J. Mater. Sci. 46 (21) (2011) 6889–6896.
[65] C. Wang, S.C. Hopkins, R.I. Tomov, R.V. Kumar, B.A. Glowacki, Optimisation of CGO suspensions for inkjet-printed SOFC electrolytes, J. Eur. Ceram. Soc. 32 (10) (2012) 2317–2324.
[66] L. Nayak, S. Mohanty, S.K. Nayak, A. Ramadoss, A review on inkjet printing of nanoparticle inks for flexible electronics, J. Mater. Chem. C 7 (29) (2019) 8771–8795.
[67] B. Derby, Inkjet printing ceramics: from drops to solid, J. Eur. Ceram. Soc. 31 (14) (2011) 2543–2550.
[68] G. Cummins, M.P. Desmulliez, Inkjet printing of conductive materials: a review, Circuit World (2012).
[69] B. Derby, Inkjet printing of functional and structural materials: fluid property requirements, feature stability, and resolution, Annu. Rev. Mater. Res. 40 (2010) 395–414.

[70] G. Kollamaram, S.C. Hopkins, B.A. Glowacki, D.M. Croker, G.M. Walker, Inkjet printing of paracetamol and indomethacin using electromagnetic technology: rheological compatibility and polymorphic selectivity, Eur. J. Pharm. Sci. 115 (2018) 248–257.
[71] D.B. van Dam, C. Le Clerc, Experimental study of the impact of an ink-jet printed droplet on a solid substrate, Phys. Fluids 16 (9) (2004) 3403–3414.
[72] O.R. Enríquez, Á.G. Marín, K.G. Winkels, J.H. Snoeijer, Freezing singularities in water drops, Phys. Fluids 24 (9) (2012) 091102.
[73] A.G. Marin, O.R. Enriquez, P. Brunet, P. Colinet, J.H. Snoeijer, Universality of tip singularity formation in freezing water drops, Phys. Rev. Lett. 113 (5) (2014) 054301.
[74] J.H. Snoeijer, P. Brunet, Pointy ice-drops: how water freezes into a singular shape, Am. J. Phys. 80 (9) (2012) 764–771.
[75] J. Stringer, B. Derby, Formation and stability of lines produced by inkjet printing, Langmuir 26 (12) (2010) 10365–10372.
[76] N. Mingirulli, R. Keding, J. Specht, A. Fallisch, D. Stüwe, D. Biro, Hot-melt inkjet as masking technology for back-contacted cells, 2009 34th IEEE Photovoltaic Specialists Conference (PVSC), IEEE, 2009.
[77] V. Sukhotskiy, I. Karampelas, G. Garg, A. Verma, M. Tong, S. Vader, Z. Vader, E. Furlani, Magnetohydrodynamic drop-on-demand liquid metal 3D printing, Solid Freeform Fabr. Symp. Proc. (2017)

Chapter 4 - 3D Freeze Printing of Cellulose Nanocrystal Aerogels[3]

Reducing amount of oil resources and environmental pollution problems caused by synthetic petroleum-based polymers have lead the researchers, governments, and corporations to focus their interest on bio-degradable, cheap, and natural polymers.[1] Cellulose is the most abundant natural polymer existing on earth. It is estimated that more than 10^{11} metric tons of cellulose is synthesized in each year.[2] This almost inexhaustible polymer has been used as energy source, building block, raw material for clothing, and communication (in form of paper since ancient Egypt civilization). Cellulose is a polydisperse, linear syndiotactic natural polymer composed by the linkage of D-glucose with 1,4-β-glycosidic bonds.[3] Due to the biocompatibility, biodegradability, low-cost, tunable surface chemistry, thermal, and chemical stability of cellulose, it is still the main raw material for pulp and paper, lumber, and textile industries.[2] However, the needs of the modern society such as high performance, sustainable, renewable, functional, durable materials cannot be achieved using traditional cellulosic materials.[4,5] Fortunately, the nanoparticles derived from cellulose can respond to the society's needs and provide a new "building block" for the next generation materials.[4] Cellulose nanoparticles are highly ordered bundles of cellulose chains aligned in the bundle axis. This gives the material new properties such as high aspect ratio, better mechanical properties, lower thermal expansion, and lower density when compared to bulk cellulose.[5] Due to their superior material properties, nanomaterials derived from cellulose have been used in applications such as spanning the coatings, biomedical,

[3] Reprinted with permission from "3D freeze-printed cellulose-based aerogels: Obtaining truly 3D shapes, and functionalization with cross-linking and conductive additives" by Halil Tetik, Keren Zhao, Nasrullah Shah, and Dong Lin, 2021. Journal of Manufacturing Processes, 68, 445-453. 2021 The Society of Manufacturing Engineers

energy, construction, separations, and special chemical industries.[6] There is also a great research interest in aerogels based on cellulosic nanomaterials. Ultralow density, tunable porous architecture and outstanding mechanical properties of aerogels attract interest for a wide range of applications including e.g. biomedical scaffolds, thermal insulation and devices for storage and generation of energy.[7]

Aerogel, some call a special kind of material, some a new state of matter, is formed when the liquid component of a wet gel is replaced by air without any damage in the solid microstructure.[8] If the drying of wet gel is done as a transformation of the solvent from the liquid phase to gas phase (as in conventional drying), due to the surface tension in the liquid phase, the solid structures tend to be broken apart and pore structures will collapse. To achieve a damage-free drying, there are two common approaches. The first one is called as super-critical drying, in which the surface tension is eliminated by supplying the super-critical conditions where the liquid and gas phases are indistinguishable. The second approach is called freeze drying, and in this method the solvent is first transformed into solid phase by low temperature and following that, it is sublimated without any surface tension.[9] Even though aerogels have fixed volume and shapes, they can exhibit very low density (even lower than air), high porosity, and large specific surface area.[1] Aerogels made from cellulose nanoparticles with unique properties such as ultra-low thermal conductivity, modulus, sonic velocity, refractive index, dielectric constant, high specific surface area, and adjustable density have been proposed for biomedical and pharmaceutical applications, electrical devices and energy storage systems, thermal insulators and fire retarders, and many more.[7]

Freeze casting technique, which incorporates freeze drying in the process, have been utilized for fabrication of light-weight, and porous aerogels for many different applications[10–13]

due to its simple procedure, environmental friendly nature, and ability to have a good control on the micro structure of the final product.[14] This versatile, and easily implemented method involves solidification of a liquid suspension (via freezing) followed by the sublimation of the solvent using low pressure and temperature (freeze drying).[11] During the solidification, solid particles in the suspension are rejected by the solidifying solvent and packed together between growing solvent crystals.[15] With the sublimation of the solvent, solid particles form thin walls and the porosity is achieved as a replica of solvent crystals.[15] During the solidification, with the application of a temperature gradient, the solidification becomes an anisotropic process so that the solid crystals of the solvent are aligned along the direction of the temperature gradient.[16] Applying a control on the cooling rate during the solidification the average pore size distribution can be manipulated.[11] Furthermore, by using additives inside the suspension, the morphology of the solid crystals, as well as the pores after the solidification, can be manipulated.[17] Nanoparticles derived from cellulose, namely cellulose nanofibers (CNFs) and cellulose nanocrystals (CNCs), have been commonly used in the aerogels fabricated through freeze casting method.[11,18–21] Also, there are plenty of studies reporting freeze-casted composite aerogels based on cellulose nanoparticles proposed for different applications such as packaging[10], microwave absorption[22], electromagnetic interference shielding[23], oil absorbance[24], wearable sensors[25] and so on.

Even though freeze casting provides a variety of tools for tailoring the microstructure of the aerogels as desired, the macrostructure relies heavily on the geometry of the mold used during the process. To eliminate the dependency on molds, several research groups proposed to combine additive manufacturing with freeze casting process to fabricate cellulose-based aerogels with complex geometries. Additive manufacturing is a process constructing the final product by depositing material in layers such that it has a predesigned shape.[26] Accordingly, Li *et al.*

fabricated 3D printed CNC aerogels using direct ink writing (DIW) method.[27] In this method, a CNC-based ink with shear- thinning behavior is synthesized and extruded through a microneedle by applied pressure. Due to its rheology, the deposited ink can resist the gravitational forces and keep its structural integrity as well as its bead shape. Once the complete structure is formed after the deposition of the ink layer by layer, the 3D printed aerogels are obtained by a subsequent freeze-drying process. Similar processes are used for fabricating 3D printed cellulose-based aerogels by other researchers as well.[28,29] Kam *et al.*, proposed to use a cold plate as substrate so that a rapid fixation of the ink is achieved as well as an aligned microstructure along the freezing direction.[30] Cellulose-based aerogels fabricated by DIW-based 3D printing method were proposed for oil-water separation[28], biomedical[27] and triboelectric nanogenerator[31] applications. However, fabricating aerogels having truly 3D structures with overhang features has always been a great challenge. This limits the freedom and complexity in design as well as the potential applications of the 3D printed cellulose-based aerogels.

Here in, for the first time, we are reporting 3D printed CNC aerogels having truly 3D structures with overhang features. For this, we used our previously reported method, which is called 3D freeze printing (3DFP).[32–35] Since it is a drop-on-demand (DOD) based 3D printing method, we used pure water as support material and were able to fabricate truly 3D structures. To demonstrate our unique capability, we have fabricated a hollow egg-shell shaped aerogel with overhang features. We further characterized the microstructure and mechanical properties of the 3D printed CNC aerogels. To show the potential of the 3D freeze printed aerogels in biomedical applications, by using a wet strength additive commonly used in the paper industry, we cross-linked the CNC aerogels to protect the structural integrity of the aerogels when immersed in water. We also functionalized the fabricated 3D printed aerogels with a conductive polymer, namely poly

(3,4-ethylenedioxythiophene): poly (styrene sulfonate) (PEDOT:PSS) for potential applications in strain sensors and flexible electronics.

Experimental

Materials

CNC powder was purchased from Celluforce (Quebec, Canada). For the synthesis of aqueous CNC ink, we mixed CNC powder with DI water to achieve 2 wt. % concentration using a mechanical stirring process. For the cross-linking of the CNC aerogels, we purchased the wet strength additive (polyamide-epichlorohydrin (PAE) resin – Kymene) from Solenis (DE, USA). 2 wt. % aqueous CNC ink was mixed with a weighted amount of Kymene resin (the weight ratio of dry CNC to PAE is 5:1) by a mechanical stirring process. PEDOT:PSS (Clevios PH1000) was purchased from Heraeus (GA, USA). Aqueous CNC-based inks functionalized with the conductive polymer was prepared by mechanically mixing the weighted amount of PEDOT:PSS suspension (the weight ratio of 2 wt.% CNC ink to PEDOT:PSS suspension is 1:1) with the CNC-based ink.

3D Freeze Printing

The details of our 3D printing setup were provided in our previous reports.[36,37] Briefly, a three-axis motion stage (Panowin Technologies, Shanghai, China) was used to manipulate the DOD print-head, which was composed of a syringe barrel (Nordson EFD, RI, USA) and a solenoid micro dispenser (The Lee Co, CT, USA) loaded with a nozzle tip having a diameter of 130 μm. Desired inks were loaded inside the syringe barrel and the pressure was controlled using a pneumatic fluid dispenser (Nordson EFD, RI, USA). Droplets of the inks were generated by the inkjet dispenser were deposited on to the substrate whose temperature was controlled by a liquid nitrogen (L N2) operated hot/cold plate (Instec, CO, USA). Frozen constructs obtained from the 2 wt. % aqueous CNC ink were freeze-dried at 35°C and 0.2 mbar for 48 h to achieve CNC aerogels

by using a commercial benchtop freeze dryer (Labconco, MO, USA). Cross-linked CNC aerogels were obtained by a thermal treatment at 120°C for 3 h following the freeze-drying process.

Characterization

Scanning electron microscopy (SEM) (HELIOS Nanolab 600i, FEI) was used for characterizing the microstructure of the fabricated aerogels. A digital material testing device (Shimadzu Universal Testing Machine) was used for performing the compression tests. For compression tests, cubic samples with a unit dimension of 7.5 mm were 3D printed and compressed between two parallel plates with a constant compression rate of 1 mm min^{-1}. Electrical resistance and piezoresistance effect were measured by a two-probe method using a digital multimeter (Fluke 233) by sampling interval of 2 Hz.

Results and Discussion

The cellulose-based aqueous ink that was used for 3DFP of CNC aerogels was prepared by a mechanically mixing CNC powder with DI water. Since the rheological properties of the prepared ink is vital for the printability using DOD print head, the density, surface tension as well as the viscosity of the ink must be well adjusted.[38] The rheological requirements for printability of an ink are determined by Reynolds (Re), Weber (We), and Ohnesorge (Oh) numbers, which are dimensionless numbers related to the physical properties of the ink such as viscosity (η), surface tension (γ), and density (ρ)[38–41]:

$$Re = \frac{\upsilon \rho L}{\eta} \quad We = \frac{\upsilon^2 \rho L}{\gamma} \quad Oh = \frac{\sqrt{We}}{Re} = \frac{\eta}{\sqrt{\gamma \rho L}} \tag{4-1}$$

where υ is droplet velocity and L is nozzle diameter. For a stable drop formation, the range of $Z = 1 / Oh$ should be $1 < Z < 10$ to avoid large number of satellite droplet formation when Z > 10 or total dissipation of jetting energy required for droplet generation when $Z < 1$.[42] By measuring the weight of the 2 wt. % CNC-based aqueous ink with a known volume, we calculated its density

as 1130.54 kg m^{-3}. The viscosity of the ink is measured as 25.65 cP by using a Brookfield DVE digital viscometer loaded with an enhanced UL adapter. The surface tension of the ink is measured as 22 mN m^{-1} by using Pendent Drop plugin[43] for ImageJ software. The rheological properties of the ink along with a nozzle diameter of $L = 130$ μm, yielded to an Oh number of ~0.45, which corresponds to $1 < Z = 1/Oh \cong 2.22 < 10$. As a result of the appropriate rheology of the ink, we were able to generate satellite-free droplets for the maximum resolution in our 3D printing process as shown in our previous reports.[36,37] Once a printable ink is synthesized, it is dispensed in the form of droplets on to a freezing substrate whose temperature is well below the freezing point of the solvent (water in this study) used in the ink (Figure 4.1a). Once the droplets reach the substrate, they immediately solidify (freeze) and keep their shapes. By reducing the distance and time lapse between successive droplets, we achieve uniform lines, which are used to create 3D complex shapes. More detailed information regarding the formation of uniform lines after coalescence of separate droplets can be found in our previous report.[37] After obtaining the frozen structure with the desired shape, the ice content is sublimated with the application of low pressure and temperature (freeze drying) without any visible shrinkage or dimensional change. As a result of the freeze-drying process, we obtained highly porous and ultralight aerogels with an average density of 12.3 mg cm^{-3} as presented in Figure 4.1b-c. During the 3DFP process, micro-structure of the final product is manipulated by the freezing kinetics as in unidirectional freeze casting. The droplets reaching on the pre-cooled substrate experience an ice crystal formation along the temperature gradient. While ice crystals grow from bottom to top, the nanoparticles inside the ink are pushed and squeezed between the ice crystal blocks. After the freeze drying applied in the post-process phase, these ice blocks are sublimated, and the micro-pores are formed. Due to the anisotropy of the solidification, the microstructure also shows anisotropic morphology as in

Figure 4.1. a) Schematics of the 3D freeze printing process. b) Photographs of the 3D freeze printed cellulose aerogels. c) 3D freeze printed cellulose aerogel with a honeycomb shape standing on a dandelion. d) SEM image showing the top surface of the 3D freeze printed CNC aerogel. e) SEM image showing the cross-sectional surface of the 3D freeze printed CNC aerogel.

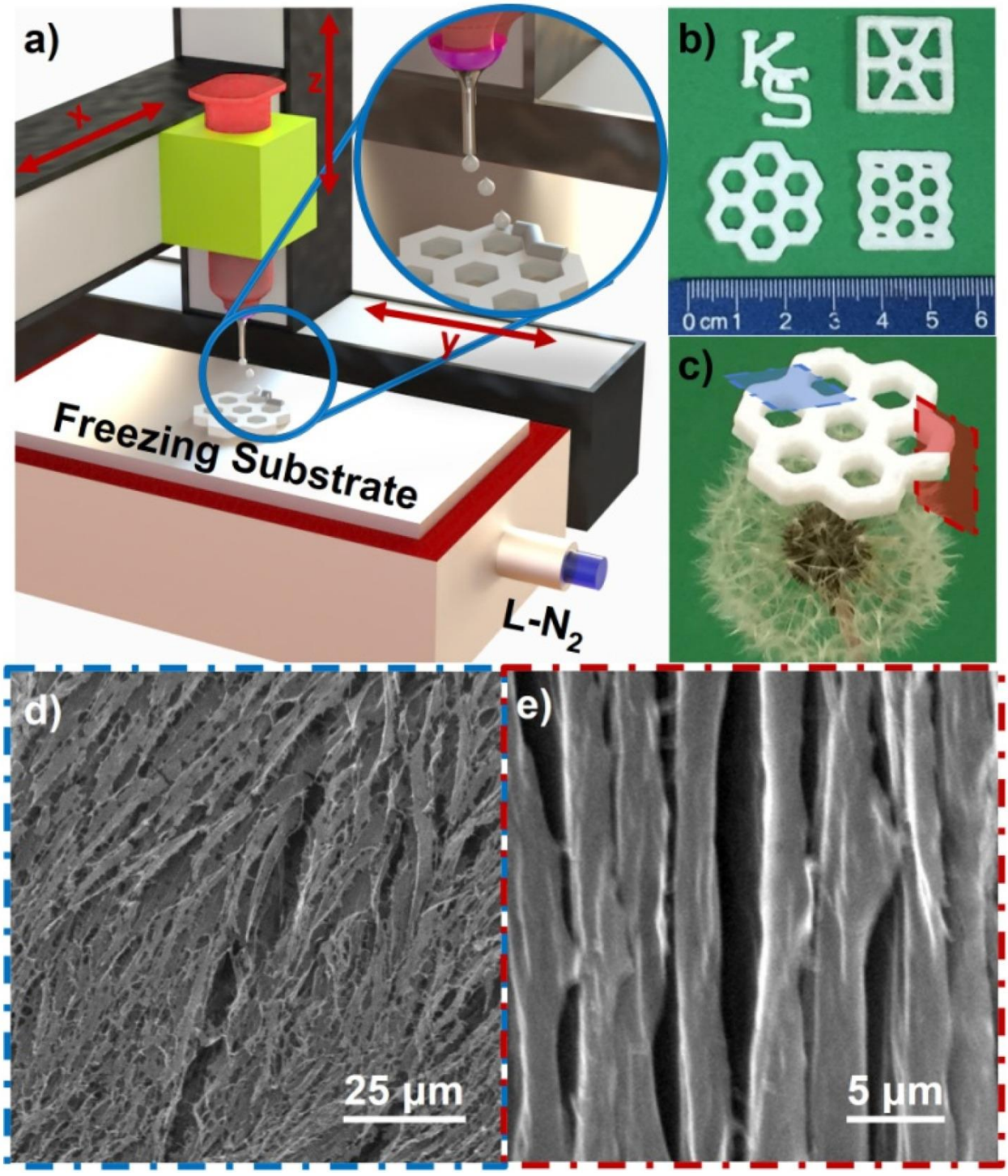

unidirectional freeze casting process.[16] As confirmed by the SEM images given in Figure 4.1d-e, the pore morphology on the top surface (the plane perpendicular to the freezing direction) is composed of a lamellar porosity with random orientation. In the cross sectional surface, which is parallel to the direction of freezing, we observed an aligned porosity along the freezing direction. The observed microstructure of the 3D printed CNC aerogels was in a good agreement with other reports in the literature, either unidirectional freeze casting of cellulose aerogels[10,11,21] or 3DFP of other materials[32–35].

Fabricating aerogels having truly 3D structures with overhang features has always been a great challenge. In DIW process, due to the shear-thinning behavior of the used ink, the viscosity is dramatically reduced with the application of pressure while extruding from the micro-sized nozzle. As the material is deposited and the pressure is removed, the viscosity of the ink is increased back and it becomes strong enough to support itself and protect its shape.[44] Li *et al.* benefited from this shear-thinning characteristics of the cellulose-based ink to fabricate bowl-like structures with overhang features.[27] Kam *et al.* on the other hand combined the shear-thinning behavior with freezing the deposited ink to achieve a quick fixation to fabricate bowl-like cellulosebased aerogels with overhang features.[30] Yet, none of these reports achieved aerogels having overhang truss structures standing on empty space. Håkansson *et al.* synthesized a highly charged carboxymethylated CNF-based ink with superior shear-thinning properties.[45] Due to the fast relaxation of the deposited ink, it was possible to print 10×10×10 mm^3 grid cubes, with 3×3×3 mm^3 pillars where the top square stands over the 4 mm gap between the corner pillars without using support material. However, the top square standing on empty space had serious issues considering the shape fidelity, which we believe is due to the lack of support structure during the 3D printing process.

Unlike the previous studies reporting 3D printed cellulose-based aerogels, our 3DFP method incorporates a DOD-based material deposition approach instead of extrusion-based deposition. Using a multimaterial additive manufacturing technique, which brings a higher level of design freedom, such as integrating structure and function to achieve tailorable material physical properties, and introducing a new degree of freedom to the 3D printed parts[46], we can use pure water as support material since it can be deposited in the form of droplets as the CNC-based aqueous ink. After deposition of the water droplets, they immediately freeze and preserve their shapes like the deposited ink. By incorporating multiple DOD heads in the printing system, one for the aqueous CNC ink and another for pure DI water as support material, we can fabricate truly 3D structures with overhang features as schematically explained in Figure 4.2a. Once the structure is completed, the support ice is easily removed (sublimated) from the material by the regularly applied freeze drying process without any need for a tedious and harsh chemical / thermal etching processes as seen in other methods. To provide the proof-of-concept for 3D printed aerogels with truly 3D structures, we designed and fabricated an egg-shell shape with multiple holes so that it would be consisting of multiple overhanging features as presented in Figure 4.2b. For this multi-material printing job, it was challenging to obtain identical lines from two different inks due to the difference in their rheological properties. By adjusting the jetting parameters such as pressure inside the syringe, jetting frequency, and duty cycle as explained in our previous study[35], we achieved uniform lines from water and aqueous CNC ink as identical as possible and successfully fabricated the truly 3D cellulose-based aerogels presented in Figure 4.2b. It should also be noted that the 3D printing setup used in this study is developed in our lab and the quality of the 3D printed aerogel can be increased by reducing the nozzle diameter and increasing the precision of the motion stage. We believe that our ability to fabricate aerogels with truly 3D structures will

Figure 4.2. a) Schematics of the 3D freeze printing process for printing the truly 3D structure with overhang features made possible by using DI water as support material and b) photographs showing the real pictures of the as prepared 3D freeze printed egg-shell shaped CNC aerogels having truly 3D structure with overhang features.

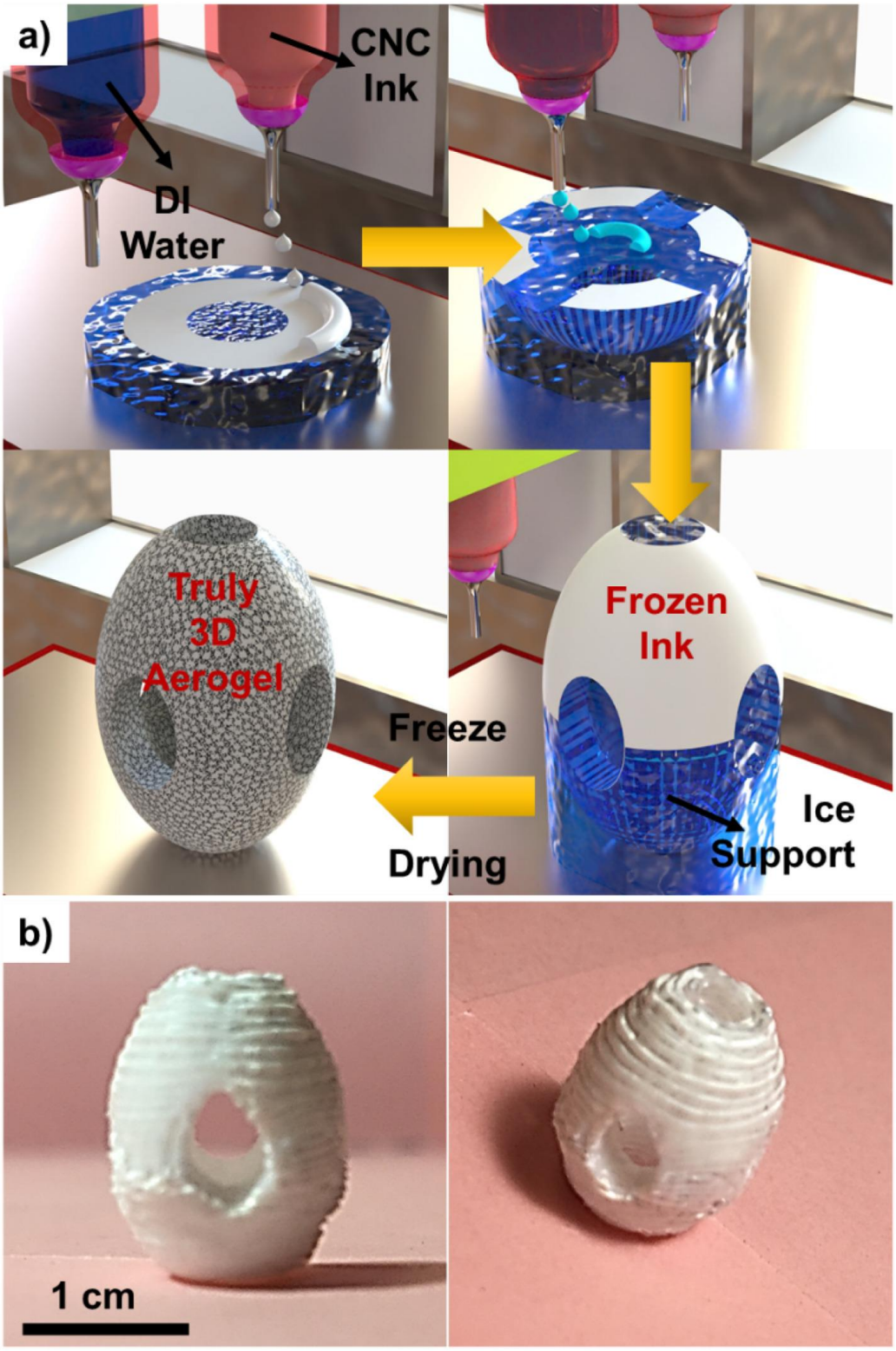

increase the freedom in the design, help to tune the material properties, and open new applications for cellulosic aerogels.

To characterize the mechanical properties of the 3D freeze printed CNC aerogels, fabricated cubic aerogels were compressed between two parallel plates attached to a universal testing device. To investigate the anisotropy in the mechanical properties of the fabricated aerogels, we tested them under uniaxial compression with the force applied parallel (axial) and perpendicular (radial) to the freezing direction (Figure 4.3a). As seen in Figure 4.3b in both orientations, we observed a linear elastic deformation region up to approximately 10% compressive strain. This can be attributed to the elastic deformation of the CNC walls and the compression of the pores. Following, the stress values slightly increase due to the plastic yielding of the cell walls which corresponds to a plateau region between 10 and 60% strain. Afterwards, the densification region, in which the stress increased dramatically, was observed between 60 and 90% strain.[47] The loading curves were similar to the previously reported freeze casted cellulose aerogels.[10,21] The maximum stress at 90% compressive strain was much lower in the radial direction (~61 kPa) compared to the axial direction (~351 kPa). This mechanical anisotropy is attributed to the anisotropic microstructure of the aerogel. Even though the maximum stress at 90% strain is much lower in the radial direction, compression recovery properties were found to be much better in this direction (see Figure 4.3c-f). This anisotropy in the mechanical properties of the 3D freeze printed CNC aerogels is in a good agreement with the previous reports.[48]

We further measured the mechanical response of the aerogels against a five-stepped compressive loading-unloading strains up to 50% strain with 10% increments in axial (Figure 4.3c) and radial (Figure 4.3d) directions. The anisotropic properties (higher maximum stress in the axial direction, better recovery in the radial direction) of the aerogels were also noticed in these tests. In

Figure 4.3. a) Schematics showing the orientation of the samples for mechanical compression tests. b) Stress-strain plots of the aerogels after uniaxial compression tests with axial and radial alignment up to 90% compressive strain. c) Stress-strain curves of multicycle compression in axial direction by increasing strain amplitude of printed CNC aerogels. d) Stress-strain curves of multicycle compression in radial direction by increasing strain amplitude of printed CNC aerogels. e) Stress-strain curves for 100 loading-unloading cycles up to 25% strain in axial direction. f) Stress-strain curves for 100 loading-unloading cycles up to 25% strain in radial direction.

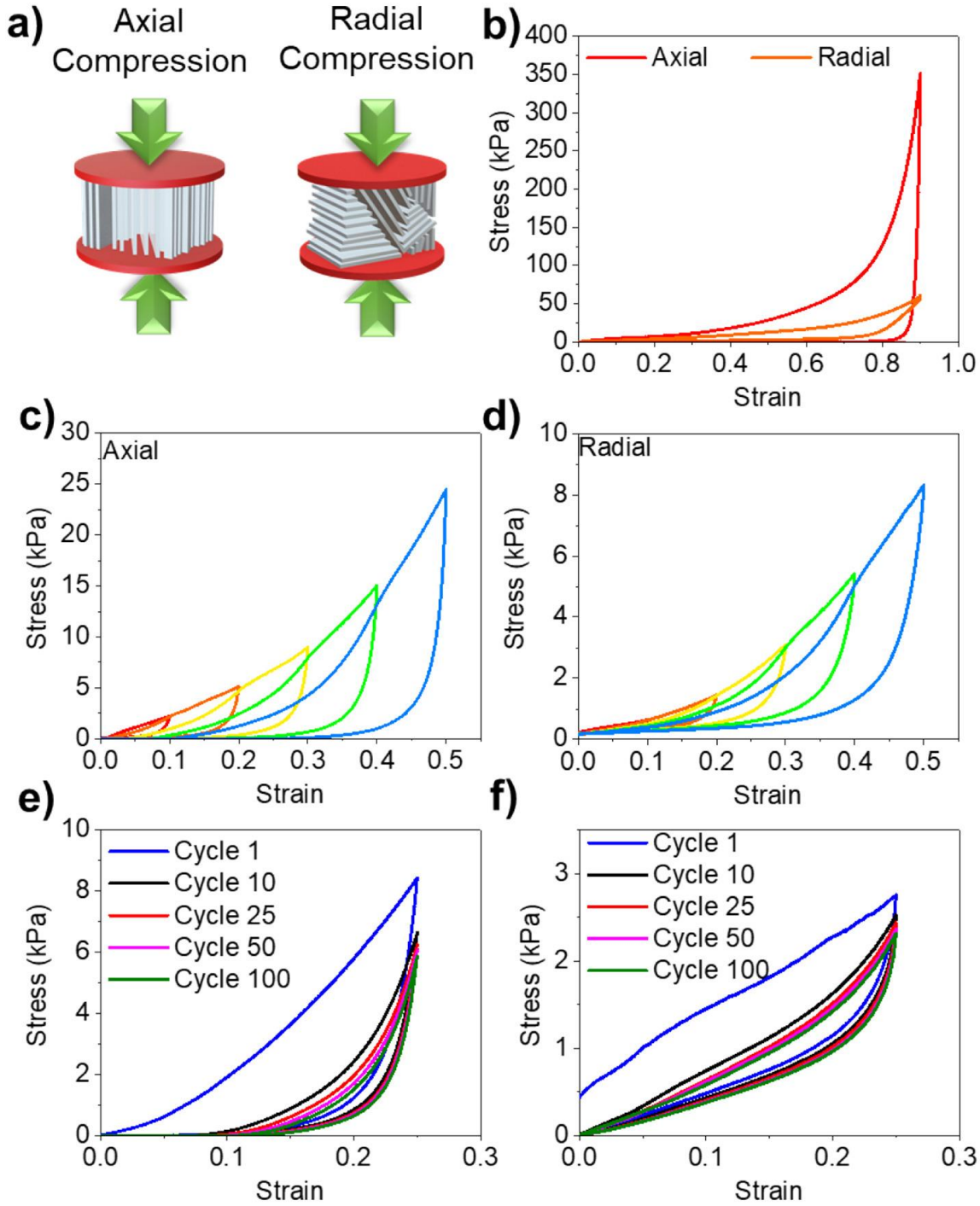

both tests, we observed that the succeeding stress-strain curve almost rises back to the stress level measured at the maximum strain value of the previous cycle. This trend was repeated for all increment values and it indicates an excellent strain memory effect.[49] The stress-strain curves obtained after multicycle (100 cycles) compression tests applied up to 25% strain are given in Figure 4.3e and f for a compression in axial and radial direction. The maximum stress at 25% strain observed in the axial direction reduced from 8.43 kPa to 5.85 kPa at the end of 100th compression, which corresponds to a stress decay of ~30%. In the radial direction, this decay (from 2.76 kPa to 2.31 kPa) remained at around 16%.

Cellulose is rich in hydroxyl groups among which hydrogen bonds are formed. These hydrogen bonds are the reason for the macroscopic integrity of cellulose-based aerogels. However, the hydrogen bond among cellulose nanoparticles can be replaced by cellulose-water hydrogen bond, which leads to the collapse of the aerogels when immersed in water.[50,51] (Figure 4.4a). In order to make cellulose-based aerogels suitable for applications such as bioengineering[51], and liquid absorption[50,52], it is essential to fabricate a strong aerogel by covalent bond of crosslinking in order to be stable in water.[51] Polyamide-epichlorohydrin resin which is widely used as wet strength additive in paper industry, was used for cross-linking cellulose-based aerogels to provide strength in water.

Previously reported cellulose-based aerogels cross-linked with PAE resin have been fabricated by freeze-casting[50–52] or DIW-based 3D printing[27,28] methods. To show the printability of the aqueous CNC ink mixed with PAE resin, we have added a weighted amount of PAE resin into the 2 wt. % CNC ink so that final mass ratio of dry CNC to PAE resin would be 5:1, and mixed them using a mechanical stirring process. After fabricating 3D printed CNC aerogels with and without crosslinking, we have tested their wet strength by immersing them in

Figure 4.4. a) Collapse of the uncross-linked CNC aerogel when immersed in water. b) CNC aerogel cross-linked with PAE resin protects its structural integrity and shape when immersed in water.

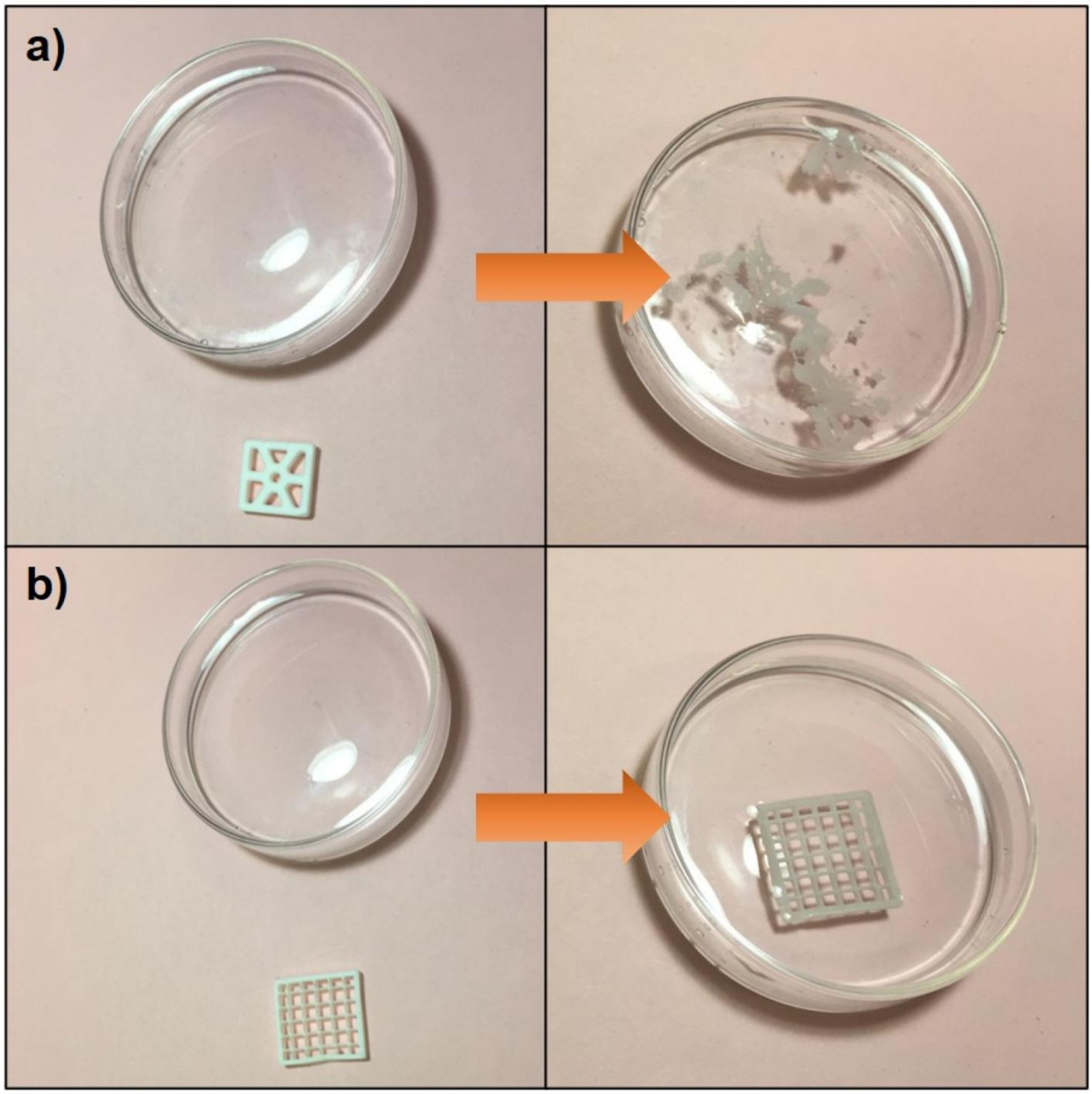

water. The CNC aerogel without the cross-linking had a structural collapse within seconds after immersion in water as seen in Figure 4.4a. Cross-linked CNC aerogel with PAE resin on the other hand, protected its structural integrity and shape in water (Figure 4.4b), which showed the potential of the 3D freeze printed aerogels in biomedical, tissue engineering, and liquid absorption applications.

Cellulose is an excellent reinforcing agent for nanocomposites due to its high strength and stiffness.[53] Nanoparticles derived from cellulose has been used as reinforcing agent in many composite aerogels such as CNF/graphene[54], CNF/reduced graphene oxide (rGO)/carbon nanotube (CNT)[55], CNF/silver nanoparticles[56], and so on. Conducting polymers are also frequently blended with cellulosic nanoparticles for novel applications where the biopolymers provide hierarchical flexibility, improved performance, mechanical stability, processability, and biocompatibility to the pure conducting polymer.[57] Composites of PEDOT:PSS, which is a well-known conductive polymer have been used with cellulosic nanoparticles to fabricate aerogels for different applications such as solar steam generation[58], pressure–temperature sensing[59], pressure–temperature–humidity sensing[60], and strain sensing[61] applications by freeze-casting method. However, 3D printing of cellulose nanoparticle–PEDOT:PSS aerogels, which can provide a freedom in the design and manufacturing and open other potential applications, has not been reported yet.

To fabricate 3D freeze printed CNC – PEDOT:PSS aerogels, we mixed the 2 wt. % aqueous CNC ink with a commercially available PEDOT:PSS suspension with 1:1 weight ratio using a mechanical stirring process. Prepared mixture was then 3D freeze printed as explained before. The fabricated CNC – PEDOT:PSS aerogels had an average ultralight density of ~11.6 mg cm^{-3} as seen in Figure 4.5a. The electrical conductivity of the composite aerogels is demonstrated in Figure 4.5b. The micropore morphology of the CNC – PEDOT:PSS aerogels were similar to the pure CNC aerogels: lamellar pores with a random alignment on the plane perpendicular to the freezing direction (Figure 4.5c), and lamellar pores aligned along the freezing direction on the plane parallel with the freezing direction (Figure 4.5d). To investigate the effect of CNC reinforcement in the mechanical properties of PEDOT:PSS aerogels, we fabricated cubic structures with a unit

Figure 4.5. a) 3D freeze-printed CNC aerogel functionalized with PEDOT:PSS. b) Experimental setup demonstrating the conductivity of the 3D freeze printed CNC-PEDOT:PSS aerogels. c) SEM image showing the top surface of the 3D freeze-printed CNC-PEDOT:PSS aerogels. d) SEM image showing the top cross-sectional surface of the 3D freeze printed CNC-PEDOT:PSS aerogels. e) Stress-strain plots of the aerogels having different ink formulations after uniaxial compression tests with axial alignment up to 90% compressive strain. f) Stress-strain curves for 10 loading-unloading cycles up to 10% strain in axial direction. g) Response in the resistance of a CNC-PEDOT:PSS aerogel to a compression with 10% strain for 10 consecutive cycles. h) Response in the resistance of a CNC-PEDOT: PSS aerogel to a 30° bending for 10 consecutive cycles.

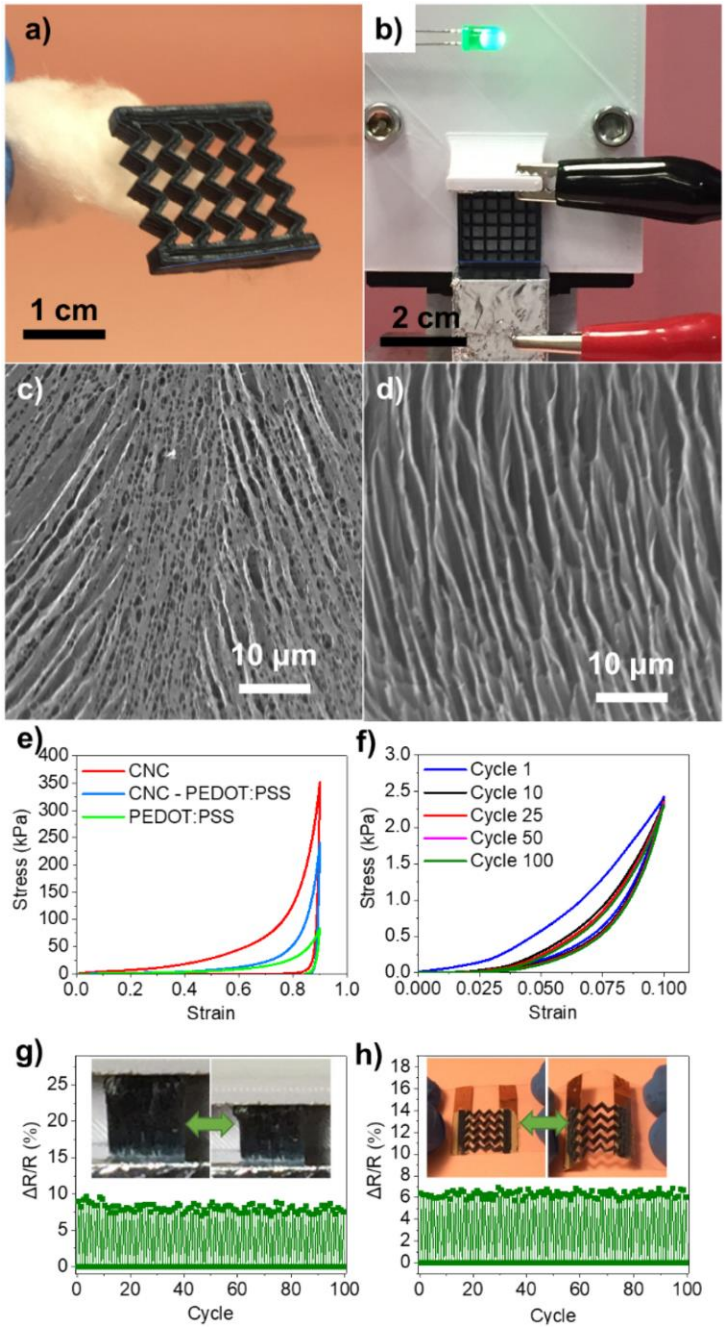

dimension of 7.5 mm and performed uniaxial compression tests in axial direction. The maximum stress at 90% compressive strain increased with the increasing amount of CNC in the aerogels (Figure 4.5e). Multicycle compression test further revealed the great resilience of the 3D freeze printed CNC-PEDOT:PSS aerogels.

In order to further investigate the mechanical robustness of the structure, as shown in Figure 4.5f, 3D freeze-printed specimens were compressed for 100 cycles up to 10% strain. The second loading-unloading curve exhibited a stress degradation less than 1%, meaning that the 3D freeze-printed aerogels maintain their original elasticity and structural robustness. After 100 loops, the stress response at 10% strain was stabilized at approximately 2.31 kPa, which corresponds to a ~4.4% stress decay. To further characterize the piezoresistive behavior of the 3D freeze-printed CNC–PEDOT:PSS aerogels after applied compression, we applied 100 cycles of mechanical compression up to 10% strain value and simultaneously measured the change in the resistance (Figure 4.5g). The change in the electrical resistance of the fabricated aerogels highly stable (average $\Delta R/R = 8\%$) over multiple cycles (100 cycles) of compression, indicating a significant structural resilience.[62] The change in the electrical resistance (average $\Delta R/R = \sim 6.3\%$) was also highly stable over multiple bending cycles (100 cycles), which shows the suitability of the 3D freeze-printed CNC–PEDOT:PSS aerogels for flexible/wearable electronics applications.

Conclusion

In this study, using a novel additive manufacturing method, we fabricated aerogels based on cellulose. Our method made it possible to use water as support material during the 3D printing process so that we achieved truly 3D aerogels with overhang features without need to chemical and/or thermal etching processes. This unique advantage of our printing technique increases the freedom in material design, and also can lead to new potential applications for cellulose-based

aerogels. To the best of our knowledge, this is the first study reporting cellulose-based aerogels with overhang features made possible by incorporating a support material during the additive manufacturing process. Furthermore, it is the first report investigating DOD-based 3D printed cellulose aerogels with covalent cross-linking to achieve stability in water and functionalized with PEDOT:PSS.

References

[1] Long L-Y, Weng Y-X, Wang Y-Z. Cellulose aerogels: synthesis, applications, and prospects. Polymers 2018;10(6):623.

[2] Brown Jr RM. Cellulose structure and biosynthesis: what is in store for the 21st century? J Polym Sci A Polym Chem 2004;42(3):487–95. [3] Hon DNS. In: Buschow KHJ, et al., editors. Cellulose: chemistry and technology, in encyclopedia of materials: science and technology. Elsevier: Oxford; 2001. p. 1039–45.

[4] Moon RJ, Martini A, Nairn J, Simonsen J, Youngblood J. Cellulose nanomaterials review: structure, properties and nanocomposites. Chem Soc Rev 2011;40(7): 3941–94.

[5] Moon RJ, Schueneman GT, Simonsen J. Overview of cellulose nanomaterials, their capabilities and applications. Jom 2016;68(9):2383–94.

[6] De France KJ, Hoare T, Cranston ED. Review of hydrogels and aerogels containing nanocellulose. Chem Mater 2017;29(11):4609–31.

[7] Lavoine N, Bergstrom ¨ L. Nanocellulose-based foams and aerogels: processing, properties, and applications. J Mater Chem A 2017;5(31):16105–17.

[8] Du A, Zhou B, Zhang Z, Shen J. A special material or a new state of matter: a review and reconsideration of the aerogel. Materials 2013;6(3):941–68.

[9] Wan C, Jiao Y, Wei S, Zhang L, Wu Y, Li J. Functional nanocomposites from sustainable regenerated cellulose aerogels: a review. Chem Eng J 2018;359: 459–75.

[10] Donius AE, Liu A, Berglund LA, Wegst UG. Superior mechanical performance of highly porous, anisotropic nanocellulose–montmorillonite aerogels prepared by freeze casting. J Mech Behav Biomed Mater 2014;37:88–99.

[11] Dash R, Li Y, Ragauskas AJ. Cellulose nanowhisker foams by freeze casting. Carbohydr Polym 2012;88(2):789–92.

[12] Wicklein B, Kocjan A, Salazar-Alvarez G, Carosio F, Camino G, Antonietti M, et al. Thermally insulating and fire-retardant lightweight anisotropic foams based on nanocellulose and graphene oxide. Nat Nanotechnol 2015;10(3):277.

[13] Munier P, Gordeyeva K, Bergstrom ¨ L, Fall AB. Directional freezing of nanocellulose dispersions aligns the rod-like particles and produces low-density and robust particle networks. Biomacromolecules 2016;17(5):1875–81.

[14] Fukasawa T, Ando M, Ohji T, Kanzaki S. Synthesis of porous ceramics with complex pore structure by freeze-dry processing. J Am Ceram Soc 2001;84(1):230–2.

[15] Deville S. Freeze-casting of porous ceramics: a review of current achievements and issues. Adv Eng Mater 2008;10(3):155–69.

[16] Scotti KL, Dunand DC. Freeze casting–a review of processing, microstructure and properties via the open data repository, FreezeCasting.net. Prog Mater Sci 2018;94: 243–305.

[17] Li W, Lu K, Walz J. Freeze casting of porous materials: review of critical factors in microstructure evolution. Int Mater Rev 2012;57(1):37–60.

[18] Or T, Saem S, Esteve A, Osorio DA, France KJ De, Vapaavuori J, et al. Patterned cellulose nanocrystal aerogel films with tunable dimensions and morphologies as ultra-porous scaffolds for cell culture. ACS Appl Nano Mater 2019;2(7):4169–79.

[19] Jim´enez-Saelices C, Seantier B, Cathala B, Grohens Y. Effect of freeze-drying parameters on the microstructure and thermal insulating properties of nanofibrillated cellulose aerogels. J Sol-Gel Sci Technol 2017;84(3):475–85.

[20] Chu G, Qu D, Zussman E, Xu Y. Ice-assisted assembly of liquid crystalline cellulose nanocrystals for preparing anisotropic aerogels with ordered structures. Chem Mater 2017;29(9):3980–8.

[21] Zhang X, Liu M, Wang H, Yan N, Cai Z, Yu Y. Ultralight, hydrophobic, anisotropic bamboo-derived cellulose nanofibrils aerogels with excellent shape recovery via freeze-casting. Carbohydr Polym 2019;208:232–40.

[22] Jiang Y, Xie X, Chen Y, Liu Y, Yang R, Sui G. Hierarchically structured cellulose aerogels with interconnected MXene networks and their enhanced microwave absorption properties. J Mater Chem C 2018;6(32):8679–87.

[23] Zeng Z, Wu T, Han D, Ren Q, Siqueira G, Nystrom ¨ G. Ultralight, flexible, and biomimetic nanocellulose/silver nanowire aerogels for electromagnetic interference shielding. ACS Nano 2020;14(3):2927–38.

[24] Zhou L, Zhai S, Chen Y, Xu Z. Anisotropic cellulose nanofibers/polyvinyl alcohol/graphene aerogels fabricated by directional freeze-drying as effective oil adsorbents. Polymers 2019;11(4):712.

[25] Chen Z, Hu Y, Zhuo H, Liu L, Jing S, Zhong L, et al. Compressible, elastic, and pressure-sensitive carbon aerogels derived from 2D titanium carbide nanosheets and bacterial cellulose for wearable sensors. Chem Mater 2019;31(9):3301–12.

[26] Zhang Z, Yan J, Kuriyagawa T. Manufacturing technologies toward extreme precision. Int J Extreme Manufact 2019;1(2):022001.

[27] Li VC-F, Dunn CK, Zhang Z, Deng Y, Qi HJ. Direct ink write (DIW) 3D printed cellulose nanocrystal aerogel structures. Sci Rep 2017;7(1):1–8.

[28] Li VC, Mulyadi A, Dunn CK, Deng Y, Qi HJ. Direct ink write 3D printed cellulose nanofiber aerogel structures with highly deformable, shape recoverable, and functionalizable properties. ACS Sustain Chem Eng 2018;6(2):2011–22.

[29] Jiang J, Oguzlu H, Jiang F. 3D printing of lightweight, super-strong yet flexible allcellulose structure. Chem Eng J 2020;405:126668.

[30] Kam D, Chasnitsky M, Nowogrodski C, Braslavsky I, Abitbol T, Magdassi S, et al. Direct Cryo writing of aerogels via 3D printing of aligned cellulose Nanocrystals inspired by the plant Cell Wall. Colloids and Interfaces 2019;3(2):46.

[31] Qian C, Li L, Gao M, Yang H, Cai Z, Chen B, et al. All-printed 3D hierarchically structured cellulose aerogel based triboelectric nanogenerator for multi-functional sensors. Nano Energy 2019;63:103885.

[32] Zhang Q, Zhang F, Medarametla SP, Li H, Zhou C, Lin D. 3D printing of graphene aerogels. Small 2016;12(13):1702–8.

[33] Brown E, Yan P, Tekik H, Elangovan A, Wang J, Lin D, et al. 3D printing of hybrid MoS2-graphene aerogels as highly porous electrode materials for sodium ion battery anodes. Mater Des 2019;170:107689.

[34] Ma C, Wang R, Tetik H, Gao S, Wu M, Tang Z, et al. Hybrid nanomanufacturing of mixed-dimensional manganese oxide/graphene aerogel macroporous hierarchy for ultralight efficient supercapacitor electrodes in self-powered ubiquitous nanosystems. Nano Energy 2019;66:104124.

[35] Yan P, Brown E, Su Q, Li J, Wang J, Xu C, et al. 3D printing hierarchical silver nanowire aerogel with highly compressive resilience and tensile elongation through tunable poisson's ratio. Small 2017;13(38):1701756.

[36] Tetik H, Lin D. 3D freeze printing: development of an experimental setup and determination of 3D printing parameters. In: International manufacturing science and engineering conference. American Society of Mechanical Engineers; 2020.

[37] Tetik H, Yang G, Tan W, Fong A, Lei S, Weker JN, et al. High speed in-situ X-ray imaging of 3D freeze printing of aerogels. Addit Manuf 2020;36:101513.

[38] Derby B. Inkjet printing of functional and structural materials: fluid property requirements, feature stability, and resolution. Annu Rev Mat Res 2010;40: 395–414.

[39] Nayak L, Mohanty S, Nayak SK, Ramadoss A. A review on inkjet printing of nanoparticle inks for flexible electronics. J Mater Chem C 2019;7(29):8771–95.

[40] Derby B. Inkjet printing ceramics: from drops to solid. J Eur Ceram Soc 2011;31 (14):2543–50.

[41] Cummins G, Desmulliez MP. Inkjet printing of conductive materials: a review. Circuit World; 2012.

[42] Reis N, Derby B. Ink jet deposition of ceramic suspensions: modeling and experiments of droplet formation. MRS Online Proceedings Library Archive 2000: 625.

[43] Daerr A, Mogne A. Pendent_drop: an imagej plugin to measure the surface tension from an image of a pendent drop. J Open Res Softw 2016;4(1).

[44] Smay JE, Cesarano J, Lewis JA. Colloidal inks for directed assembly of 3-D periodic structures. Langmuir 2002;18(14):5429–37.

[45] Håkansson KM, Henriksson IC, de la Pena ˜ Vazquez ´ C, Kuzmenko V, Markstedt K, Enoksson P, et al. Solidification of 3D printed nanofibril hydrogels into functional 3D cellulose structures. Adv Mater Technol 2016;1(7):1600096.

[46] Cheng D, Li L. An overview of laser-based multiple metallic material additive manufacturing: from macro-to micro-scales. Int J Extreme Manufact 2020;3: 012003.

[47] Chen B, Zheng Q, Zhu J, Li J, Cai Z, Chen L, et al. Mechanically strong fully biobased anisotropic cellulose aerogels. RSC Adv 2016;6(99):96518–26.

[48] Zhang X, Wang H, Cai Z, Yan N, Liu M, Yu Y. Highly compressible and hydrophobic anisotropic aerogels for selective oil/organic solvent absorption. ACS Sustain Chem Eng 2018;7(1):332–40.

[49] Zhu C, Han TY-J, Duoss EB, Golobic AM, Kuntz JD, Spadaccini CM, et al. Highly compressible 3D periodic graphene aerogel microlattices. Nat Commun 2015;6(1): 1–8.

[50] Zhang W, Zhang Y, Lu C, Deng Y. Aerogels from crosslinked cellulose nano/microfibrils and their fast shape recovery property in water. J Mater Chem 2012;22(23): 11642–50.

[51] Ghafari R, Jonoobi M, Amirabad LM, Oksman K, Taheri AR. Fabrication and characterization of novel bilayer scaffold from nanocellulose based aerogel for skin tissue engineering applications. Int J Biol Macromol 2019;136:796–803.

[52] Feng J, Nguyen ST, Fan Z, Duong HM. Advanced fabrication and oil absorption properties of super-hydrophobic recycled cellulose aerogels. Chem Eng J 2015;270: 168–75.

[53] Madyan OA, Fan M, Feo L, Hui D. Enhancing mechanical properties of clay aerogel composites: an overview. Compos Part B Eng 2016;98:314–29.

[54] Yao X, Yu W, Xu X, Chen F, Fu Q. Amphiphilic, ultralight, and multifunctional graphene/nanofibrillated cellulose aerogel achieved by cation-induced gelation and chemical reduction. Nanoscale 2015;7(9):3959–64.

[55] Zheng Q, Cai Z, Ma Z, Gong S. Cellulose nanofibril/reduced graphene oxide/carbon nanotube hybrid aerogels for highly flexible and all-solid-state supercapacitors. ACS Appl Mater Interfaces 2015;7(5):3263–71.

[56] Dong H, Snyder JF, Tran DT, Leadore JL. Hydrogel, aerogel and film of cellulose nanofibrils functionalized with silver nanoparticles. Carbohydr Polym 2013;95(2): 760–7.

[57] Belaineh D, Andreasen JW, Palisaitis J, Malti A, Håkansson K, Wågberg L, et al. Controlling the organization of PEDOT: PSS on cellulose structures. ACS Appl Polym Mater 2019;1(9):2342–51.

[58] Han S, Ruoko TP, Gladisch J, Erlandsson J, Wågberg L, Crispin X, et al. Celluloseconducting polymer aerogels for efficient solar steam generation. Adv Sustain Syst 2020;4:2000004.

[59] Han S, Jiao F, Khan ZU, Edberg J, Fabiano S, Crispin X. Thermoelectric polymer aerogels for pressure–temperature sensing applications. Adv Funct Mater 2017;27 (44):1703549.

[60] Han S, Alvi NUH, Granlof ¨ L, Granberg H, Berggren M, Fabiano S, et al. A multiparameter pressure–temperature–humidity sensor based on mixed ionic–electronic cellulose aerogels. Adv Sci 2019;6(8):1802128.

[61] Zhou J, Hsieh Y-L. Conductive polymer protonated nanocellulose aerogels for tunable and linearly responsive strain sensors. ACS Appl Mater Interfaces 2018;10 (33):27902–10.

[62] Qiu L, Liu JZ, Chang SL, Wu Y, Li D. Biomimetic superelastic graphene-based cellular monoliths. Nat Commun 2012;3(1):1–7.

Chapter 5 - 3D Freeze Printing of MXene Aerogels[4]

The outstanding electronic, mechanical, electrochemical, and optical properties of 2D MXenes, have attracted much research interest since their discovery in 2011.[1] MXenes are transition metal carbides, nitrides, and carbonitrides produced by a selective etching of metal "A" layer atoms from their corresponding "MAX" phases. The term "MAX" phase refers to a group of layered ceramics of the chemical composition of "$M_{n+1}AX_n$", where "M" stands for an early transition metal, "A" is an A group element, and "X" is carbon and/or nitrogen.[2–6] MXenes have shown exceptional properties such as high electrical conductivity, hydrophilicity, and the ability to intercalate different cations between their layers.[6–10] However, similar to other 2D materials, the performance of MXenes for some applications is affected by their tendency to restack and/or aggregate during assembly.[11,12] To overcome this issue, various methods are successfully utilized to integrate 2D materials into 3D macroscopic architectures with attractive properties such as ultralight feature, high porosity, and large specific surface area.[13–15] $Ti_3C_2T_x$, which is produced by selective etching of Al atoms from Ti_3AlC_2 MAX phase, is the first discovered and the most studied MXene,[16] and macroscopic 3D porous structures fabricated from $Ti_3C_2T_x$ and its composites have shown great promise for a variety of applications,[12] including electrochemical energy storage,[15,17–20] electromagnetic interference shielding,[21–27] sensing applications,[28–30] photothermal energy conversion,[31,32] water/oil separation,[33] and solar desalination applications.[34]

[4] Reprinted with permission from "3D Printed MXene Aerogels with Truly 3D Macrostructure and Highly Engineered Microstructure for Enhanced Electrical and Electrochemical Performance" by Halil Tetik, Jafar Orangi, Guang Yang, Keren Zhao, Shakir Bin Mujib, Gurpreet Singh, Majid Beidaghi, and Dong Lin, 2021. Advanced Materials, 34, 2104980. 2021 Wiley-VCH GmbH

Unidirectional freeze casting (UFC) method has been previously utilized for the fabrication of macroscopic 3D porous structures from $Ti_3C_2T_x$ and its composites. In this method, prepared gels or suspensions of $Ti_3C_2T_x$ sheets and other components are frozen by applying a unidirectional temperature gradient. Ice crystals nucleate on the cold surface and grow along the temperature gradient. $Ti_3C_2T_x$ sheets are expelled by the growing ice crystals and aligned along the freezing direction forming a tightly packed continuous network.[24] This well-ordered microstructure obtained after UFC have shown great benefits for a variety of applications. For instance, Bian *et al.* utilized UFC to fabricate pristine $Ti_3C_2T_x$ aerogels for electromagnetic interference (EMI) shielding applications.[26] Their aerogels' specific shielding effectiveness reached 9904 dB cm^3 g^{-1}, which is the highest value reported for foam-like materials. Other studies also reported aerogels that are composites of $Ti_3C_2T_x$ and reduced graphene oxide,[21] sodium alginate,[24] nanocellulose,[25] and gelatin,[27] fabricated through UFC. The high EMI shielding performances of those aerogels are attributed to their ultralight density, high conductivity, and highly ordered porous microstructure. Cai *et al.* demonstrated that highly ordered microstructures of $Ti_3C_2T_x$-based aerogels fabricated by UFC are highly efficient for solar absorption and show fast capillarity-driven oil absorption capability.[31]

Moreover, MXene aerogels have been widely explored as electrodes for electrochemical energy storage devices. Engineering electrode structures to enhance their ionic and electronic conductivity can significantly affect the electrochemical properties including rate capability.[12] Yang *et al.* fabricated porous $Ti_3C_2T_x$ films using UFC to achieve a homogeneous microstructure that is composed of vertically aligned MXene walls within lamellar pores.[35] Supercapacitor electrodes based on the MXene films exhibited remarkably high gravimetric and areal power density of 150 kW kg^{-1} at 10 00 A g^{-1} and 667 mW cm^{-2} at 4444 mA cm^{-2}, respectively. The

performance of the $Ti_3C_2T_x$-based porous supercapacitor electrode films was attributed to the efficient ion transport created by well-ordered microstructure that allows for fast electrochemical charge–discharge cycles. In our previous study, we have demonstrated the critical role of microstructure on the mechanical, electrical, and electrochemical properties of MXene aerogels by fabrication of aerogels with ordered $Ti_3C_2T_x$ sheets through UFC.[15] Lithium-ion capacitor electrodes made from those aerogels delivered a significantly high specific capacity (≈1210 mAh g^{-1} at 0.05 A g^{-1}), excellent rate capability (≈200 mAh g^{-1} at 10 A g^{-1}), and outstanding cycling performance due to their highly ordered and well-engineered microstructure.

Although UFC provided porous $Ti_3C_2T_x$ bodies with well-ordered microstructure, which was proven to be beneficial for multiple applications, this method lacks the ability of fabricating porous bodies with complex, engineered macrostructures since it is a mold-based fabrication approach. For applications such as electrochemical energy storage devices, where the geometry, architecture, and micropore morphology of the electrode play a crucial role in the capacitive behavior, fabrication of devices with tailored hierarchical architectures involving micro-, meso-, and macropores is a significant challenge.[12,14,36,37] To address this issue, Li *et al.* performed the extrusion-based 3D printing and followed with UFC to fabricate thick interdigitated micro-supercapacitors (MSCs) from $Ti_3C_2T_x$-based aerogels.[38] Highly ordered honeycomb-like microporous architectures were obtained after directional freezing facilitated the infiltration of the electrolyte into the internal active sites, which can improve electrochemical performance and also improve resilience to deformation.[38]

Despite the recent advances in 3D printing of MXenes, due to the limitations of extrusion-based 3D printing, truly 3D architectures with overhang features or changing cross-sectional geometry is often difficult to fabricate without using tedious chemical/thermal post-processes. In

the previous reported 3D printed MXene aerogels, extrusion-based 3D printing methods have been used and fabricated structures had to have constant cross-sectional geometries due to lack of support material that can easily be removed after the printing process.[38–40] Also, controlling the orientation of MXene sheets in the printed structure has been challenging. As we have demonstrated in this paper, the ability to control the orientation of sheets in both horizontal and vertical directions allows engineering the microstructure of the prints, improve their performance, and extend their applications.

Here, we report on the fabrication of ultralight and truly 3D MXene aerogel structures using 3D freeze-printing (3DFP) method. This novel fabrication method combines UFC and drop-on-demand inkjet printing to tailor the micro- and macrostructure of the aerogels.[41–45] Unlike extrusion-based 3D printing, 3DFP does not require a viscoelastic shear-thinning ink and can use water (ice) as supporting material to fabricate truly 3D structures with overhang features. In this study, we performed mechanical, electrical, and electrochemical characterization of the 3DFP $Ti_3C_2T_x$ aerogels to evaluate their potential for different applications such as piezoresistive sensing, flexible/wearable electronics, and MSC devices. Furthermore, with the advantages provided by our inkjet-based 3D printing method, we fabricated all-MXene MSC devices that are composed of current collector and porous electrodes with controlled orientation of MXene sheets. 3D printed all-MXene MSC devices with engineered microstructure, composed of both horizontally and vertically aligned MXene sheets demonstrated the importance of MXene sheets alignment on the electrochemical performance of the MSCs. The results showed that the current collector layer with horizontally aligned MXenes helps enhancing the electrical conductivity whereas the vertically aligned layer with high porosity provides better ion transport and improved performance at high scan rates. To the best of our knowledge, this is the first report proposing all-

solid state MXene MSC devices with both horizontally and vertically aligned MXene sheets. Our results demonstrate 3DFP as a simple, straightforward, and inexpensive electrode fabrication method with great customizability to engineer electrode's micro- and macrostructure.

Experimental

Preparation of $Ti_3C_2T_x$ Dispersions

$Ti_3C_2T_x$ dispersions were prepared according to a previously reported method.[46] Briefly, concentrated hydrochloric acid (HCl, ACS Grade, BDH) solution was diluted with DI water to obtain 20 mL of 9 m HCl solution. About 1.6 g lithium fluoride (LiF, 98+% purity, Alfa Aesar) was added to the solution and stirred for 10 min using Teflon-coated magnetic stir bars at room temperature. Then, 1 g of Ti_3AlC_2 powder was slowly added to the solution. The mixture was transferred to a hot bath and kept at 35°C for 24 h while stirring. The mixture was then washed several times with DI water and centrifuged at 3500 rpm until the supernatant pH reaches ≈6. The supernatant in each washing step was collected and the concentration was adjusted to desired values using super-absorbing polymer balls.[14] The dispersion then used to print all MXene-based aerogels and MSC electrodes.[14]

3D Freeze Printing

Details of the 3D printing setup[76] and 3DFP process[47] were explained in the previous reports. Briefly, a 3-axis motion stage (Panowin Technologies, Shanghai, China) was used to manipulate the inkjet printing head, which was composed of a syringe barrel (Nordson EFD, RI, USA) and a solenoid inkjet dispenser (The Lee Co, CT, USA) connected to a 100 μm nozzle tip. $Ti_3C_2T_x$ suspension with various concentrations was loaded inside the syringe barrel and the internal pressure was controlled using a pneumatic fluid dispenser (Nordson EFD, RI, USA). Droplets of $Ti_3C_2T_x$ suspension that were generated by the inkjet dispenser were deposited on to

the substrate whose temperature was controlled by liquid nitrogen (LN_2) operated hot/cold plate (Instec, CO, USA). Silicon wafer substrates (unless otherwise specified) and a cold plate temperature of -20°C were used. Once 3D freeze printing of samples was completed, they were freeze dried by a commercially available freeze dryer (Labconco, MO, USA) at -35°C and 0.02 mbar for at least 48 h.

Material Characterization

The microstructure of the 3DFP $Ti_3C_2T_x$ aerogels was investigated by SEM (FEI HELIOS Nanolab 600i, OR, USA). For mechanical, electrical, and thermoelectrical characterization, cubic samples with dimensions of 5 × 5 × 5 mm were fabricated using MXene dispersions with concentrations of 9, 12, and 15 mg mL^{-1}. For in-plane compression tests, a digital material testing device (Shimadzu Universal Testing Machine, Kyoto, Japan) was used. All the compression tests were performed with a constant compression rate of 1 mm min^{-1}. The $V-I$ plots for obtaining the electrical conductivity properties of the MXene aerogels were obtained using a CHI 760D electrochemical workstation (CH Instruments, Austin, TX). For determination of the piezoelectric behavior, the resistance of the aerogels was measured by a two-probe method using a digital multimeter (Fluke 287) by a sampling interval of 2 Hz. The electrodes were painted with high conductive silver paste (≈0.01 Ω cm) on two sides of the samples to eliminate contact resistance. All the samples were placed between the compression (for mechanical characterization) or copper plates (for electrical characterization) so that the freezing direction is parallel to the surface normal of compression/copper plates unless otherwise stated.

Symmetrical MSCs were 3DFP using 15 mg mL^{-1} dispersion and their electrochemical performances were tested using a VMP3 potentiostat (Biologic, France). Pieces of silver wire were used to connect the printed electrodes to the potentiostat cables. Silver adhesive (fast-drying Ag

paint, SPI Supplies) was used to connect silver wires with the current collectors/electrodes. To cover the contact area to protect the silver paint and wires from the electrolyte, nail polish was used. The PVA/H_2SO_4 gel electrolyte was carefully drop cast onto the printed $Ti_3C_2T_x$ interdigital electrodes design followed by air drying overnight. To avoid MXene oxidation, cyclic voltammetry tests were performed at scan rates ranging from 2 to 100 mV s^{-1} in a potential window of 0 to 0.6 V.[17] Electrochemical impedance spectroscopy was performed at open-circuit potential, with a small sinusoidal amplitude of 5 mV, and frequencies of 10 mHz to 100 kHz. The areal and gravimetric capacitances were calculated for the printed devices.[77]

The CV curve was used to calculate the cell capacitance (C/A), according to the following equations:

$$C = \frac{\int I(V)dV}{\nu \Delta V}[F] \tag{5-1}$$

where $I(V)$ was the voltammetric discharge current (mA), ν is the scan rate (mV s^{-1}), and ΔV is the potential window (0.6 V).

The normalized areal (C/A) and gravimetric (C/G) capacitances were calculated based on the area (A, in cm^2 calculated as the total area of the device) and total weight of the printed devices. The normalized capacitances were calculated as follows:

$$C/A = \frac{C_{device}}{A} \tag{5-2}$$

and

$$C/G = \frac{C_{device}}{g} \tag{5-3}$$

The power and energy densities of the devices were measured according to the following equations:

$$Energy\ Density\ (E) = \frac{\left((C/A) \times V^2\right)}{7200}[Wh\ cm^{-2}\ ] \tag{5-4}$$

$$Power\ Density\ (P) = \frac{3.6 \times E \times \upsilon}{V} [W\ cm^{-2}\ ] \quad (5\text{-}5)$$

where C/A [F cm^{-2}], V [V], and υ [mV s^{-1}] are as described above.

Results and Discussion

$Ti_3C_2T_x$ aqueous dispersion was prepared following a previously reported method (please see the Experimental Section for a detailed description of the MXene synthesis process and preparation of dispersions).[46] Briefly, $Ti_3C_2T_x$ was first synthesized by selective etching of Al atoms from Ti_3AlC_2 particles in a LiF and HCl aqueous mixture. The mixture was then washed with DI water until its pH dropped below 5. The product of this washing step was a dilute dispersion of single-layer $Ti_3C_2T_x$ sheets. Super-absorbing polymer balls were used to adjust the concentration of the dispersion to desired value according to our previously reported method.[14] Figure 5.1a shows an atomic force microscope image of representative single-layer $Ti_3C_2T_x$ sheets showing an average size of 0.8 μm for MXene sheets. To fabricate $Ti_3C_2T_x$ aerogels, droplets of the additive-free aqueous $Ti_3C_2T_x$ dispersion were generated using an inkjet head (see Figure A.2), and they were deposited onto a freezing substrate at -20°C (Figure 5.1a). Droplets are instantly frozen upon contact with the precooled substrate, preserving their shape. By adjusting the inter-droplet distance and time lapse between successive droplets, continuous lines were generated through the coalescence of separate droplets. Complex 3D architectures were printed through layer-by-layer deposition of lines. Once the 3D printing of the frozen structure is completed, a freeze-drying process was applied to remove the ice from the frozen bodies and achieve highly porous aerogels, as presented in Figure 5.1b. Figure A.1b shows a representative X-ray diffraction pattern of a fabricated 3DFP $Ti_3C_2T_x$ aerogel, confirming that there is no new phase formation during the 3DFP process.

Figure 5.1. a) Schematics of the 3DFP process used for the fabrication of 3D Ti_3C_2Tx aerogels. MXene ink is deposited in form of spherical droplets on to a freezing substrate. Partial melting caused by the freshly deposited ink (layer N+1) ensures a good bonding of successive layers. With the freezing of the deposited ink, ice crystals grow from bottom to top, resulting in a vertically aligned porosity and MXene flakes. b) Photograph showing the 3D printed MXene aerogels having various geometries with constant cross-sections. c) Photograph showing 3D printed ultralight aerogels standing on a flower. d) Photographs showing the steps of fabricating truly 3D MXene aerogels with overhang truss structures.

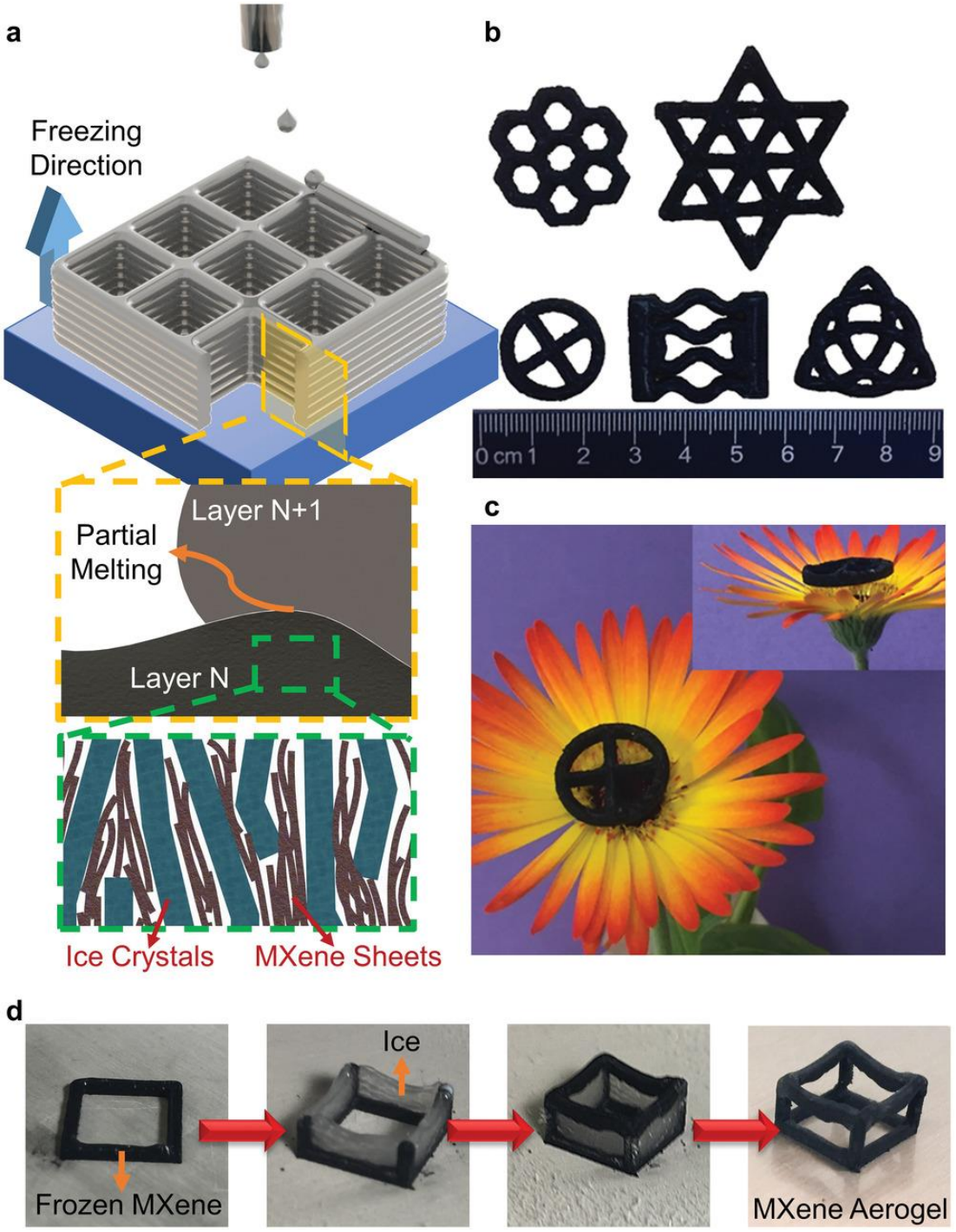

Since the frozen structures are composed of mostly DI water, after freeze-drying, obtained aerogels are light-weight with a density as low as 9.73 mg cm^{-3}. As it is presented in Figure 5.1c, 3DFP aerogels can stand on a flower without damaging its fibers

In extrusion-based 3D printing, the physical properties of the prints are negatively influenced by insufficient bonding at the interface of the deposited layers driven by intermolecular diffusion and the undesirable voids between the adjacent layers.[43] In 3DFP, deposited layer at room temperature ($N+1^{th}$ layer—Figure 5.1a) causes a partial melting on top of the previously deposited and frozen layer (N^{th} layer—Figure 5.1a). Since the ink's viscosity is low, it fills the possible voids between layers by the help of surface tension and gravitational forces. Finally, partially melted part of N^{th} layer fuses with the not yet frozen $N+1^{th}$ layer, and they both freeze together. This eliminates insufficient bonding, interfacial boundaries, and voids between layers and yields aerogels with continuous MXene walls as confirmed by the scanning electron microscopy (SEM) images (Figure 5.2a,b). Furthermore, as in the UFC method, deposited ink on top of the precooled substrate or already frozen layer uni-directionally freezes with ice crystals growing from the bottom to the top along the temperature gradient. This forces the MXene sheets to align vertically forming tightly packed walls between the ice crystals. After freeze-drying, MXene aerogels whose pore morphology is a replica of the ice crystals are obtained.

3D printed $Ti_3C_2T_x$-based aerogels have previously been fabricated by using extrusion-based 3D printing followed by freeze drying.[38–40] This 3D printing method is limited in printing truly 3D architectures as it is often difficult to print structures with overhang features or changing cross-sectional geometry without using harsh chemical or thermal post-processes.[47] Accordingly, the studies report the fabrication of MXene-based aerogels using extrusion-based 3D printed having a constant cross-sectional geometry, which limits the freedom in design.[38–40] The use of

sacrificial support materials that can be burned out after drying process is not practical for MXene due to its oxidation tendency.[48] However, in 3DFP process, ice can be used as the as support material to fabricate MXene aerogels with overhang structures (Figure 5.1d). As we also described in our previous works,[43,45,47] we employed a multi-nozzle 3D printing setup in which one nozzle was loaded with MXene ink and another nozzle was loaded with DI water as support material. The pillars and trusses of the cube presented in Figure 1d have cross-sectional dimensions of 1 × 1 mm. The length of each truss and the height of each pillar are 10 and 5 mm, respectively. With the 3D printing setup used in this work, the minimum height and thickness of the pillars can be printed are 0.1 and 0.25 mm, respectively. The maximum values of the width and height of the pillars are limited by the build volume of the 3D printing setup (120 × 120 × 120 mm in our setup) provided that the thickness of each pillar is sufficiently large to support the load of the pillars. Also, as we presented in our previous work,[43] the number of the horizontal trusses as well as the number of ice supports between those can be further increased. After sublimation of the ice including the support material during the freeze-drying process truly 3D $Ti_3C_2T_x$ aerogels with overhang features were fabricated. Since 3DFP enables the fabrication of truly 3D MXene aerogels, we believe that this method may lead to new applications for 3D MXene aerogels in the future.

The micropore morphology of the aerogels fabricated through a freeze casting-based method depends on type, concentration, and average size of the solute in the initial suspension, type of the solvent and used additives, and rate of freezing (solidification).[49] For instance, Dash *et al.* showed that the decreasing rate of freezing results in larger average pore size.[50] Yan *et al.* showed that the solid loading of the initial suspension has a similar impact (e.g., decreasing solid loading resulting in larger average pore size) on the microstructure of the aerogel.[49] Zhang *et al.* showed how the pore morphology can be tuned by using additives in the initial suspension

formulation.[51] With a defined temperature gradient, as in UFC, the nucleation of the ice crystals occurs on the cooled surface and the ice crystals propagate along the temperature gradient. At the end of the freeze-drying process, an aligned pore morphology is obtained.[52] Since 3DFP is a UFC-based fabrication method, the microstructure of the 3DFP aerogels can be tuned using the tools available for UFC, such as solid loading of the ink, temperature of the freezing substrate, using additives in the ink formulation, etc.

The microstructure of aerogels fabricated using 3DFP was studied by SEM, confirming the alignment of the MXene sheets along the temperature gradient from the bottom to the top (Figure 5.2a–c). With the advantages provided by 3DFP method, void formation is eliminated between subsequent layers and continuous MXene walls all along the freezing direction is obtained (Figure 5.2a,b). The top surface (plane parallel to the freezing direction) of 3DFP MXene aerogels consists of a micropore morphology with randomly aligned lamellar structures (Figure 5.2d–f). Depositing the ink in a layer-by-layer fashion did not result in void or boundary formation between deposited layers, indicating the merging of subsequently printed layers into previously printed layers (Figure 5.2f). The effect of the dispersion concentration on the aerogel's morphology is presented in Figure 5.2g. With the increasing concentration (from 9 to 15 mg mL^{-1}), the porosity decreased, MXene walls became thicker, and the pore width between MXene walls became smaller. This can be related to the less available space for the ice crystals to nucleate and grow and is in good agreement with our previous study reporting the fabrication of MXene aerogels by UFC.[15] Changing the microstructure of the aerogels by increasing the concentration of MXene ink would affect mechanical and electrical properties of the fabricated electrodes as discussed below.

$Ti_3C_2T_x$ MXene aerogels and its composites fabricated by conventional methods have been studied as pressure sensors in several previous reports.[13,29,30,53] Using 3D printing to fabricate

Figure 5.2. a) SEM image showing the cross-sectional surface of the aerogels showing deposited layers upon previous one. b) High-magnification SEM image showing the layer interface without any voids and interlayer boundaries. c) High-magnification SEM image showing the layer with the aligned porosity along the freezing direction (from bottom to top). d) SEM image showing the top surface of the 3D freeze printed MXene aerogels. e) High magnification SEM image showing the random pore alignment on the plane perpendicular to freezing direction. f) High-magnification SEM image showing no visible boundary between grids deposited one after another. g) Images showing the top surface of 3DFP MXene aerogels fabricated from inks with a concentration of 9, 12, and 15 mg mL^{-1}.

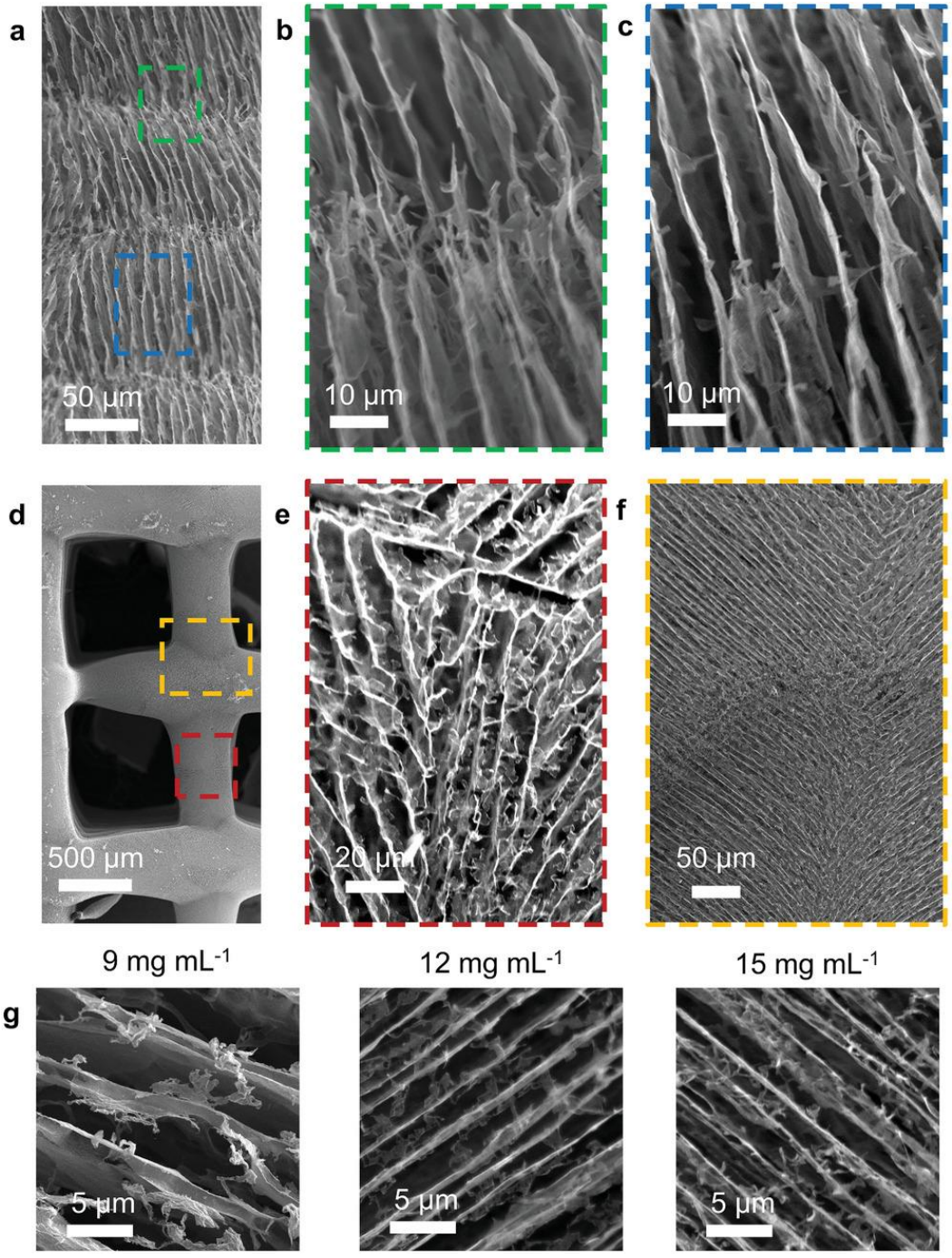

aerogels can provide flexibility in design and sensor geometry for different applications. To evaluate the performance of the 3DFP MXene aerogels for pressure sensing, we characterized their mechanical and electrical properties (Figure 5.3). For these tests, cubic aerogels (5 × 5 × 5 mm) were fabricated using 9, 12, and 15 mg mL^{-1} dispersions and their average densities were measured to be 9.73, 12.56, and 15.69 mg cm^{-3}, respectively. Mechanical properties of the aerogels were characterized by in-plane compression tests with up to 50% strain (Figure 5.3a). Three distinctive regimes were observed in the loading curves: a linear elastic region within 0–5% compressive strain, a plateau-like regime between 5% and 30% compressive strain, and a nonlinear elastic regime after 30% compressive strain. The maximum stresses at 50% strain were measured as 1.3, 2.25, and 4.04 kPa with the increasing density values. This trend was in good agreement with previously reported 3DFP aerogels[42,43] and freeze casted pristine $Ti_3C_2T_x$ aerogels.[15,22]

The mechanical response of the 15.69 mg cm^{-3} aerogel, which provided the highest stress response at 50% compressive strain value, was further studied using five-stepped compressive loading–unloading strains up to 50% strain with 10% increments (Figure 5.3b). The results indicate that the succeeding stress–strain curves almost rise back to the stress level measured at the maximum strain value of the previous cycle. This trend was repeated for all increment values indicating an excellent strain memory effect.[54] Multicycle compression test further revealed the great resilience of the 3DFP MXene aerogels. 3D freeze printed specimens were compressed for 50 cycles up to 10% strain to further investigate the mechanical robustness of the structure (Figure 5.3c). The second loading–unloading curve exhibited a stress degradation less than 3%, meaning that the 3DFP MXene aerogels maintain their original elasticity and structural robustness. After 15 loops, the stress response at 10% strain was stabilized at ≈0.87 kPa (Figure A.4), which corresponds to an 11.2% stress decay.

Figure 5.3. Mechanical and electrical properties of 3DFP MXene aerogels. a) Stress–strain plots of the aerogels having different densities after uniaxial compression tests up to 50% compressive strain. b) Stress–strain curves of multicycle compression by increasing strain amplitude of printed MXene aerogels (ρ = 15.69 mg cm^{-3}). c) Stress–strain curves for 50 loading–unloading cycles up to 10% strain (ρ = 15.69 mg cm^{-3}). d) $I-V$ curves of $Ti_3C_2T_x$ aerogels with different densities parallel to freezing direction. e) I–V curves of $Ti_3C_2T_x$ aerogels with different densities perpendicular to freezing direction. The arrows in the inset of both (d) and (e) indicate the freezing direction. f) Response in the aerogels resistance to a compression with 10% strain for 10 consecutive cycles (ρ = 15.69 mg cm^{-3}). g) 3D freeze printed MXene aerogels infiltrated in PDMS elastomer. h) Response in the resistance of the 3D freeze printed aerogels infiltrated in PDMS after applying 10% tension.

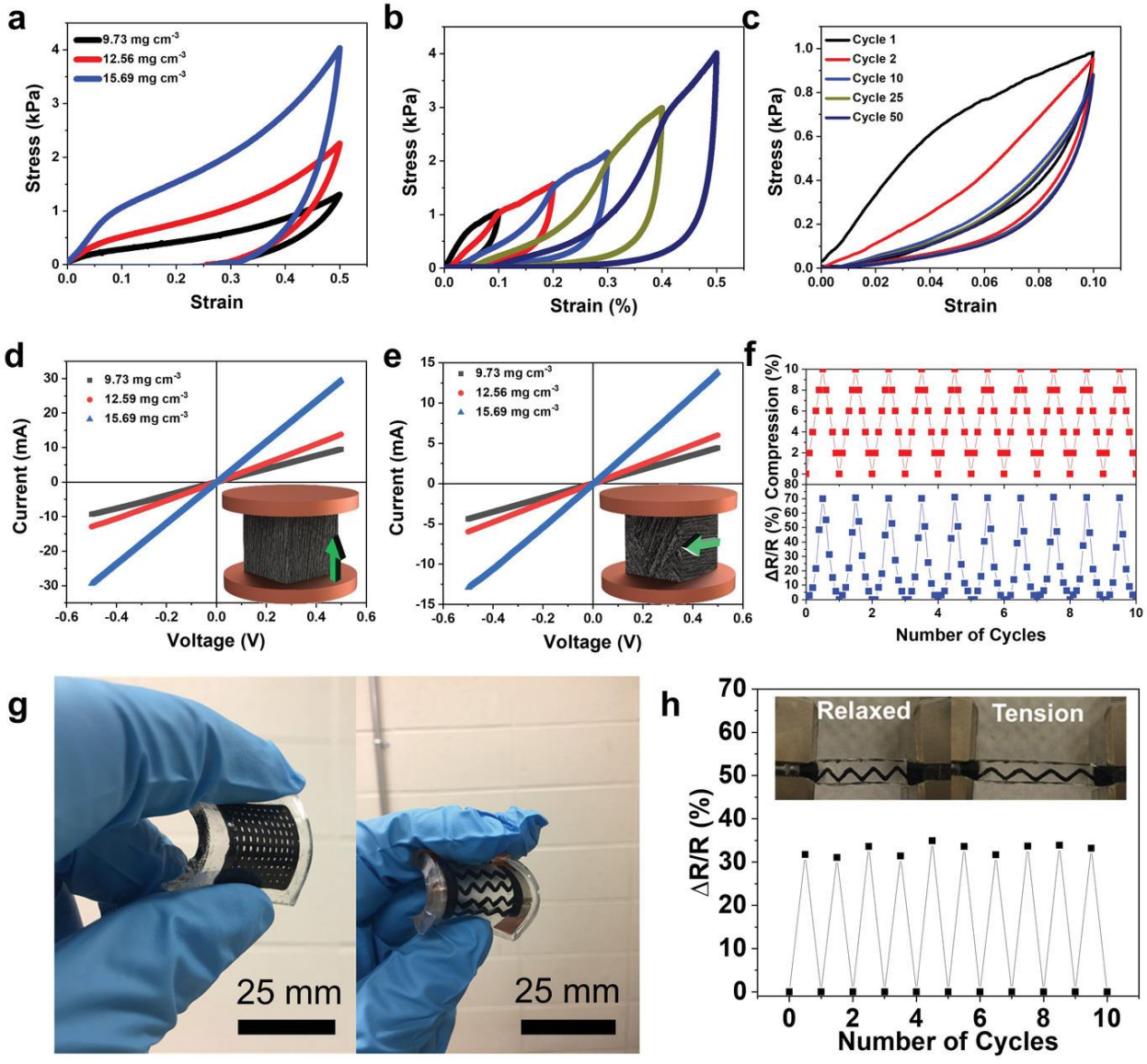

The electrical conductivity of the fabricated cubic specimens as a function of their density was investigated using current (I)–voltage (V) curves. In Figure 5.3d,e, the MXene aerogels were

placed between two copper electrodes so that the freezing direction is parallel and perpendicular to the testing direction, respectively. The current responses of all specimens in all directions present a linear relationship with the changing voltage, following Ohm's law. Since the microstructural features of the aerogels, such as the thickness of MXene walls or the distance between the walls, have a great dependency on the density of aerogels, the resistance of the specimens increased with decreasing density due to the presence of more space and less inter-sheet junctions in the microstructure. A similar behavior was also observed in our previous study reporting $Ti_3C_2T_x$ aerogels fabricated through the UFC method.[15] 3DFP MXene aerogels in parallel configuration (measurement in the direction of freezing) exhibited high electrical conductivity values: 3.78, 5.35, and 11.8 S m^{-1} at densities of 9.73, 12.56, and 15.69 mg cm^{-3}, respectively (Figure 5.3d). When the freezing direction of the aerogels are perpendicular to the copper plates (measurement in the direction perpendicular to freezing), the conductivity of the samples reduced to 1.76, 2.40, and 5.35 S m^{-1} for 9.73, 12.56, and 15.69 mg cm^{-3} samples, respectively. This anisotropy in the electrical conductivity of the 3D freeze printed aerogels due to unidirectional freezing is in good agreement with the previous reports.[27]

To further characterize the piezoresistive behavior of the 3DFP aerogels, in situ resistance measurement was employed over 10 cycles of mechanical compression up to 10% strain value. Electrical resistance of the fabricated aerogels is highly stable over multiple cycles, indicating a significant structural resilience (Figure 5.3f).[55] Inspired by the work of Wang *et al.*,[56] 3DFP MXene aerogels were infiltrated in poly(dimethylsiloxane) (PDMS) elastomer to provide improved performance for real world applications such as wearable electronics. As seen in Figure 5.3g, we printed MXene aerogels where the user can control the shape and dimensions of the inner features. After infiltration of the PDMS into the pores of the MXene aerogels and curing, we have

Figure 5.4. Electrochemical performance of 3DFP MXene-based MSC. a) CV at different scan rate for MSC-2H-1V. b,c) CV curves at 10 mV s^{-1} and areal capacitance of different 3DFP MSC devices. d) Gravimetric capacitance of MXene-based MSC compared with different MXene-based film with different thicknesses and sheets alignment. e) Nyquist plots for different MXene MSCs taken at 0 V versus the open-circuit potential. The inset shows the Nyquist plots of the MSC-5H and MSC-1H-5V. f) Ragone plots of the 3DFP $Ti_3C_2T_x$-based MSCs together with other reported values for comparison.

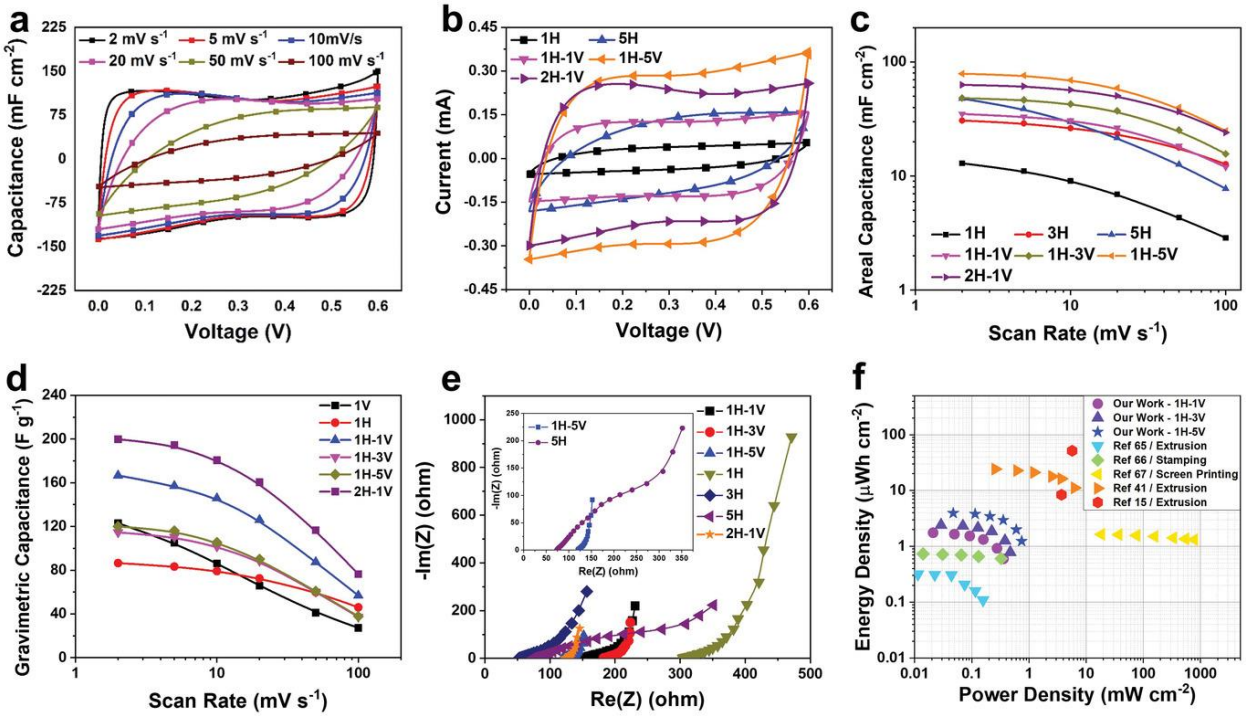

obtained flexible composites with a conductive MXene network, whose shape and dimensions can be customized for various needs. MXene/PDMS composites showed a great elasticity and a stable response in the electrical resistance (≈30% change in the resistance) with the applied tension (10% strain) for 10 consecutive cycles (Figure 5.3h).

In order to demonstrate the potential of 3DFP MXene aerogels for energy storage application, interdigitated $Ti_3C_2T_x$ electrodes were printed (using 15 mg mL^{-1} dispersion) on various substrates (including paper, acetate film, acrylic sheet, and glass slide), and their performance as all-solid state MSCs were investigated (Figure A.5). Due to the nature of the 3DFP process, fabricated interdigitated electrodes possessed a highly ordered porous morphology with vertically aligned MXene sheets. The ordered and vertically aligned microstructure of the printed

electrodes leads to their enhanced electrical and ionic conductivities, improving the capacitance and rate handling capability of the printed devices.[35,57] However, due to the anisotropic microstructure of the MXene aerogels, the electrical conductivity is also anisotropic as discussed above (Figure 5.3d,e). Considering the geometry of the fabricated MSCs, in-plane electrical conductivity (x–y plane) is expected to be much lower than out-of-plane (y–z or x–z planes) due to the vertical alignment of the MXene sheets (

Figure A.8). Cuna *et al.* have previously showed that the electrical conductivity as well as specific capacitance of electrodes having an anisotropic porosity is highly dependent on the testing direction.[58] To address this issue and increase the electrical conductivity in x–y plane, we added a current collector layer to the electrode design. To achieve that, the same 3D printing setup was employed while the substrate was kept at ambient temperature. We first performed inkjet-based printing of a current collector layer and let it dry in ambient conditions to obtain MXene film with horizontally aligned sheets. Following, the temperature of the substrate was reduced to the desired value and 3DFP was performed to achieve porous electrodes standing on the current collector layer (Figure A.9). The resulting MSCs had a hybrid alignment of MXene sheets: the current collector with horizontally aligned sheets followed by the porous electrode with vertically aligned MXene sheets (Figure A.10). The current collector layer with horizontally aligned MXene sheets provided superior electrical conductivity along x–y plane (Figure A.8) whereas the porous electrode with vertically aligned MXene sheets provided an improved ionic diffusion and electrical conductivity in z direction. As previously reported by Peng *et al.*,[59] all-MXene MSCs exhibit a much lower contact resistance, higher capacitances, and better rate capabilities compared to MXene MSCs with platinum current collectors.

To evaluate the performance of fabricated MXene-based MSCs and study the effect of MXene sheets alignment on the electrochemical performance, 3D devices with horizontal, vertical, and mixed alignment of the MXene sheet were fabricated. The fabricated devices were labeled based on the number of printed layers as MSC-XH-YV, where X and Y represent the number of printed layers with horizontal (H, air dried) and vertical (V, freeze printed/dried) sheet alignment, respectively (e.g., MSC-1H-3V consists of one layer of air dried and three layers of freeze printed structure). The CV curves of the MSC-2H-1V device at different scan rates show an ideal capacitive behavior with a quasi-rectangular shape as presented in Figure 5.4a. To test the flexibility of the MSC devices, the effect of bending on their electrochemical performance of the MSC-3V devices printed on paper substrate was investigated (Figure A.11). CV curves at 50 mV s^{-1} and electrochemical impedance spectroscopy (EIS) tests results at different bending angles (60°, 120°, and 180°) are presented inFigure A.11. The flexibility of the printed devices is demonstrated by the capacitance, and series resistance (Rs) of the MSC not changing significantly with changing the bending angle. MSCs with different current collector–electrode layer combinations showed similar CV curve shapes at different scan rate (Figure 5.4b;

Figure A.12, CV at 10 mV s^{-1}). The specific capacitance of the devices with different number of printed layers at different scan rates is presented in Figure 5.4c. As expected, increasing the load of active material per area results in a higher areal capacitance. The MCS-1H, MCS-1H-1V, MCS-1H-3V, MCS-1H-5V, and MCS-2H-1V devices showed high areal capacitance of 13, 35, 48.2, 79, and 63 mF cm^{-2}, respectively (Figure 5.4c). The results indicate that designing electrode structure through changing the MXene sheets orientation significantly affect electrochemical performances.[12] Comparing the electrochemical properties of MSC-1V (superior capacitive performance at higher scan rates) and MSC-1H (superior capacitive performance at

lower scan rates) helps to better understand the influence of sheet alignment (Figure 5.4d). At low scan rates ionic transfer is the dominant factor on the electrochemical performance, while at high scan rates the role of electron transfer is dominant. The results show that MSC-1H has better electron transfer properties (in agreement with aforementioned electrical conductivity results), while for the MSC-1V ionic transfer is enhanced. MSC-2H-1V showed high gravimetric capacitance of ≈200 F g^{-1} at 2 mV s^{-1} due to its improved ionic and electronic transfer properties. In addition, increasing the electrode thickness from 626 to ≈925 μm for MSC-1H-3V and MSC-1H-5V did not affect the gravimetric capacitive behavior of the devices, indicating the thickness independent-behavior. The freeze printed MSCs surpasses some of the best gravimetric capacitive performances reported in literature (Table A.1).[57,60–70] This behavior can be related to the increased amount of accessible MXene surface area in the vertically aligned structure and enhanced electrical conductivity due to the horizontally aligned sheets in the current collector layer.

As previously discussed by Yang *et al.*, vertical alignment of the MXene sheets may reduce their restacking while preserving a high porosity in the structure resulting in a highly ion accessible the electrodes.[35] Directional ion transport, parallel to the direction of sheets, also leads to a thickness independent behavior of the electrodes.[57] On the other hand, the horizontally aligned current collector layer provides enhanced electrical conductivity due to its closely packed MXene sheets that are oriented in direction of electron flow from the device electrical connection to the interdigital electrodes.[71] The advantage of the dual alignment of the sheet on the charge storage properties of MSCs is schematically presented in Figure A.13. Once ion reaches the surface MXene sheets, the charge is stored by the reversible protonation of surface functional groups. In a simplified view, the overall charge– discharge process can be expressed as[72]:

$$Ti_3C_2O_x(OH)_yF_z + H^+ + SO_4^{2-}$$

$$\rightleftharpoons [Ti_3C_2O_x(OH)_yF_z]^- // H^+ + [Ti_3C_2O_x(OH)_yF_z]^+ // SO_4^{2-} \qquad (5\text{-}6)$$

where H^+ and SO_4^{2-} are the cation and the anion present in the PVA/H_2SO_4 electrolyte.

The fabricated devices showed excellent cyclability, retaining ≈94% of their capacitance after 10 000 cycles (Figure A.14). It is worth highlighting the importance of the horizontally aligned layers (the current collector) in device integrity and physical stability. The vertically aligned MXene sheets did not have a good attachment to the substrate.

To compare the maximum areal capacitance value of the 3DFP MSC-1H-5V (79 mF cm^{-2}), we prepared the plot given inFigure A.15. This compares the maximum areal capacitance values reported for interdigitated electrode structures fabricated from solely MXene inks. It shows that 3DFP results in a higher areal capacitance by keeping the initial ink concentration the same when compared to other fabrication methods.

EIS test was employed to further study the charge transfer and ion transport in the 3DFP MSCs with their porous and well aligned architecture. As presented in Figure 5.4e and Figure A.16 Rs was decreased from ≈550 Ω cm^{-2} for MSC-1V to ≈300 Ω cm^{-2} for MSC-1H to ≈150 Ω cm^{-2} for MSC-1H-1V, and to ≈120 Ω cm^{-2} for MSC- 2H-1V with MXene sheets working as current collector, indicating the importance of horizontally aligned layers. The EIS results of MSC-5H and MSC-1H-5V are presented in inset of Figure 5.4e. While the MSC-5H showed lower Rs, the MSC-1H-5V showed improved ionic transfer confirmed by higher slope of the Nyquist plot in the low frequency regime.[57,60] This originated from the vertical versus horizontal alignment of the MXene sheets. The vertically aligned MXene sheets possess faster ion transport compared with horizontally aligned electrodes due to their well aligned porous structure, which is a key element

for thickness-independent performance. It is worth mentioning the lack of noticeable semicircle in high frequency region, indicating low charge transfer resistance for all the tested samples. These results are in line with the morphological studies of the electrodes confirming the formation of a well aligned porous structure for MSC fabricated with 3DPF process.

The Ragone plot (Figure 5.4f) further showcases the potential of 3DFP MXene interdigitated electrodes for high energy density and power density supercapacitors.[14,39,73–75] At a scan rate of 50 mV s^{-1}, the MSC-1H-5V exhibits an energy density of 2 µWh cm^{-2} and a power density of 0.6 mW cm^{-2}. By decreasing scan rate to 2 mV s^{-1}, the energy density increases to 3.9 µWh cm^{-2} while the power density decreases to 0.05 mW cm^{-2}. The 3DFP, $Ti_3C_2T_x$based MSCs exhibit almost ten orders of magnitude higher energy density with comparable power densities to other reported MSC devices with similar power density values. The electrochemical performances indicate that designing electrode structure through changing the MXene sheets orientation significantly affects electrochemical performances.[12]

Conclusion

This study reports on fabrication of ultralight, multipurpose, and truly 3D MXene aerogel structures using 3DFP method. While simple, straightforward, and inexpensive, the proposed fabrication method provides a great deal of customizability to engineer the micro- and macrostructure of the fabricated electrodes. Employing this capability and study electrodes properties with different microstructure provided a better insight into structure–property relationship. The mechanical compression tests showed that the aerogels' mechanical properties can be tuned simply by controlling the ink concentration. The excellent stability of the electrical conductivity over multiple compression cycles revealed excellent structural resilience of the fabricated aerogels. The all-MXene based 3DFP MSCs with various sheets alignment showed

improved capacitive and rate capability responses and confirmed the importance of engineering microstructure and its effect on electrochemical performances. The engineered MSCs with hybrid MXene sheets orientation showed thickness independent capacitive behavior. The proposed fabrication method can be employed to fabricate various devices with enhanced performances in applications such as flexible electronics, sensors, and energy storage.

References

[1] Naguib, M., M. Kurtoglu, V. Presser, J. Lu, J. Niu, M. Heon, L. Hultman, Y. Gogotsi, and M.W. Barsoum, Two-dimensional nanocrystals produced by exfoliation of Ti3AlC2. Advanced materials, 2011. 23(37): p. 4248-4253.

[2] Naguib, M., V.N. Mochalin, M.W. Barsoum, and Y. Gogotsi, 25th anniversary article: MXenes: a new family of two-dimensional materials. Advanced materials, 2014. 26(7): p. 992-1005.

[3] Naguib, M., O. Mashtalir, J. Carle, V. Presser, J. Lu, L. Hultman, Y. Gogotsi, and M.W. Barsoum, Two-dimensional transition metal carbides. ACS nano, 2012. 6(2): p. 1322-1331.

[4] Anasori, B., M.R. Lukatskaya, and Y. Gogotsi, 2D metal carbides and nitrides (MXenes) for energy storage. Nature Reviews Materials, 2017. 2(2): p. 1-17.

[5] Naguib, M., J. Come, B. Dyatkin, V. Presser, P.-L. Taberna, P. Simon, M.W. Barsoum, and Y. Gogotsi, MXene: a promising transition metal carbide anode for lithium-ion batteries. Electrochemistry Communications, 2012. 16(1): p. 61-64.

[6] Anasori, B., Y. Xie, M. Beidaghi, J. Lu, B.C. Hosler, L. Hultman, P.R. Kent, Y. Gogotsi, and M.W. Barsoum, Two-dimensional, ordered, double transition metals carbides (MXenes). ACS nano, 2015. 9(10): p. 9507-9516.

[7] Halim, J., S. Kota, M.R. Lukatskaya, M. Naguib, M.Q. Zhao, E.J. Moon, J. Pitock, J. Nanda, S.J. May, and Y. Gogotsi, Synthesis and characterization of 2D molybdenum carbide (MXene). Advanced Functional Materials, 2016. 26(18): p. 3118-3127.

[8] Wang, X., S. Kajiyama, H. Iinuma, E. Hosono, S. Oro, I. Moriguchi, M. Okubo, and A. Yamada, Pseudocapacitance of MXene nanosheets for high-power sodium-ion hybrid capacitors. Nature communications, 2015. 6(1): p. 1-6.

[9] Lei, J.-C., X. Zhang, and Z. Zhou, Recent advances in MXene: Preparation, properties, and applications. Frontiers of Physics, 2015. 10(3): p. 276-286.

[10] Er, D., J. Li, M. Naguib, Y. Gogotsi, and V.B. Shenoy, Ti3C2 MXene as a high capacity electrode material for metal (Li, Na, K, Ca) ion batteries. ACS applied materials & interfaces, 2014. 6(14): p. 11173-11179.

[11] Shang, T., Z. Lin, C. Qi, X. Liu, P. Li, Y. Tao, Z. Wu, D. Li, P. Simon, and Q.H. Yang, 3D macroscopic architectures from self-assembled MXene hydrogels. Advanced Functional Materials, 2019. 29(33): p. 1903960.

[12] Orangi, J. and M. Beidaghi, A review of the effects of electrode fabrication and assembly processes on the structure and electrochemical performance of 2D MXenes. Advanced Functional Materials, 2020. 30(47): p. 2005305.

[13] Liu, J., H.B. Zhang, X. Xie, R. Yang, Z. Liu, Y. Liu, and Z.Z. Yu, Multifunctional, superelastic, and lightweight MXene/polyimide aerogels. Small, 2018. 14(45): p. 1802479.

[14] Orangi, J., F. Hamade, V.A. Davis, and M. Beidaghi, 3D printing of additive-free 2D Ti3C2T x (MXene) ink for fabrication of micro-supercapacitors with ultra-high energy densities. ACS nano, 2019. 14(1): p. 640-650.

[15] Orangi, J., H. Tetik, P. Parandoush, E. Kayali, D. Lin, and M. Beidaghi, Conductive and highly compressible MXene aerogels with ordered microstructures as high-capacity electrodes for Li-ion capacitors. Materials Today Advances, 2021. 9: p. 100135.

[16] Hantanasirisakul, K., M. Alhabeb, A. Lipatov, K. Maleski, B. Anasori, P. Salles, C. Ieosakulrat, P. Pakawatpanurut, A. Sinitskii, and S.J. May, Effects of synthesis and processing on optoelectronic properties of titanium carbonitride MXene. Chemistry of Materials, 2019. 31(8): p. 2941-2951.

[17] Song, J., X. Guo, J. Zhang, Y. Chen, C. Zhang, L. Luo, F. Wang, and G. Wang, Rational design of free-standing 3D porous MXene/rGO hybrid aerogels as polysulfide reservoirs for high-energy lithium–sulfur batteries. Journal of Materials Chemistry A, 2019. 7(11): p. 6507-6513.

[18] Li, L., M. Zhang, X. Zhang, and Z. Zhang, New Ti3C2 aerogel as promising negative electrode materials for asymmetric supercapacitors. Journal of power Sources, 2017. 364: p. 234-241.

[19] Wang, Q., S. Wang, X. Guo, L. Ruan, N. Wei, Y. Ma, J. Li, M. Wang, W. Li, and W. Zeng, Mxene-reduced graphene oxide aerogel for aqueous zinc-ion hybrid supercapacitor with ultralong cycle life. Advanced Electronic Materials, 2019. 5(12): p. 1900537.

[20] Zhang, X., R. Lv, A. Wang, W. Guo, X. Liu, and J. Luo, MXene aerogel scaffolds for high-rate lithium metal anodes. Angewandte Chemie, 2018. 130(46): p. 15248-15253.

[21] Zhao, S., H.-B. Zhang, J.-Q. Luo, Q.-W. Wang, B. Xu, S. Hong, and Z.-Z. Yu, Highly electrically conductive three-dimensional Ti3C2T x MXene/reduced graphene oxide hybrid aerogels with excellent electromagnetic interference shielding performances. Acs Nano, 2018. 12(11): p. 11193-11202.

[22] Han, M., X. Yin, K. Hantanasirisakul, X. Li, A. Iqbal, C.B. Hatter, B. Anasori, C.M. Koo, T. Torita, and Y. Soda, Anisotropic MXene aerogels with a mechanically tunable ratio of electromagnetic wave reflection to absorption. Advanced Optical Materials, 2019. 7(10): p. 1900267.

[23] Sambyal, P., A. Iqbal, J. Hong, H. Kim, M.-K. Kim, S.M. Hong, M. Han, Y. Gogotsi, and C.M. Koo, Ultralight and mechanically robust Ti3C2T x hybrid aerogel reinforced by carbon nanotubes for electromagnetic interference shielding. ACS Applied Materials & Interfaces, 2019. 11(41): p. 38046-38054.

[24] Wu, X., B. Han, H.-B. Zhang, X. Xie, T. Tu, Y. Zhang, Y. Dai, R. Yang, and Z.-Z. Yu, Compressible, durable and conductive polydimethylsiloxane-coated MXene foams for high-performance electromagnetic interference shielding. Chemical Engineering Journal, 2020. 381: p. 122622.

[25] Zeng, Z., C. Wang, G. Siqueira, D. Han, A. Huch, S. Abdolhosseinzadeh, J. Heier, F. Nüesch, C. Zhang, and G. Nyström, Nanocellulose-MXene biomimetic aerogels with orientation-tunable electromagnetic interference shielding performance. Advanced Science, 2020. 7(15): p. 2000979.

[26] Bian, R., G. He, W. Zhi, S. Xiang, T. Wang, and D. Cai, Ultralight MXene-based aerogels with high electromagnetic interference shielding performance. Journal of Materials Chemistry C, 2019. 7(3): p. 474-478.

[27] Yang, M., Y. Yuan, Y. Li, X. Sun, S. Wang, L. Liang, Y. Ning, J. Li, W. Yin, and Y. Li, Anisotropic Electromagnetic Absorption of Aligned Ti3C2T x MXene/Gelatin Nanocomposite Aerogels. ACS Applied Materials & Interfaces, 2020. 12(29): p. 33128-33138.

[28] Bi, L., Z. Yang, L. Chen, Z. Wu, and C. Ye, Compressible AgNWs/Ti 3 C 2 T x MXene aerogel-based highly sensitive piezoresistive pressure sensor as versatile electronic skins. Journal of Materials Chemistry A, 2020. 8(38): p. 20030-20036.

[29] Wang, L., M. Zhang, B. Yang, J. Tan, and X. Ding, Highly compressible, thermally stable, light-weight, and robust aramid nanofibers/Ti3AlC2 MXene composite aerogel for sensitive pressure sensor. ACS nano, 2020. 14(8): p. 10633-10647.

[30] Hu, Y., H. Zhuo, Q. Luo, Y. Wu, R. Wen, Z. Chen, L. Liu, L. Zhong, X. Peng, and R. Sun, Biomass polymer-assisted fabrication of aerogels from MXenes with ultrahigh compression elasticity and pressure sensitivity. Journal of Materials Chemistry A, 2019. 7(17): p. 10273-10281.

[31] Cai, C., Z. Wei, Y. Huang, and Y. Fu, Wood-inspired superelastic MXene aerogels with superior photothermal conversion and durable superhydrophobicity for clean-up of super-viscous crude oil. Chemical Engineering Journal, 2021. 421: p. 127772.

[32] Lin, P., J. Xie, Y. He, X. Lu, W. Li, J. Fang, S. Yan, L. Zhang, X. Sheng, and Y. Chen, MXene aerogel-based phase change materials toward solar energy conversion. Solar Energy Materials and Solar Cells, 2020. 206: p. 110229.

[33] Wang, N.-N., H. Wang, Y.-Y. Wang, Y.-H. Wei, J.-Y. Si, A.C.Y. Yuen, J.-S. Xie, B. Yu, S.-E. Zhu, and H.-D. Lu, Robust, lightweight, hydrophobic, and fire-retarded polyimide/MXene aerogels for effective oil/water separation. ACS applied materials & interfaces, 2019. 11(43): p. 40512-40523.

[34] Zhang, Q., G. Yi, Z. Fu, H. Yu, S. Chen, and X. Quan, Vertically aligned janus MXene-based aerogels for solar desalination with high efficiency and salt resistance. ACS nano, 2019. 13(11): p. 13196-13207.

[35] Wei, Z., T. Liu, L. Zhang, and J. Yu, Sulfide-based nickel-plated fabrics for foldable quasi-solid-state supercapacitors. Energy & Environmental Materials, 2021.

[36] Zhu, C., T. Liu, F. Qian, W. Chen, S. Chandrasekaran, B. Yao, Y. Song, E.B. Duoss, J.D. Kuntz, and C.M. Spadaccini, 3D printed functional nanomaterials for electrochemical energy storage. Nano Today, 2017. 15: p. 107-120.

[37] Chang, P., H. Mei, S. Zhou, K.G. Dassios, and L. Cheng, 3D printed electrochemical energy storage devices. Journal of Materials Chemistry A, 2019. 7(9): p. 4230-4258.

[38] Li, X., H. Li, X. Fan, X. Shi, and J. Liang, 3D-printed stretchable micro-supercapacitor with remarkable areal performance. Advanced Energy Materials, 2020. 10(14): p. 1903794.

[39] Yang, W., J. Yang, J.J. Byun, F.P. Moissinac, J. Xu, S.J. Haigh, M. Domingos, M.A. Bissett, R.A. Dryfe, and S. Barg, 3D printing of freestanding MXene architectures for current-collector-free supercapacitors. Advanced materials, 2019. 31(37): p. 1902725.

[40] Yu, L., W. Li, C. Wei, Q. Yang, Y. Shao, and J. Sun, 3D printing of NiCoP/Ti3C2 MXene architectures for energy storage devices with high areal and volumetric energy density. Nano-micro letters, 2020. 12(1): p. 1-13.

[41] Brown, E., P. Yan, H. Tekik, A. Elangovan, J. Wang, D. Lin, and J. Li, 3D printing of hybrid MoS2-graphene aerogels as highly porous electrode materials for sodium ion battery anodes. Materials & Design, 2019. 170: p. 107689.

[42] Yan, P., E. Brown, Q. Su, J. Li, J. Wang, C. Xu, C. Zhou, and D. Lin, 3D printing hierarchical silver nanowire aerogel with highly compressive resilience and tensile elongation through tunable poisson's ratio. Small, 2017. 13(38): p. 1701756.

[43] Zhang, Q., F. Zhang, S.P. Medarametla, H. Li, C. Zhou, and D. Lin, 3D printing of graphene aerogels. Small, 2016. 12(13): p. 1702-1708.

[44] Ma, C., R. Wang, H. Tetik, S. Gao, M. Wu, Z. Tang, D. Lin, D. Ding, and W. Wu, Hybrid nanomanufacturing of mixed-dimensional manganese oxide/graphene aerogel macroporous

hierarchy for ultralight efficient supercapacitor electrodes in self-powered ubiquitous nanosystems. Nano Energy, 2019. 66: p. 104124.

[45] Tetik, H., K. Zhao, N. Shah, and D. Lin, 3D freeze-printed cellulose-based aerogels: Obtaining truly 3D shapes, and functionalization with cross-linking and conductive additives. Journal of Manufacturing Processes, 2021. 68: p. 445-453.

[46] Ghidiu, M., M.R. Lukatskaya, M.-Q. Zhao, Y. Gogotsi, and M.W. Barsoum, Conductive two-dimensional titanium carbide 'clay'with high volumetric capacitance. Nature, 2014. 516(7529): p. 78-81.

[47] Tetik, H., G. Yang, W. Tan, A. Fong, S. Lei, J.N. Weker, and D. Lin, High speed in-situ X-ray imaging of 3D freeze printing of aerogels. Additive Manufacturing, 2020. 36: p. 101513.

[48] Zhang, J., N. Kong, D. Hegh, K.A.S. Usman, G. Guan, S. Qin, I. Jurewicz, W. Yang, and J.M. Razal, Freezing titanium carbide aqueous dispersions for ultra-long-term storage. ACS applied materials & interfaces, 2020. 12(30): p. 34032-34040.

[49] Yan, L., J. Wu, L. Zhang, X. Liu, K. Zhou, and B. Su, Pore structures and mechanical properties of porous titanium scaffolds by bidirectional freeze casting. Materials Science and Engineering: C, 2017. 75: p. 335-340.

[50] Dash, R., Y. Li, and A.J. Ragauskas, Cellulose nanowhisker foams by freeze casting. Carbohydrate polymers, 2012. 88(2): p. 789-792.

[51] Zhang, Y., K. Zuo, and Y.-P. Zeng, Effects of gelatin addition on the microstructure of freeze-cast porous hydroxyapatite ceramics. Ceramics International, 2009. 35(6): p. 2151-2154.

[52] Hu, L., C.-A. Wang, Y. Huang, C. Sun, S. Lu, and Z. Hu, Control of pore channel size during freeze casting of porous YSZ ceramics with unidirectionally aligned channels using different freezing temperatures. Journal of the European Ceramic Society, 2010. 30(16): p. 3389-3396.

[53] Ma, Y., Y. Yue, H. Zhang, F. Cheng, W. Zhao, J. Rao, S. Luo, J. Wang, X. Jiang, and Z. Liu, 3D synergistical MXene/reduced graphene oxide aerogel for a piezoresistive sensor. Acs Nano, 2018. 12(4): p. 3209-3216.

[54] Zhu, C., T. Han, E.B. Duoss, A.M. Golobic, J.D. Kuntz, C.M. Spadaccini, and M.A. Worsley, Highly compressible 3D periodic graphene aerogel microlattices. Nature communications, 2015. 6(1): p. 1-8.

[55] Qiu, L., J.Z. Liu, S.L. Chang, Y. Wu, and D. Li, Biomimetic superelastic graphene-based cellular monoliths. Nature communications, 2012. 3(1): p. 1-7.

[56] Wang, D., Y. Lin, D. Hu, P. Jiang, and X. Huang, Multifunctional 3D-MXene/PDMS nanocomposites for electrical, thermal and triboelectric applications. Composites Part A: Applied Science and Manufacturing, 2020. 130: p. 105754.

[57] Xia, Y., T.S. Mathis, M.-Q. Zhao, B. Anasori, A. Dang, Z. Zhou, H. Cho, Y. Gogotsi, and S. Yang, Thickness-independent capacitance of vertically aligned liquid-crystalline MXenes. Nature, 2018. 557(7705): p. 409-412.

[58] Cuna, A., N. Tancredi, J. Bussi, V. Barranco, T.A. Centeno, A. Quevedo, and J.M. Rojo, Biocarbon monoliths as supercapacitor electrodes: influence of wood anisotropy on their electrical and electrochemical properties. Journal of The Electrochemical Society, 2014. 161(12): p. A1806.

[59] Peng, Y.-Y., B. Akuzum, N. Kurra, M.-Q. Zhao, M. Alhabeb, B. Anasori, E.C. Kumbur, H.N. Alshareef, M.-D. Ger, and Y. Gogotsi, All-MXene (2D titanium carbide) solid-state microsupercapacitors for on-chip energy storage. Energy & Environmental Science, 2016. 9(9): p. 2847-2854.

[60] Lukatskaya, M.R., S. Kota, Z. Lin, M.-Q. Zhao, N. Shpigel, M.D. Levi, J. Halim, P.-L. Taberna, M.W. Barsoum, and P. Simon, Ultra-high-rate pseudocapacitive energy storage in two-dimensional transition metal carbides. Nature Energy, 2017. 2(8): p. 1-6.

[61] Bo, Z., W. Zhu, W. Ma, Z. Wen, X. Shuai, J. Chen, J. Yan, Z. Wang, K. Cen, and X. Feng, Vertically oriented graphene bridging active-layer/current-collector interface for ultrahigh rate supercapacitors. Advanced materials, 2013. 25(40): p. 5799-5806.

[62] Kurra, N., B. Ahmed, Y. Gogotsi, and H.N. Alshareef, MXene-on-paper coplanar microsupercapacitors. Advanced Energy Materials, 2016. 6(24): p. 1601372.

[63] Navarro-Suárez, A.M., K. Maleski, T. Makaryan, J. Yan, B. Anasori, and Y. Gogotsi, 2D titanium carbide/reduced graphene oxide heterostructures for supercapacitor applications. Batteries & Supercaps, 2018. 1(1): p. 33-38.

[64] Zhao, C., Q. Wang, H. Zhang, S. Passerini, and X. Qian, Two-dimensional titanium carbide/RGO composite for high-performance supercapacitors. ACS applied materials & interfaces, 2016. 8(24): p. 15661-15667.

[65] Yue, Y., N. Liu, Y. Ma, S. Wang, W. Liu, C. Luo, H. Zhang, F. Cheng, J. Rao, and X. Hu, Highly self-healable 3D microsupercapacitor with MXene–graphene composite aerogel. Acs Nano, 2018. 12(5): p. 4224-4232.

[66] Zhou, Z., W. Panatdasirisuk, T.S. Mathis, B. Anasori, C. Lu, X. Zhang, Z. Liao, Y. Gogotsi, and S. Yang, Layer-by-layer assembly of MXene and carbon nanotubes on electrospun polymer films for flexible energy storage. Nanoscale, 2018. 10(13): p. 6005-6013.

[67] Quain, E., T.S. Mathis, N. Kurra, K. Maleski, K.L. Van Aken, M. Alhabeb, H.N. Alshareef, and Y. Gogotsi, Direct writing of additive-free MXene-in-Water ink for electronics and energy storage. Advanced Materials Technologies, 2019. 4(1): p. 1800256.

[68] Yu, L., Z. Fan, Y. Shao, Z. Tian, J. Sun, and Z. Liu, Versatile N-doped MXene ink for printed electrochemical energy storage application. Advanced Energy Materials, 2019. 9(34): p. 1901839.

[69] Li, H., X. Li, J. Liang, and Y. Chen, Hydrous RuO2-decorated MXene coordinating with silver nanowire inks enabling fully printed micro-supercapacitors with extraordinary volumetric performance. Advanced Energy Materials, 2019. 9(15): p. 1803987.

[70] Zhao, J., Y. Zhang, Y. Huang, X. Zhao, Y. Shi, J. Qu, C. Yang, J. Xie, J. Wang, and L. Li, Duplex printing of all-in-one integrated electronic devices for temperature monitoring. Journal of Materials Chemistry A, 2019. 7(3): p. 972-978.

[71] Yoon, Y., K. Lee, S. Kwon, S. Seo, H. Yoo, S. Kim, Y. Shin, Y. Park, D. Kim, and J.-Y. Choi, Vertical alignments of graphene sheets spatially and densely piled for fast ion diffusion in compact supercapacitors. Acs Nano, 2014. 8(5): p. 4580-4590.

[72] Wang, G., L. Zhang, and J. Zhang, A review of electrode materials for electrochemical supercapacitors. Chemical Society Reviews, 2012. 41(2): p. 797-828.

[73] Zhang, C.J., L. McKeon, M.P. Kremer, S.-H. Park, O. Ronan, A. Seral-Ascaso, S. Barwich, C.Ó. Coileáin, N. McEvoy, and H.C. Nerl, Additive-free MXene inks and direct printing of micro-supercapacitors. Nature communications, 2019. 10(1): p. 1-9.

[74] Zhang, C., M.P. Kremer, A. Seral-Ascaso, S.H. Park, N. McEvoy, B. Anasori, Y. Gogotsi, and V. Nicolosi, Stamping of flexible, coplanar micro-supercapacitors using MXene inks. Advanced Functional Materials, 2018. 28(9): p. 1705506.

[75] Abdolhosseinzadeh, S., R. Schneider, A. Verma, J. Heier, F. Nüesch, and C. Zhang, Turning trash into treasure: additive free MXene sediment inks for screen-printed micro-supercapacitors. Advanced Materials, 2020. 32(17): p. 2000716.

[76] Tetik, H. and D. Lin. 3D Freeze Printing: Development of an Experimental Setup and Determination of 3D Printing Parameters. in International Manufacturing Science and Engineering Conference. 2020. American Society of Mechanical Engineers.

[77] Ling, Z., C.E. Ren, M.-Q. Zhao, J. Yang, J.M. Giammarco, J. Qiu, M.W. Barsoum, and Y. Gogotsi, Flexible and conductive MXene films and nanocomposites with high capacitance. Proceedings of the National Academy of Sciences, 2014. 111(47): p. 16676-16681.

Chapter 6 - Bioinspired Manufacturing of Aerogels with Precisely Manipulated Surface Microstructure[5]

Aerogels are highly porous materials whose porosity is achieved by replacing the liquid component of a wet gel with air.[1] Material properties of aerogels are directly affected by their micropore structures and use of a specific aerogel for a particular application requires precise control of its micro porosity.[2] For instance, the micropore structure of the aerogels can be tailored for best mechanical properties[3], piezo resistivity[4], thermal conductivity[5], absorption performance[6], optical transmittance[7,8], electromagnetic interference shielding efficiency[9], etc. Freeze casting, which is a widely utilized method for fabrication of aerogels and porous structures from a variety of materials, offers many different tools for tailoring the microstructure of the final product. Freeze casting parameters used for manipulating the microstructure of the final product have been deeply investigated and several review papers have been published.[10-13] Typically, freeze casting produces a homogeneous micropore morphology where micropore size is controlled through tuning the freeze casting parameters. However, applications like bone tissue engineering, controlled multidrug delivery, selective liquid absorption, and separating membranes may benefit from nonhomogeneous micropore morphologies, that is, having pores of varying sizes, those are located in specific, controlled regions of the aerogels. Fabricating aerogels with a controlled nonhomogeneous microstructure has always been a challenge. Furthermore, in the age of atomic

[5]Reprinted with permission from "Bioinspired Manufacturing of Aerogels with Precisely Manipulated Surface Microstructure through Controlled Local Temperature Gradients" by Halil Tetik, Dan Feng, Samuel W. Oxandale, Guang Yang, Keren Zhao, Katelyn Feist, Nasrullah Shah, and Yiliang Liao, Zayd C. Leseman, and Dong Lin, 2021. ACS Applied Materials & Interfaces, 13, 924-931. 2021 American Chemical Society

and close to atomic scale manufacturing[14,15], controlling the pore morphology of the aerogels with a micrometer resolution would be of the interest.

To address this issue, several researchers performed sequential freeze casting of multiple slurries to mimic the bone microstructure.[16,17] Since the increasing solid content of the slurry yields to pores with decreasing size, they performed a two-step freeze casting procedure using slurries with low and high solid loadings. Using this method, they achieved bone-like scaffolds with larger pores at the center surrounded by much smaller pores at the shell. Ogden *et al.* on the other hand, used an ultrasound-directed self-assembly method to achieve a control on the microstructure during the freeze casting process.[18] They used an ultrasound wave field to drive the nanoparticles in the slurry into a concentric ring pattern achieving alternating regions with low and high porosities. In another study, Yang *et al.* reported that surface wettability of the substrate used for freeze casting has a significant effect on micropore size.[19] They showed that performing freeze casting on a hydrophilic substrate leads to small pores, whereas a hydrophobic substrate results in large pores. They fabricated substrates with various wetting behaviors and were able to manipulate the microstructure of the freeze-casted aerogels. Even though these studies achieved non-monolithic microstructures with controlled size and location of the micropores, proposed processes are complex, and lack design possibilities, high resolution, and clear boundaries between different pore size regions.

Thermal conductivity of the substrates used in a unidirectional freeze casting process has a significant impact on the nucleation and growth of ice crystals during the freezing as well as the micropore morphology of the final product.[20] Herein, we benefited from this phenomenon and fabricated substrates with varying thermal conductivity patterns, which was achieved by fabricating patterned photoresist (PR) polymer features on a silicon (Si) wafer following a

lithography process. The difference in thermal conductivity between PR and Si yielded to non-monolithic microstructures on the surface of the aerogels with micropores whose size and location can be controlled by the user. We selected two common freeze-cast suspensions such as colloidal silica and graphene oxide (GO) as base materials to demonstrate our method as a general approach. Furthermore, by adjusting the temperature of the cold plate used in the freeze casting procedure, the average size of the pores at different regions can be tailored for different size requirements. Using the Si substrates with patterned PR features, we distinguished boundaries between the regions with small and large pores and achieved a resolution as low as ~50 μm. We further showed the possibility of 3D-printed aerogels with precisely controlled surface micropore morphologies. To the best of our knowledge, this is the first study to report aerogels with controlled micropore morphologies (e.g., pore size, shape, and location) precisely controlled by creating thermal conductivity patterns on the substrates. We believe our method can be further extended for controlling pore size and location in 3D, and can be beneficial for applications such as drug delivery, bone tissue engineering, photo catalysis, pollutant absorption from water, etc.

Experimental

Preparation of the PR Patterns on Si Wafer Substrates

For the substrates, we used 4-in.-diameter silicon wafers. To begin the process, AZ 4620 PR was spun onto the Si wafer, which was then soft-baked on a 110°C hot plate for 80 s with full contact. A second layer of AZ 4620 PR was then spun onto the wafer, followed by a 180 s soft-bake on a 115°C hot plate with full contact. The final thickness of the PR was approximately 24 μm. After applying the PR, it was patterned using photolithography. Using a patterned photomask, the wafer was exposed to a dose of 1742 $mJ \cdot cm^{-2}$. The pattern was then developed through submersion in AZ 400 K 1:4 for 300 s. The wafer was then placed in an oven at 200 °C to hard-

bake the PR pattern. After fabrication, resulting heights of the PR features were measured and found to be in the range of 15−19 μm.

Freeze Casting Procedure

For the freeze casting process, we used a commercially available colloidal silica suspension (Nyacol, DP9711) with a concentration of 30 wt. % and an average particle size of 20 nm. We prepared the GO suspension by adding graphene oxide powder (Cheaptubes Inc.) into DI water and using sonication for 30 min. The concentration of the GO suspension was set to 8 $mg \cdot mL^{-1}$. To obtain aerogels with spatially controlled porosity, we prepared the freeze casting setup described in Figure 6.1a. First, we prepared square polydimethylsiloxane (PDMS) (Dow Corning, Sylgard 184) walls to be used as bottomless molds for the freeze casting process according to the manufacturer's directions. Briefly, we first prepared 3D printed polylactic acid (PLA) molds using a commercially available fused deposition modeling type 3D printer to shape the PDMS molds. Then, we mixed the PDMS with curing agents of 10:1 weight ratio. The mixture was kept in a vacuum chamber for 30 min to remove gas bubbles. Finally, the mixture was poured inside the already prepared 3D printed PLA molds and cured for 24 h in ambient temperatures. To freeze-cast the suspensions, we poured the prepared suspension inside the PDMS wall structure placed on the PR-patterned Si wafer substrate, which was placed on top of a precooled cold plate (Instec, HCP204SG). We pushed the PDMS wall firmly from the top to ensure there was no leakage after pouring the suspensions. We left the suspensions at the target temperature for at least 30 min to ensure complete freezing. Frozen samples were moved to a −70°C freezer for further crystallization and then a subsequent freeze-drying was applied at −35°C and 0.02 mbar using a commercial freeze-dryer (Labconco, Freezone Triad).

FEA Simulations

We simplified the model with several assumptions. First, all materials were assumed to be homogeneous and isotropic, with thermal properties independent of temperature change. The PR stripes were assumed to have consistent width and gap distance, so the temperature distribution was uniform along the PR stripe direction. We simplified the model with the region covering three PR stripes as shown in Figure 6.2 to represent the repeated stripes. We ignored the effect of PDMS mold, since the size is much larger than the PR stripes. The aqueous slurry was represented as pure DI water since the concentration was very low. Because we were more interested in the temperature profile discrepancy between aqueous suspension−Si wafer interface and the aqueous suspension−PR patterns interface, rather than the exact transient temperature during the process, the simulation was at steady state. In addition, the initial temperature of water affected the freezing rate (i.e., Mpemba effect), the reason for which is still unclear. We ignored the phase change of DI water, because a phase-change problem requires an FEA solver with transient analysis or quasi-static iterations to update the physical properties. As discussed in previous assumptions, we were more interested in the trend of temperature-profile discrepancy between the two interfaces. The model was built in ABAQUS, following the sketch and dimensions as shown in Figure 6.2a. There were six parts in the model, including three PR patterns, Si wafer, a DI water region with refined meshes, and a DI water region with coarse meshes. Boundary conditions were chosen to satisfy right-hand side of equation 6-2:

1. There was no heat flux on $x = 0, X$ (i.e., Neumann boundary conditions $T(x = 0.y)_{,x} = 0, T(x = X.y)_{,x} = 0$).

2. The precooled cold plate offered a Dirichlet boundary condition to the bottom of the Si wafer with a constant temperature of −30 °C (i.e., $T(x, y = 0) = -30°C$).

3. The air on top of DI water provides a Neumann boundary condition by free convection with a 25 °C room temperature and a film coefficient of 5 $W\cdot(m^2\cdot K)^{-1}$ (i.e., $T(x, y = Y)_{,y} = h(T(x, y = Y) - T_{air})$, where h is the film coefficient and T_{air} is the room temperature).

We chose DC2D4 (a four-node, linear heat-transfer quadrilateral) element for all the parts. Since the simulation was at steady state, we only needed the heat conductivity of each material, which were 0.19 $W\cdot(m\cdot K)^{-1}$, 149 $W\cdot(m\cdot K)^{-1}$, and 0.58 $W\cdot(m\cdot K)^{-1}$ for PR, Si, and DI water, respectively. After our convergence study, we chose to use 65 elements for each PR pattern, 9,375 elements for Si wafer, 2,115 elements for the DI water region with refined meshes, and 3,290 elements for the DI water region with coarse meshes.

3D Freeze Printing Procedure

We used a similar inkjet-based 3D printing method that had been reported in other studies. Briefly, as a prepared GO suspension (5 $mg\cdot mL^{-1}$) was loaded inside a syringe barrel attached to a three-axis motion stage. A solenoid micro-dispensing device was used to generate droplets of GO suspension. Generated droplets were deposited on top of the precooled substrate. By controlling the inter-droplet distance and time lapse between droplets with the help of a three-axis motion stage, we 3D printed lines and complex structures after the coalescence of the droplets. Printed structures were freeze-dried using conditions provided for the freeze casting case.

Surface Characterization of the Fabricated Aerogels

Dried aerogels were investigated under SEM (FEI Versa3D Dual Beam) after sputter-coating the samples with a thin layer of gold (~10 nm). Obtained SEM images were used to investigate characteristics of the micropore morphology of the aerogels. To measure average pore size distribution, we used an image-processing software (ImageJ).

Results and Discussion

In the freeze casting method, thermal conductivity of the substrate has a tremendous effect on the cooling rate of the slurry, nucleation and growth of the ice crystals, and eventually the final microstructure.[20] To date, in all reported cases, substrates with uniform thermal conductivities were used. Here in this work, we prepared Si wafer substrates with patterned PR features that are deposited by photolithography. Using these substrates with patterned PR features, we performed unidirectional freeze casting procedures as schematically described in Figure 6.1a. Patterned PR features on the Si substrate were parallel stripes with a feature size (width) of λ. To test the effect of different stripe dimensions, we fabricated patterned PR features with varying λ values on Si substrates. The relatively low thermal conductivity ($0.19 W \cdot (m \cdot K)^{-1}$)[21] of the PR features compared to Si ($149 W \cdot (m \cdot K)^{-1}$) helped us to manipulate the temperature gradient above the PR and Si surfaces. To achieve a unidirectional freeze casting process, we poured the prepared aqueous suspensions into a PDMS wall structure, which was placed on top of the PR-featured Si substrate. At this stage, the poured suspension contained liquid water and homogeneously dispersed nanoparticles. Thereafter, the substrate was placed on top of a precooled cold plate, whose temperature was well below the freezing point of water and was used to manipulate the rate of freezing. Due to the difference in the thermal conductivities of those surfaces, nucleation and growth rate of the ice crystals differed and resulted in a variation in the ice crystal size. As schematically demonstrated in Figure 6.1b,c, due to a higher thermal conductivity of the Si substrate surface, we obtained fine-sized ice crystals. The size was much coarser on the PR feature surface where the thermal conductivity was much lower. Once the frozen structures were freeze-dried, we obtained a surface porosity that replicates the patterned PR features on the Si substrate (Figure 6.1d). Even though we only generated patterned PR features as parallel stripes to find the

Figure 6.1. Schematics of proposed process: (a) Si substrate with PR patterns placed on top of a cold plate. Aqueous suspension is poured into a PDMS mold placed on top of the Si substrate for freeze casting. (b) Before freezing, the aqueous suspension is composed of water and homogeneously dispersed nanoparticles. (c) Once the temperature of the cold plate is reduced, the freezing process is initiated on the top of the PR and Si surfaces. Due to the difference in thermal conductivity of both surfaces, the average size of the ice crystals varies. (d) After freeze-drying sublimates all the ice content, the porosity is obtained as a replica of the patterned PR features.

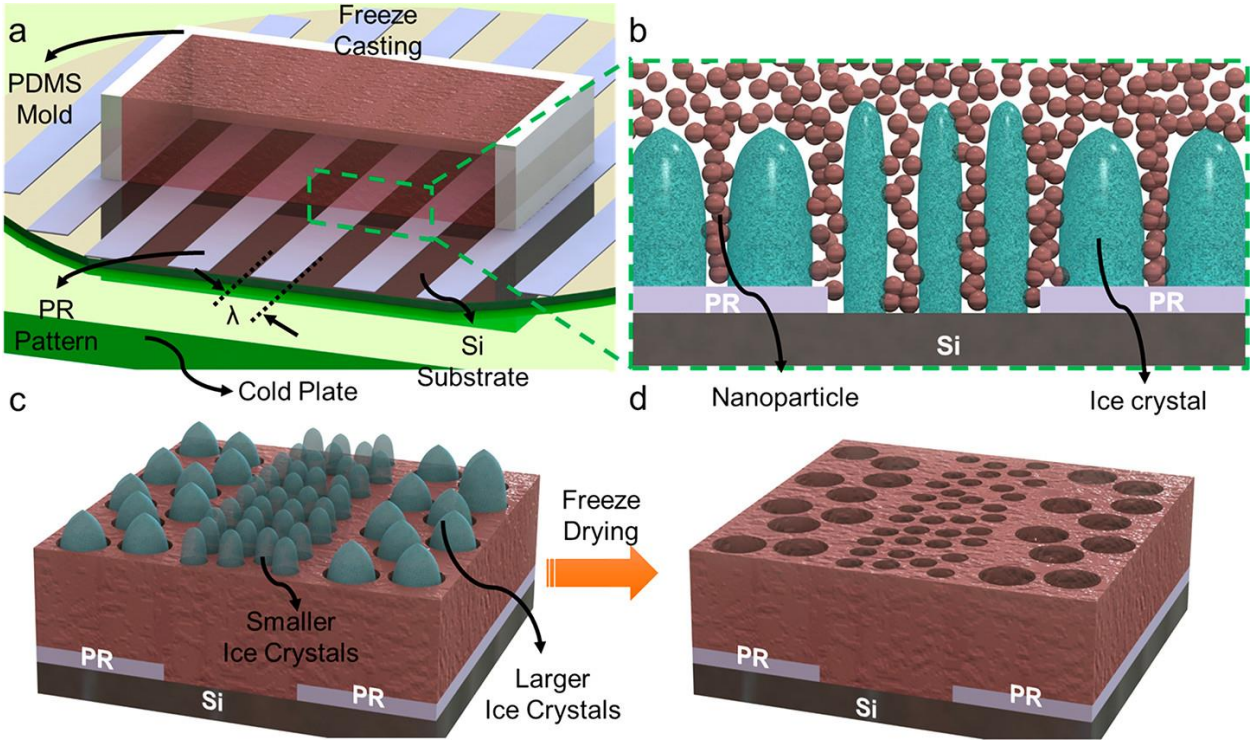

minimum resolution, it is also possible to deposit the PR polymer in a designed 2D shape, which will result in a micropore structure in a desired pattern.

To better illustrate how the unidirectional freeze casting using Si substrates with patterned PR features works, we used finite-element analysis (FEA) and simulated the temperature field around the aqueous suspension−Si wafer interface and the aqueous suspension−PR patterns interface. We used several assumptions for simplifying the model as explained in the experimental section. The geometry that covered three PR stripes as shown in Figure 6.2a was constructed to represent the repeated stripes in our simulations. We ignored the effect of the PDMS mold, since the size is much larger than the PR stripes and the aqueous suspension was represented as pure DI water because the concentration of slurries used was low (less than 1 wt. % for GO). Since there

is no body-heat flux on the model domain, the heat equation for the 2D model given in Figure 6.2a can be written as:

$$k\left(T(x,y)_{,xx} + T(x,y)_{,yy}\right) = 0 \tag{6-1}$$

where k is the heat conductivity, x and y are spatial coordinates, "," indicates a spatial derivative, and T is the temperature. Equation 1 can be rewritten to a weak form as:

$$\int_0^X \int_0^Y \left(k\delta T_{,x}T_{,x} + k\delta T_{,y}T_{,y}\right)dydx = \int_0^Y k\delta TT_{,x}dy\Big|_{x=0}^{x=X} + \int_0^X k\delta TT_{,y}dx\Big|_{y=0}^{y=Y} \tag{6-2}$$

After our simulations, we obtained the temperature profile in the neighborhood of Si, PR, and DI interfaces as presented in Figure 6.2b. As clearly seen there, we obtained a wavy temperature profile on the heights that is close to the substrate and patterned PR features. As the height is increasing, the temperature profile becomes more uniform. Due to the temperature profile reaching to equilibrium and becoming uniform after a certain height above the substrate, we only observed the patterned microstructure on the surface of the aerogels. However, we believe that by performing an optimization study for parameters such as the thermal conductivity values of the materials used, dimension of the patterns, and initial temperatures, we think the wavy temperature profile can be extended much above the substrate surface and can be used to tune the microstructure of the aerogels in 3D. To compare the temperature curves of PR−water and Si−water interfaces, we prepared the 2D temperature profile given in Figure 6.2c. Due to a lower thermal conductivity, the temperature of water at the PR−water interface is higher than that of the water at the same height above bare silicon. Therefore, the water above the PR freezes more slowly

Figure 6.2. a) The sketch, dimensions, and boundary conditions of a 2D model for FEA simulation. b) The 2D temperature profile in the neighborhood of Si, PR, and DI interfaces. c) The temperature curves of PR−water interface and Si−water interface. d) Temperature curves of PR−water interface with various λ values. e) 2D temperature profiles in the neighborhood of PR patterns with varying λ values.

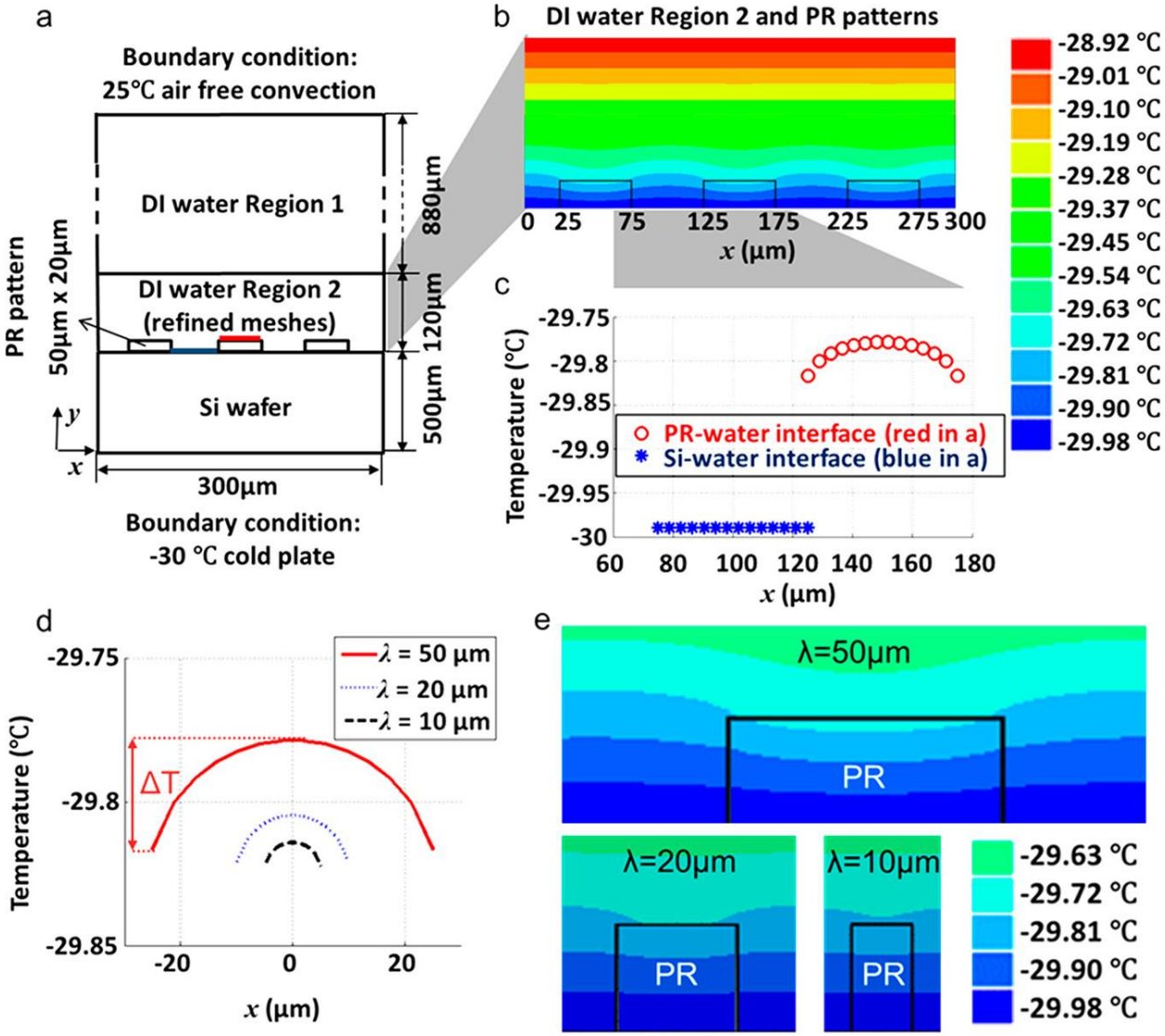

than the water at the same height above the Si surface and the water in contact with the Si wafer to freeze earlier and grow smaller ice crystals than water contacting PR patterns. As the above-mentioned simulations were performed for a feature size of λ = 50 μm, we also provided the simulation results for much smaller feature size values (λ = 20, and 10 μm) to see the effect of the feature size on the temperature profile above the patterned substrate. As given in Figure 6.2d, with

the decreasing λ values, the difference between the maximum and minimum temperature at the PR−water interface (ΔT) reduces. Furthermore, as presented in Figure 6.2e, wavy temperature profile in the vicinity of PR−water interface, which is the driving force for making distinct region of the different pore size, becomes flatter across the surface of the substrate. This change in the temperature profile obtained with the decreasing λ would make it harder to obtain a patterned microstructure as confirmed by the SEM images given in Figure 6.3 for λ = 9.68 and 19.01 μm cases.

We first investigated the fabricated Si substrates with and without PR patterned features, as presented in Figure 6.3a,d,g, using an optical microscope. Widths of the PR pattern features (λ) were measured as 48.64, 19.01, and 9.68 μm for a designed λ of 50, 20, and 10 μm, respectively, while the width of the gaps between PR stripes were measured as 52.24, 21.87, and 10.55 μm. For each λ value, a distinct boundary between the PR features and the Si surface was obtained and the height of each pattern was measured as approximately 20 μm. To understand how these features affect the microstructure of the fabricated aerogels, we freeze-casted colloidal silica suspension and investigated their microstructure as presented in Figure 6.3. In Figure 6.3b,c, we provided the control experiment where there was no PR feature on the Si substrate. As seen in the scanning electron microscope (SEM) images, the microstructure morphology was identical to common unidirectional freeze casting. When λ = 9.68 μm, we observed that patterned PR features had affected the freeze casting process and resulted in a patterned orientation in the pore morphology (Figure 6.3e,f). However, we did not observe any trace on controlled location of varying pore size. Even though the substrate having patterned PR features with λ = 19.01 μm showed some traces of location control on the pore size, the distinction between different-sized regions was not clear. Also, the width (λ) of the regions with different pore sizes did not match with the patterned PR

Figure 6.3. Optical microscope images showing the Si substrates with PR patterns and SEM images showing the effect of the PR pattern feature size on the microstructure of the freeze-casted silica; a–c) without PR pattern, d–f) λ = 9.68 μm, g–i) λ = 19.01 μm, and j–o) λ = 48.64 μm.

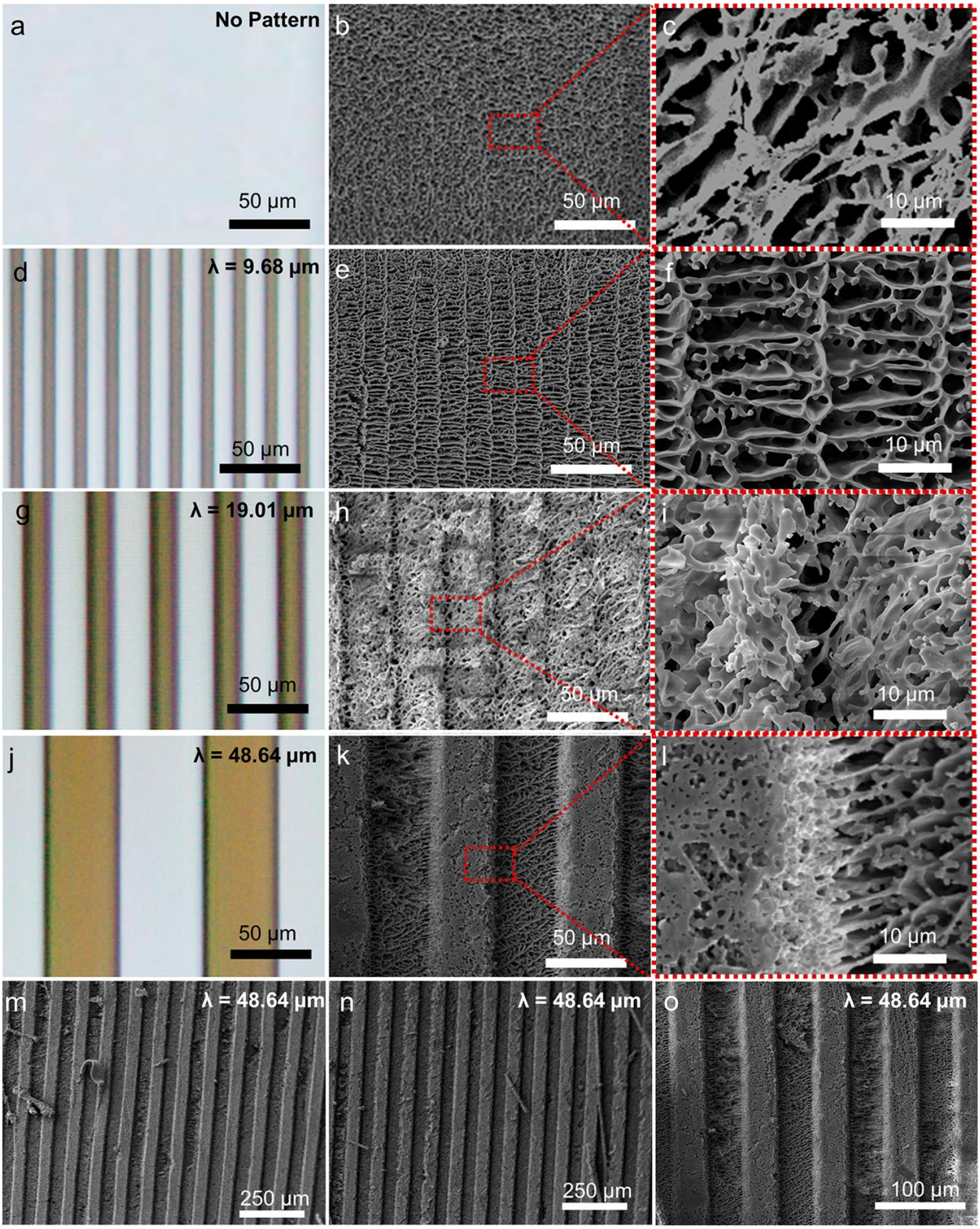

features (Figure 6.3h,i). With λ = 48.64 μm, we obtained a spatial control on the micropore-sized distribution as a replica of the patterned PR features on the Si substrate (Figure 6.3k,l). The border between regions with different pore size was distinct, as it can be seen from the high-magnification SEM image given in Figure 6.3l. We further provided low-magnification SEM images of the λ = 48.64 μm case to show the long-range control on the microstructure of the aerogel surfaces in Figure 6.3m,o.

To demonstrate it as a general method, we also freeze-casted a GO suspension since reduced graphene oxide is one of the most common functional aerogels fabricated by freeze casting. We first fabricated two control specimens, using a Si substrate without any PR features and Si substrates covered with PR (without patterning) using a cold plate temperature of −30°C. As presented in Figure 6.4a,b, the average pore size of the sample fabricated on top of the Si substrate without PR is much finer when compared to the sample fabricated on top of the Si substrate with PR. The average pore size was measured as ∼26 and 6 μm with and without PR cases, respectively (Figure 6.4c). In our experiments with the substrates having patterned features (λ = 48.64 μm), we used two different (−30°C and −70°C) cold plate temperatures to investigate the effect of the freeze temperature on the microstructure. With a cold surface temperature of −30 °C, we have obtained a microporosity as a replica of the patterned PR features as presented in Figure 6.4d. The high magnification SEM images clearly show the difference between the average size of the pores on PR (Figure 6.4e) and Si (Figure 6.4f) surfaces. When we reduced the cold plate temperature to −70°C and repeated the freeze casting procedure using the same GO suspension, we obtained the microstructure provided in Figure 6.4g. The distinction between the regions having different pore-size distribution is as clear as the other cases at −30°C cold plate temperature. Average pore size on the other hand is much smaller in both regions due to the much faster freezing

Figure 6.4. a) SEM image of the GO aerogel freeze casted on Si substrate with a cold plate temperature of −30 °C. b) SEM image of the GO aerogel freeze casted on Si substrate covered with PR layer without any pattern with a cold plate temperature of −30 °C. c) Size distribution of the pores on the aerogel surfaces given in a and b. d−f) SEM images of the GO aerogel freeze casted on Si substrate patterned with PR features (λ = 48.64 μm) with a cold plate temperature of −30 °C. g−i) SEM images of the GO aerogel freeze casted on Si substrate patterned with PR features (λ = 48.64 μm) with a cold plate temperature of −70 °C. j) Average size distribution of the pores on the aerogel surfaces given in d and g.

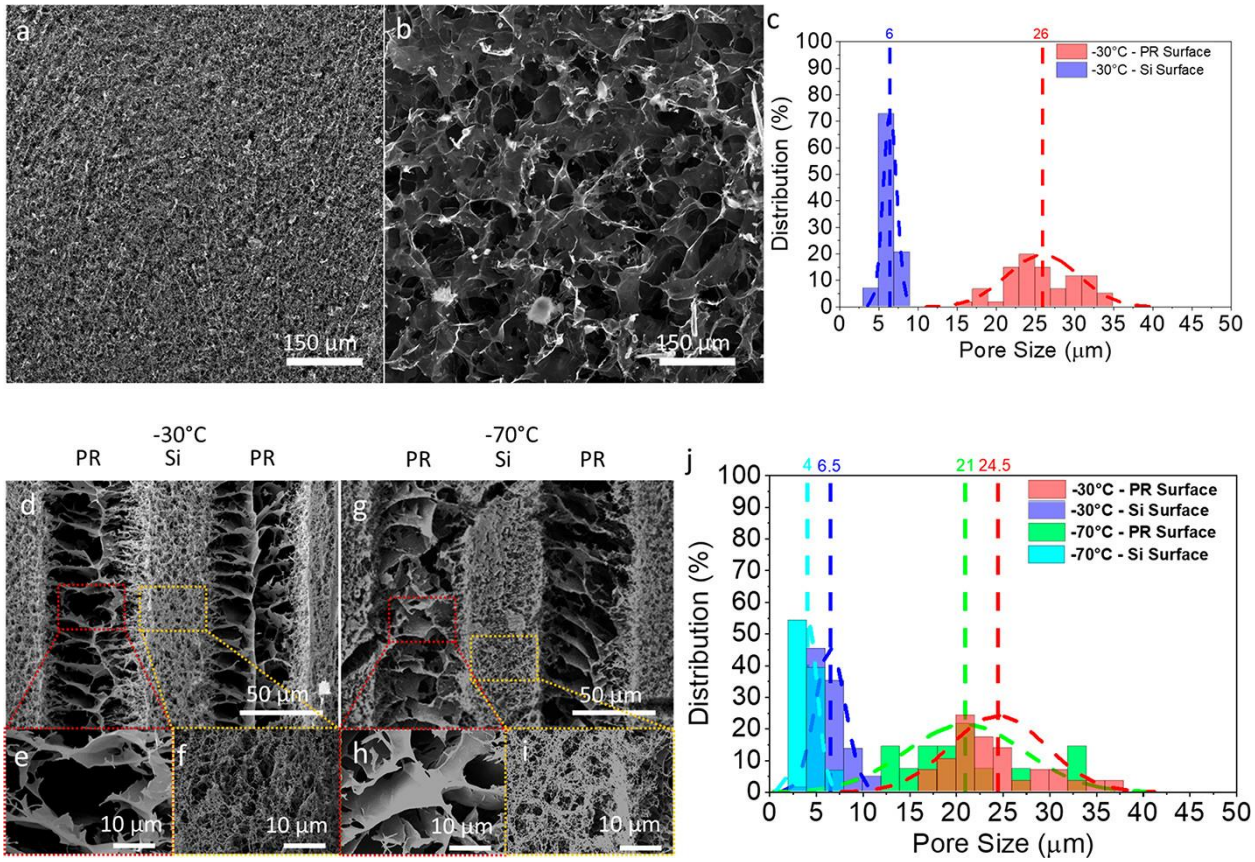

rate. To quantify the difference between −30°C and −70°C cold plate temperature cases, we have used an image-processing software (ImageJ) to help us measure the average size of individual pores. As given in Figure 6.4j, the average size of the pores increased from ~6.5 μm to ~24.5 μm when the substrate surface changed from Si to PR for the cold plate temperature of −30°C. With the lower cold plate temperature (−70°C), average size of the pores for both surfaces was much finer compared to the −30 °C plate due to a much faster freezing rate.[10–12] While the Si surface yielded to an average pore size of ~4 μm, the PR surface resulted in ~21 μm. Measured pore size

Figure 6.5. a) Schematics of the 3D freeze printing process using substrates with patterned PR features. b−d) Low and high-magnification SEM images showing the tailored microstructure of the graphene oxide aerogels fabricated through the 3D freeze printing process using the patterned Si substrate with λ = 48.64 μm.

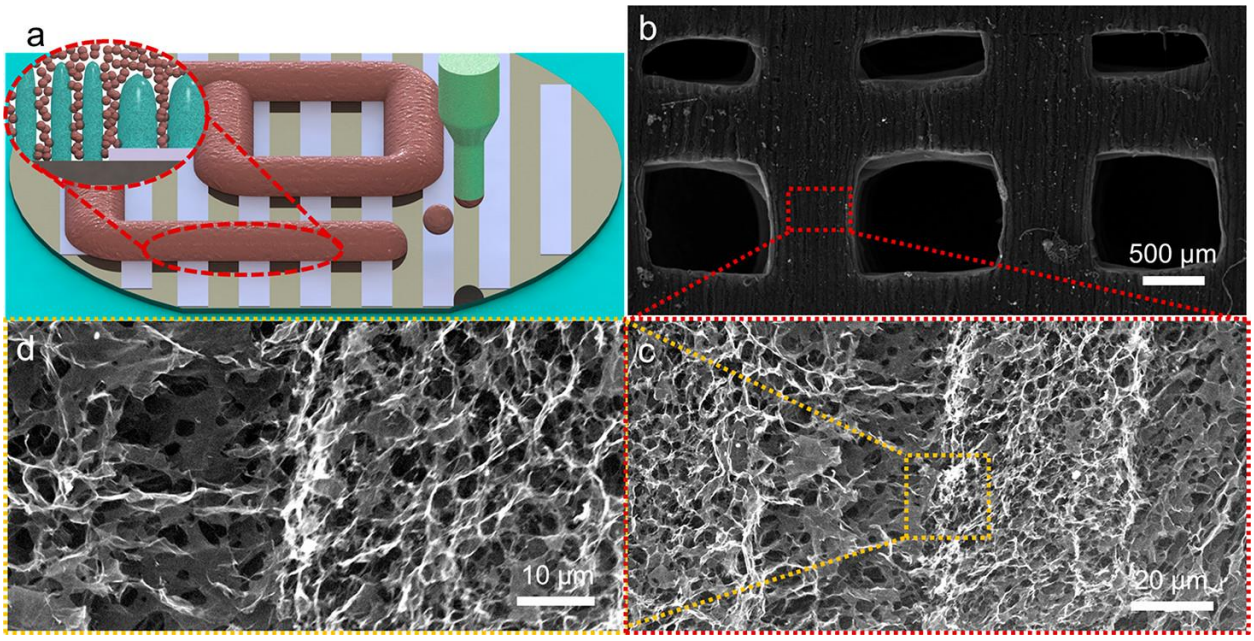

for the −30°C case was also in a good agreement with results provided in Figure 6.4c.

In order to eliminate the dependency of freeze casting method on molds, our group recently developed a 3D freeze printing (3DFP) method, which is a hybrid method composed of unidirectional freeze casting and drop-on-demand (DOD) printing.[22−25] In a 3DFP process, droplets of liquid precursors are generated using a DOD dispenser and are deposited on top of a substrate whose temperature is well below the freezing point of the solvent used in the liquid precursor (Figure 6.5a). As droplets reach the precooled substrate, the solvents experience an immediate freezing, which allows them to preserve their shape. With the reduced distance and time between separate droplets, uniform lines can be obtained after the coalescence.[26] Using these lines, complex 3D frozen structures can be achieved by a mold-free method. Frozen structures with desired shapes are freeze-dried, which sublimates the solvent crystals and a porous aerogel is obtained. Since 3DFP involves freeze casting, the microstructure of the final aerogel can be

manipulated by the freezing kinetics. To further increase the impact of the proposed freeze casting method by increasing the freedom in material design, we investigated the effect of the patterned PR features on the microstructure of 3D freeze printed GO aerogels. For this experiment, we used a 5 mg·mL^{-1} GO suspension along with PR-patterned Si substrates (λ = 48.64 μm) and fabricated scaffolds as presented in Figure 6.5b. With the high-magnification SEM images presented in Figure 6.5c,d, we observed the microstructure of the 3D freeze printed aerogels is also manipulated with the patterned PR features on the Si substrate. As we observed in the previous cases (unidirectional freeze casting using silica and GO-based suspensions), we have seen that due to thermal conductivity on the patterned PR features, the pore size (~15 μm) is much larger than the regions without patterned PR features (~5 μm).

Conclusion

In summary, we used substrates with patterned thermal conductivities to fabricate aerogels with designed surface porosities in terms of size and location of the micropores. The patterned thermal conductivity was obtained as a replica of PR features on the Si substrates deposited by a lithography process. Due to patterned thermal conductivity of the substrates, we obtained a wavy temperature profile above the surface, which manipulated the nucleation and growth of the ice crystals during the freeze casting process. On the surface of the final aerogels, we observed larger ice crystals above the PR surface, while the ice crystals were much smaller above the Si surface. The aerogels fabricated through our method exhibited a designed surface micropore morphology, in which size and location of the pores can be determined by the user. Our experiments with the 3D freeze printing method also showed that substrates with varying thermal conductivities can be further implemented to a 3D printing processes based on a freeze casting method to fabricate aerogels with custom macro and microstructures. We think that by further improving/optimizing

thermal conductivity patterns on the substrates, the control on the microstructure morphology on the aerogel surface can be extended to 3D.

References

[1] Du, A.; Zhou, B.; Zhang, Z.; Shen, J. A special material or a new state of matter: a review and reconsideration of the aerogel. Materials 2013, 6 (3), 941−968.

[2] Jimenez-Saelices, C.; Seantier, B.; Cathala, B.; Grohens, Y. Effect of freeze-drying parameters on the microstructure and thermal insulating properties of nanofibrillated cellulose aerogels. J. Sol-Gel Sci. Technol. 2017, 84 (3), 475−485.

[3] Yan, L.; Wu, J.; Zhang, L.; Liu, X.; Zhou, K.; Su, B. Pore structures and mechanical properties of porous titanium scaffolds by bidirectional freeze casting. Mater. Sci. Eng., C 2017, 75, 335−340.

[4] Wu, S.; Ladani, R. B.; Zhang, J.; Ghorbani, K.; Zhang, X.; Mouritz, A. P.; Kinloch, A. J.; Wang, C. H. Strain sensors with adjustable sensitivity by tailoring the microstructure of graphene aerogel/PDMS nanocomposites. ACS Appl. Mater. Interfaces 2016, 8 (37), 24853−24861.

[5] Weigold, L.; Mohite, D. P.; Mahadik-Khanolkar, S.; Leventis, N.; Reichenauer, G. Correlation of microstructure and thermal conductivity in nanoporous solids: the case of polyurea aerogels synthesized from an aliphatic tri-isocyanate and water. J. Non-Cryst. Solids 2013, 368, 105−111.

[6] Zhu, X.; Yang, C.; Wu, P.; Ma, Z.; Shang, Y.; Bai, G.; Liu, X.; Chang, G.; Li, N.; Dai, J. Precise control of versatile microstructure and properties of graphene aerogel via freezing manipulation. Nanoscale 2020, 12 (8), 4882−4894.

[7] Twej, W. A.; Alattar, A. M.; Drexler, M.; Alamgir, F. M. Tuned optical transmittance in single-step-derived silica aerogels through pH-controlled microstructure. Int. Nano Lett. 2017, 7 (4), 257−265.

[8] Li, T.; Zhou, B.; Du, A.; Xiang, Y.; Wu, S.; Liu, M.; Ding, W.; Shen, J.; Zhang, Z. Microstructure control of the silica aerogels via pinhole drying. J. Sol-Gel Sci. Technol. 2017, 84 (1), 96−103.

[9] Li, C.-B.; Li, Y.-J.; Zhao, Q.; Luo, Y.; Yang, G.-Y.; Hu, Y.; Jiang, J.-J. Electromagnetic Interference Shielding of Graphene Aerogel with Layered Microstructure Fabricated via Mechanical Compression. ACS Appl. Mater. Interfaces 2020, 12 (27), 30686−30694.

[10] Nelson, I.; Naleway, S. E. Intrinsic and extrinsic control of freeze casting. J. Mater. Res. Technol. 2019, 8 (2), 2372−2385.

[11] Li, W.; Lu, K.; Walz, J. Freeze casting of porous materials: review of critical factors in microstructure evolution. Int. Mater. Rev. 2012, 57 (1), 37−60.

[12] Scotti, K. L.; Dunand, D. C. Freeze casting-A review of processing, microstructure and properties via the open data repository, Freeze Casting. Prog. Mater. Sci. 2018, 94, 243−305.

[13] Liu, R.; Xu, T.; Wang, C.-A. A review of fabrication strategies and applications of porous ceramics prepared by freeze-casting method. Ceram. Int. 2016, 42 (2), 2907−2925.

[14] Fang, F.; Zhang, N.; Guo, D.; Ehmann, K.; Cheung, B.; Liu, K.; Yamamura, K. Towards atomic and close-to-atomic scale manufacturing. International Journal of Extreme Manufacturing 2019, 1 (1), 012001.

[15] Fang, F. Atomic and close-to-atomic scale manufacturing: perspectives and measures. International Journal of Extreme Manufacturing 2020, 2 (3), 030201.

[16] Lee, H.; Jang, T.-S.; Song, J.; Kim, H.-E.; Jung, H.-D. The production of porous hydroxyapatite scaffolds with graded porosity by sequential freeze-casting. Materials 2017, 10 (4), 367.

[17] Tang, Y.; Zhao, K.; Hu, L.; Wu, Z. Two-step freeze casting fabrication of hydroxyapatite porous scaffolds with bionic bone graded structure. Ceram. Int. 2013, 39 (8), 9703−9707.

[18] Ogden, T. A.; Prisbrey, M.; Nelson, I.; Raeymaekers, B.; Naleway, S. E. Ultrasound freeze casting: Fabricating bioinspired porous scaffolds through combining freeze casting and ultrasound directed self-assembly. Mater. Des. 2019, 164, 107561.

[19] Yang, M.; Wu, J.; Bai, H.; Xie, T.; Zhao, Q.; Wong, T. W. Controlling three-dimensional ice template via two-dimensional surface wetting. AIChE J. 2016, 62 (12), 4186−4192.

[20] Zhao, J.; Li, Y.; Wu, Y.; Lv, S.; Lu, K. Microstructure of TiO2 porous ceramics by freeze casting of nanoparticle suspensions. Ceram. Int. 2017, 43 (17), 14593−14598.

[21] Shokralla, S. A.; Al-Muaikel, N. S. Thermal properties of epoxy (DGEBA)/phenolic resin (NOVOLAC) blends. Arabian Journal for Science and Engineering 2010, 35 (1B), 7−14.

[22] Zhang, Q.; Zhang, F.; Medarametla, S. P.; Li, H.; Zhou, C.; Lin, D. 3D printing of graphene aerogels. Small 2016, 12 (13), 1702− 1708.

[23] Yan, P.; Brown, E.; Su, Q.; Li, J.; Wang, J.; Xu, C.; Zhou, C.; Lin, D. 3D printing hierarchical silver nanowire aerogel with highly compressive resilience and tensile elongation through tunable poisson's ratio. Small 2017, 13 (38), 1701756.

[24] Ma, C.; Wang, R.; Tetik, H.; Gao, S.; Wu, M.; Tang, Z.; Lin, D.; Ding, D.; Wu, W. Hybrid nanomanufacturing of mixed-dimensional manganese oxide/graphene aerogel macroporous hierarchy for ultralight efficient supercapacitor electrodes in self-powered ubiquitous nanosystems. Nano Energy 2019, 66, 104124.

[25] Brown, E.; Yan, P.; Tekik, H.; Elangovan, A.; Wang, J.; Lin, D.; Li, J. 3D printing of hybrid MoS2-graphene aerogels as highly porous electrode materials for sodium ion battery anodes. Mater. Des. 2019, 170, 107689.

[26] Tetik, H.; Yang, G.; Tan, W.; Fong, A.; Lei, S.; Weker, J. N.; Lin, D. High Speed In-situ X-Ray Imaging of 3D Freeze Printing of Aerogels. Additive Manufacturing 2020, 36, 101513.

Chapter 7 - Conclusions

In this dissertation, 3D Freeze Printing Method has been systematically studied for realization of functional aerogel where the microstructure as well as the macrostructure of the constructs can be precisely engineered. To achieve this goal, a highly customized and open-source additive manufacturing setup was designed and developed. Following, an *in-situ* process investigation study was performed using the sophisticated high-speed X-ray imaging facilities of the SLAC National Lab at Stanford University. This investigation provided quality information on the phase change of the deposited materials at different scales (e.g. single droplets, uniform lines, consecutive layers) and how the process parameters affect the final product quality. With the obtained information, aerogels based on cellulose nanocrystals and $Ti_3C_2T_x$ MXene have been fabricated. Due to the low melting point of cellulose and high oxidation tendency of MXenes, it has always been a great challenge to obtain aerogels with highly irregular geometries with overhang features. By using water as a support material that can be removed from the constructs by normally applied freeze-drying step, aerogels with overhang features have been achieved, and the effects of the microstructure on the physical properties (e.g. mechanical compressibility, compressive strength, electrical conductivity) have been investigated. Cellulose nanocrystal aerogels have been functionalized by different additives in the ink formulation: Polyamide-epichlorohydrin resin for cross-linked aerogels to obtain wet stability in applications such as biomedical, selective liquid absorption, and etc.; Poly (3,4-ethylenedioxythiophene): poly (styrene sulfonate) for providing electrical conductivity for piezoresistive sensing and flexible electronics. MXene aerogels already had functionality based on their high electrical conductivities. 3D freeze printed MXene aerogels have been evaluated for their piezoresistive sensing capabilities. Further, composites based on 3D printed MXene aerogels and Poly(dimethylsiloxane) elastomer have been

fabricated, where the elastomer provided a packaging and the aerogel, functionality. Those composites showed a great promise for flexible and wearable electronics. Then, all printed microsupercapacitor devices based on $Ti_3C_2T_x$ MXene were fabricated, and the alignment of the MXene sheets in the microstructure was precisely engineered to boost the energy storage performance. Finally, by creating local thermal gradients, a novel approach was developed to achieve a control over the rate of freezing in the freeze casting and 3DFP processes. This method allowed realization of aerogels having non-monolithic microstructures where the location of the pores having different dimensions can be precisely tuned. Even though the achieved control over the porosity remained only in the surface of the aerogels, it is a very promising approach for fabricating 3D aerogels that can mimic the structure of the bone for bone tissue engineering applications, or having a designed absorption behavior for selective absorption applications.

Compared to the other 3D printing methods used for fabricating aerogels, 3DFP offers a lot in terms of flexibility in design, simultaneous control over the macro and microstructure, and enhanced bonding in between adjacent layers. This method also has a great potential to boost the range of the materials, which have been a limiting factor in the field of additive manufacturing of aerogels due to printability requirements. Introducing novel materials would potentially increase the performance in the already existing application or introduce novel applications to the field. Especially ceramic and metal based nanomaterials need to be explored for the field since the aerogels based on those materials have shown great potential with conventional fabrication methods. Another challenge within the field, is the extreme pressure and temperature conditions required for the collapse-free drying. This issue is the most important limiting factor staying in between the commercialization of the aerogels, and several research groups have been investigating the possibilities for ambient condition drying of aerogels. Nevertheless, those efforts

are mostly specific to a certain material, and same approach which works for one material cannot be applied for another. Especially for 3D printed aerogel where the fast fabrication of complex and accurate constructs based on different materials can be achieved, a systematic drying approach that will work for different materials will be greatly appreciated.

Appendix A - Supporting Information for Chapter 5[6]

Figure A.1. a) AFM image of a MXene sheet. b) XRD pattern of the 3D freeze printed MXene aerogels.

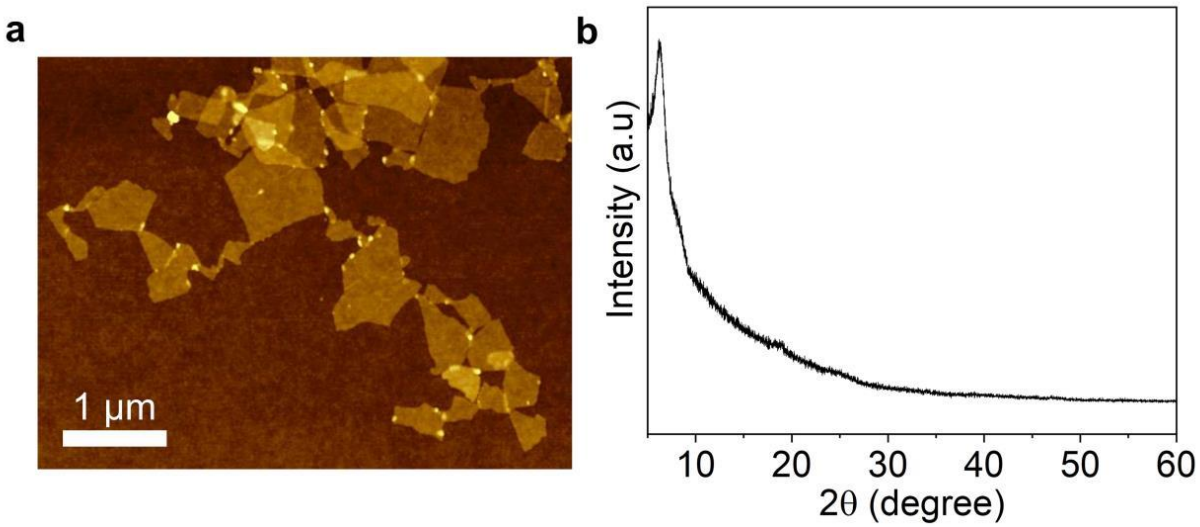

Figure A.2. Stroboscopic images showing the phases of satellite-free droplet generation

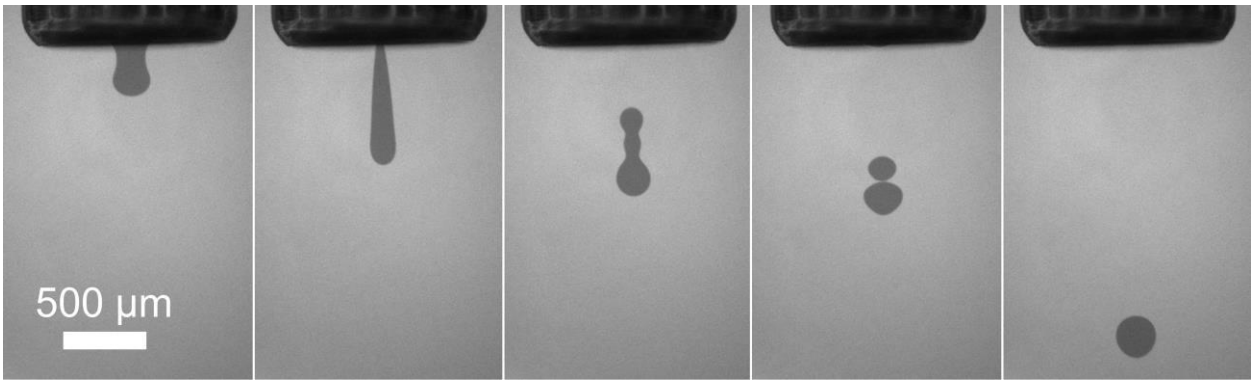

[6] Reprinted with permission from "3D Printed MXene Aerogels with Truly 3D Macrostructure and Highly Engineered Microstructure for Enhanced Electrical and Electrochemical Performance" by Halil Tetik, Jafar Orangi, Guang Yang, Keren Zhao, Shakir Bin Mujib, Gurpreet Singh, Majid Beidaghi, and Dong Lin, 2021. Advanced Materials, 34, 2104980. 2021 Wiley-VCH GmbH

Figure A.3. Schematics of the MXene synthesis and 3D freeze printing process for fabricating truly 3D structures with overhang features

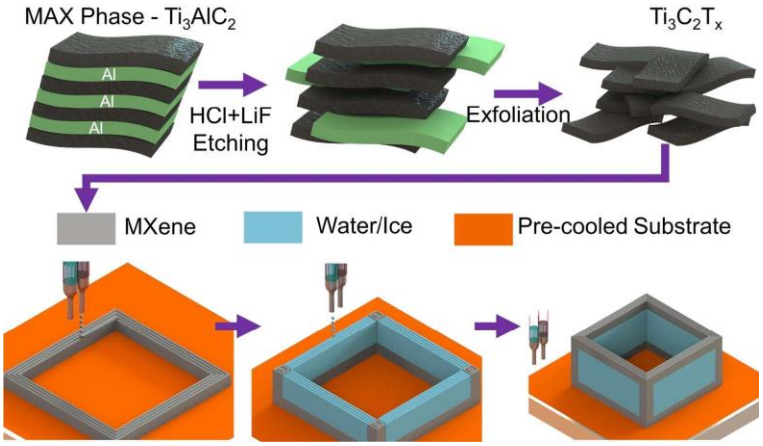

Figure A.4. Retention of max stress during 50 loading-unloading cycles up to 10% strain (ρ = 15.69 mg cm^{-3})

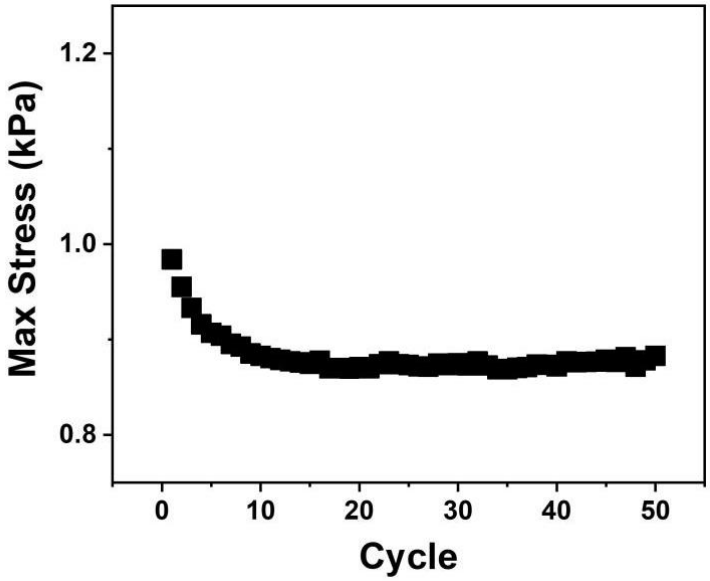

Figure A.5. 3D freeze printed super capacitor devices printed on a) paper, b) acetate film, c) glass slide, and d) acrylic sheet substrates.

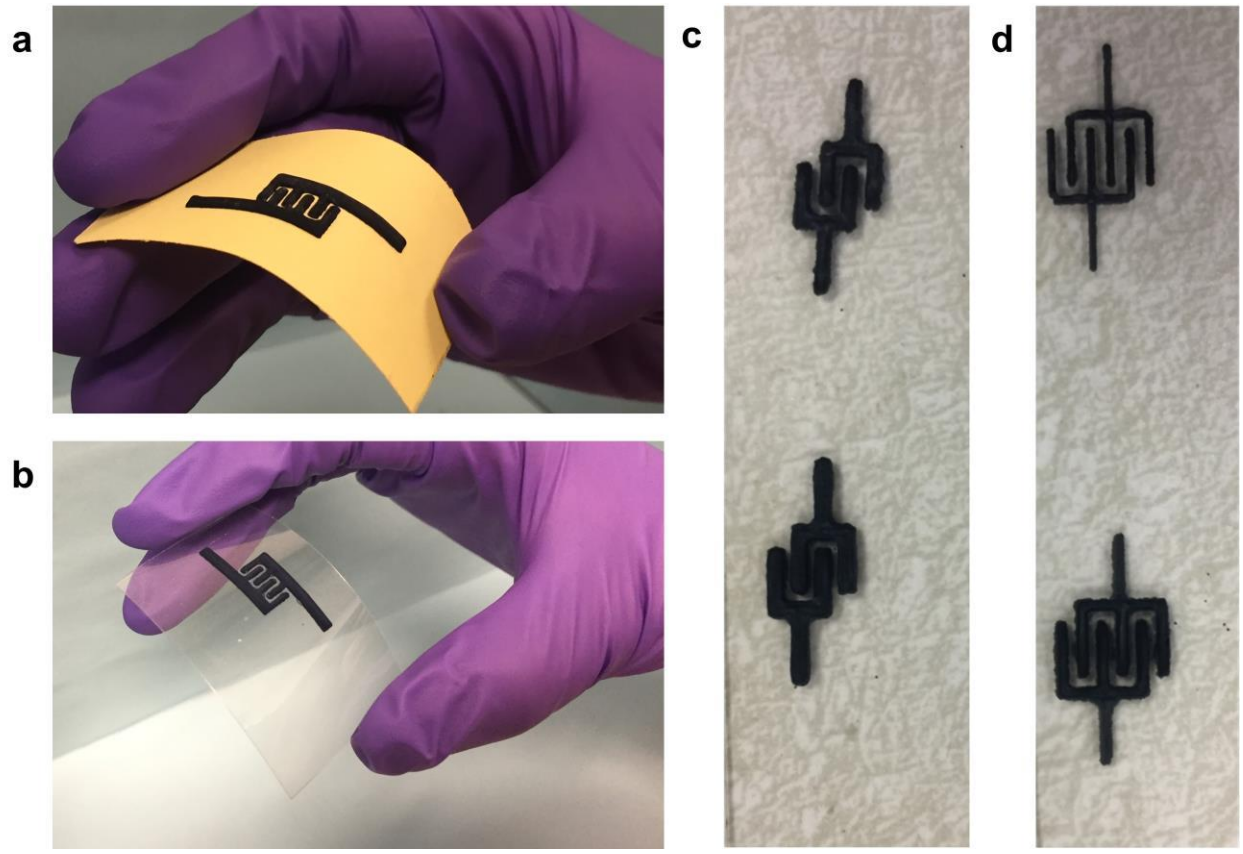

Figure A.6. Average dimensions of the line width, finger distance, and height for different amount of deposited layers

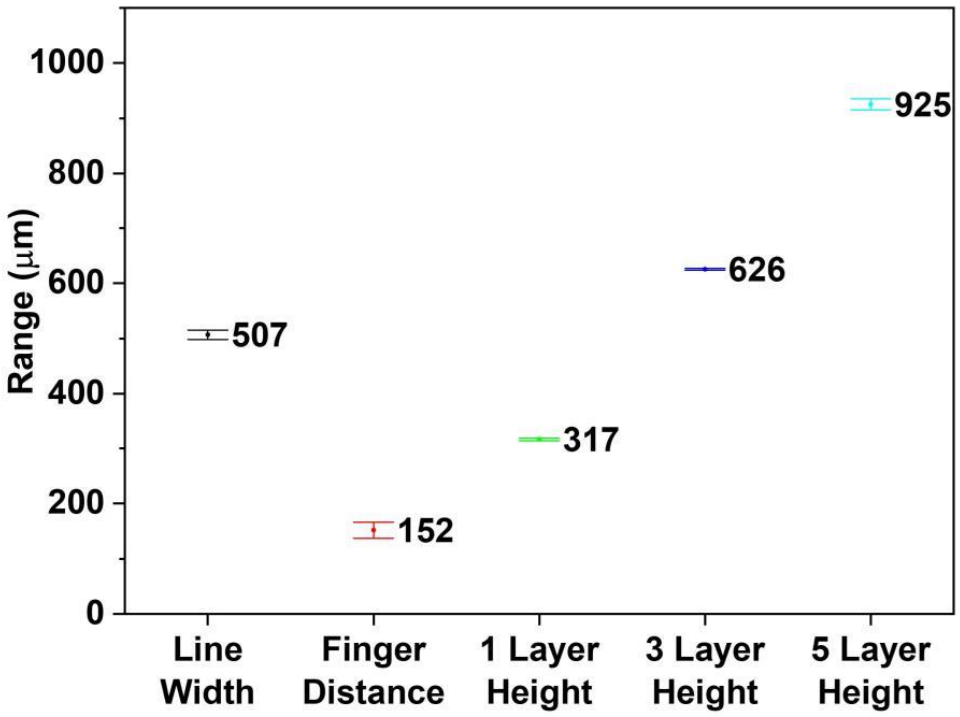

Figure A.7. SEM images showing the ordered microstructure of the 3D printed MSCs.

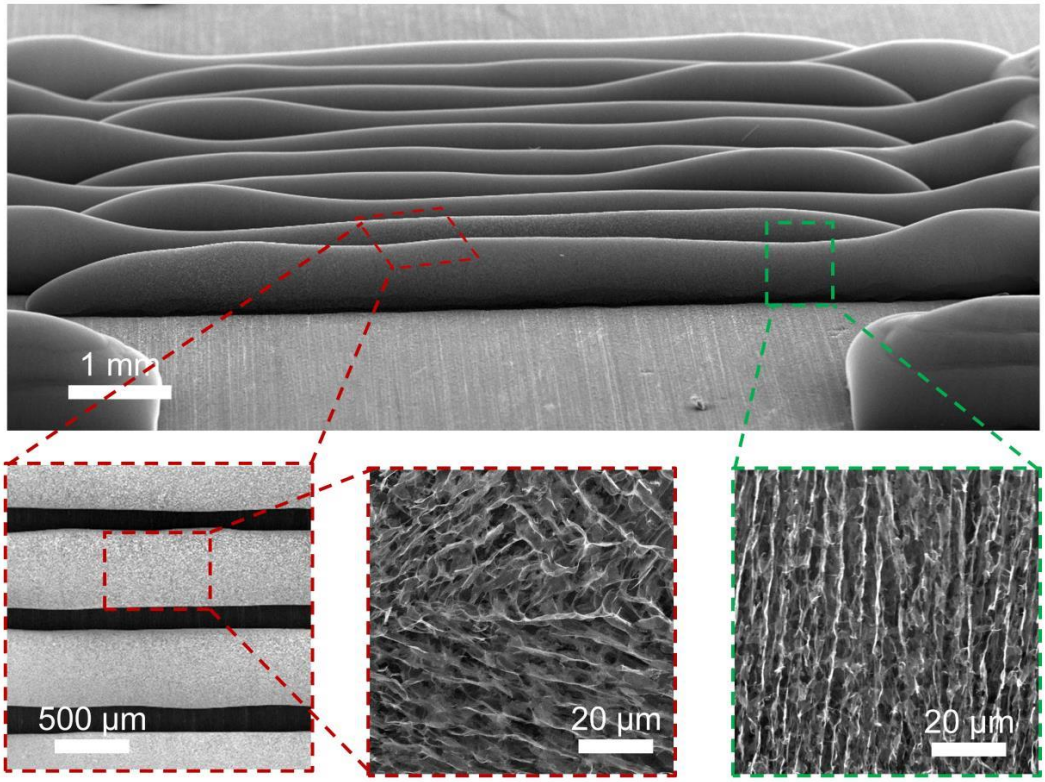

Figure A.8. Geometry of 3D freeze printed MSCs with highly-ordered, anisotropic microstructure.

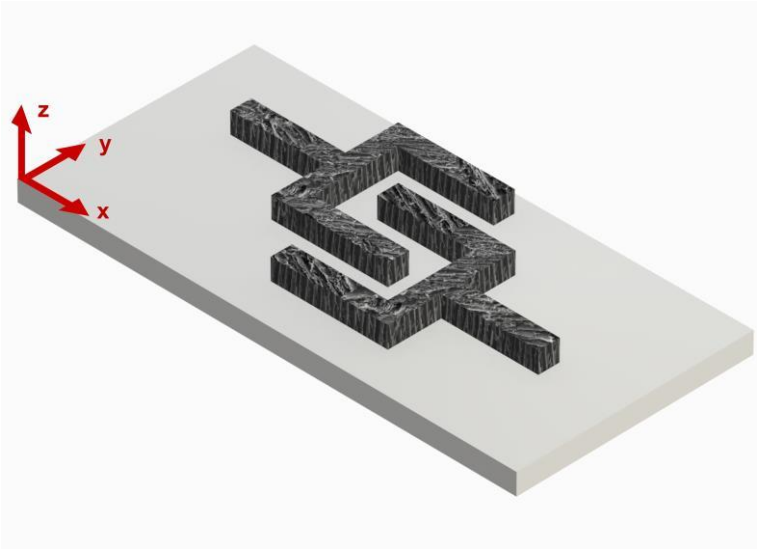

Figure A.9. Inkjet-based printing of a current collector layer which dries in ambient conditions, and 3DFP of porous electrode on top of the current collector layer

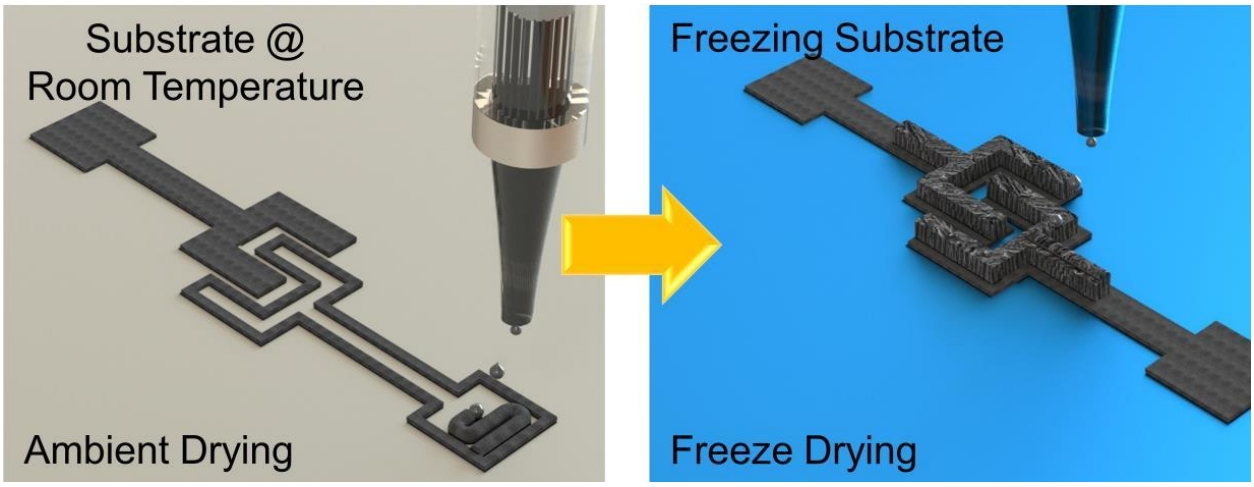

Figure A.10. Macro and microstructure of the MSCs composed of MXene sheets with hybrid alignment (horizontal for current collector and vertical for porous electrode).

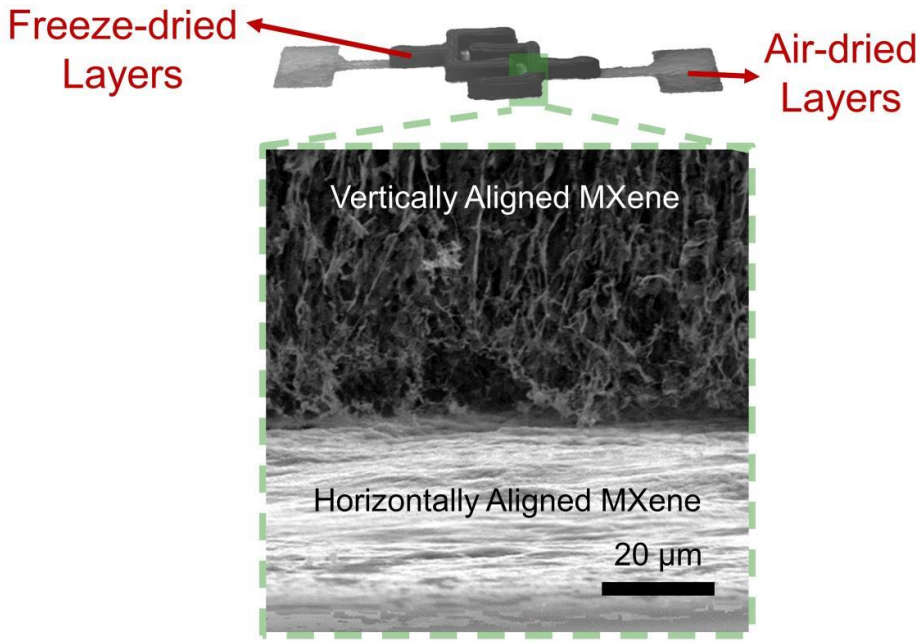

Figure A.11. a) CV curves at 50 mV s^{-1} and b) EIS tests results of the 3V MSCs printed on paper substrate at different bending angles.

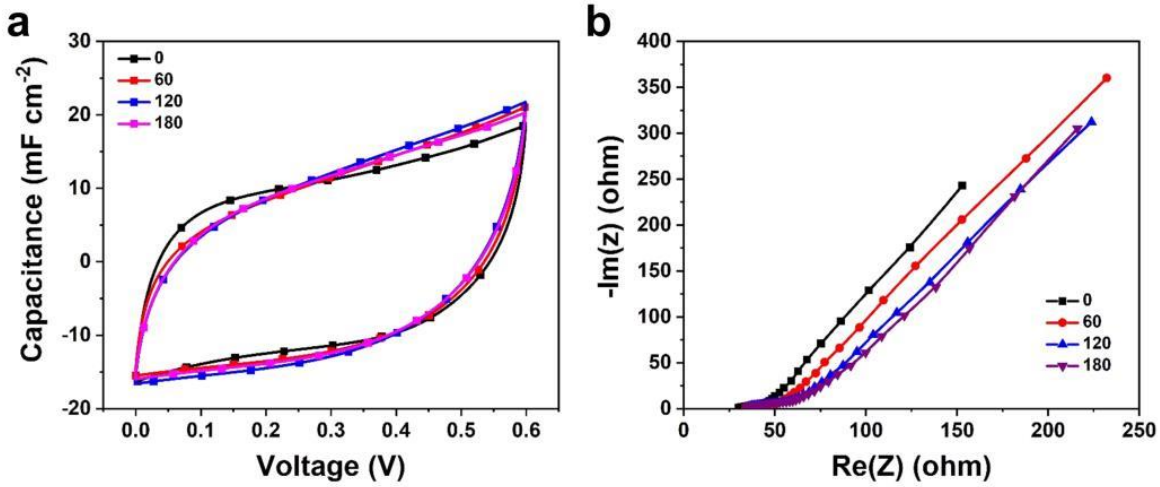

Figure A.12. CV curves of 3H and 1H-3V MSC devices at 10 mv s^{-1}.

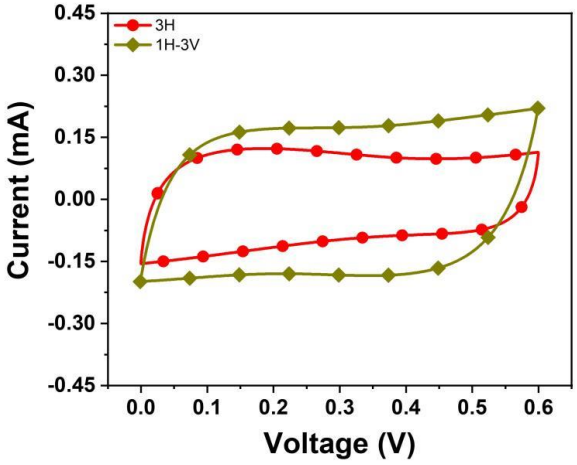

Figure A.13. Charge storage mechanism of the MSCs composed of MXene sheets with hybrid alignment (horizontal for current collector and vertical for porous electrode). The horizontal alignment of the MXene sheets facilitates electron transport, and vertically aligned MXenes provide enhanced ion accessibility and fast ion transport.

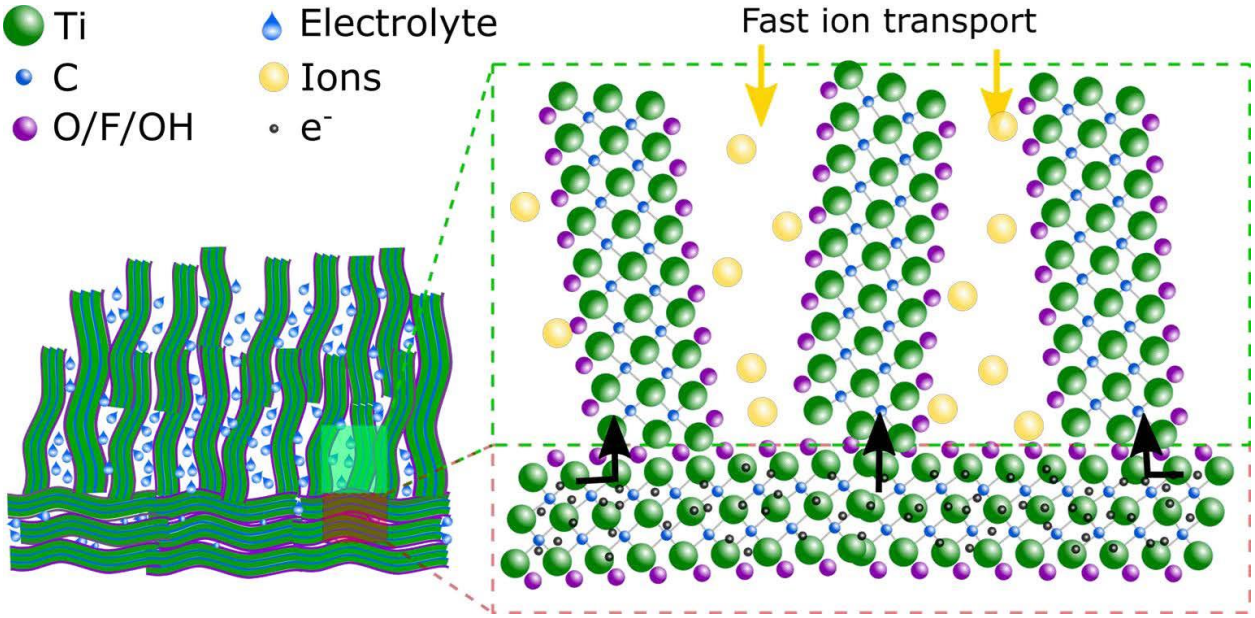

Figure A.14. Cycling stability of 1V-3H MSC device at 20 mV s^{-1}. Over 90% capacity retention of the printed device after 10000 cycles.

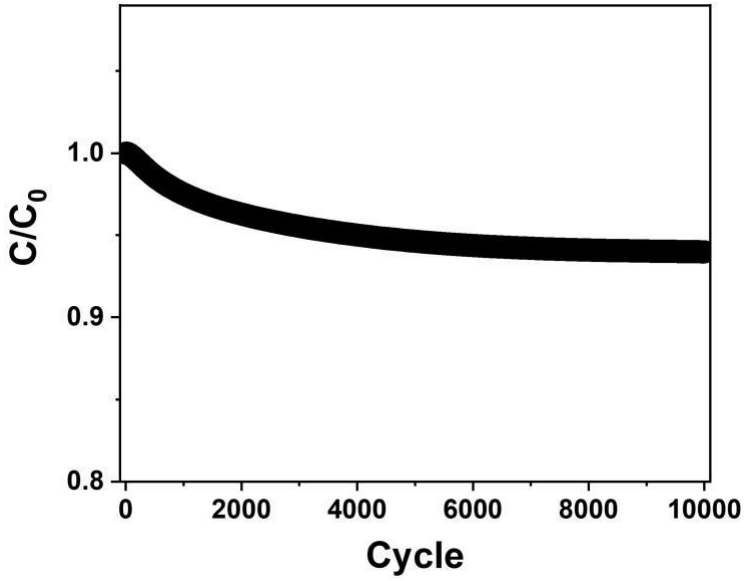

Figure A.15. Comparison of the areal capacitance performance of the 3D printed pristine MXene supercapacitor devices considering the concentration of the used inks.

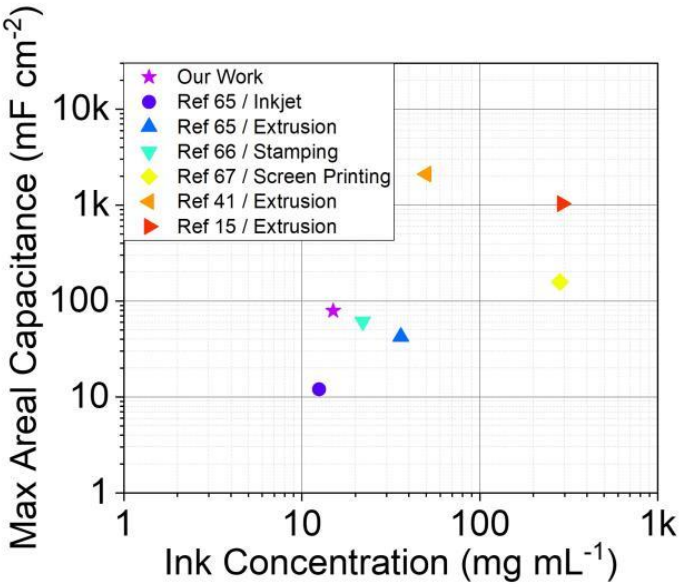

Figure A.16. The EIS test result for the MSC-1V.

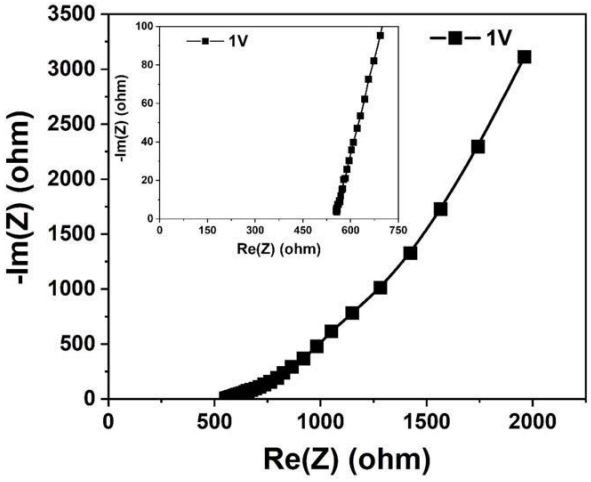

Table A.1. Comparison of the electrochemical performance of MXene based MSC fabricated with different fabrication methods.

Material	Fabrication Method	Electrolyte	Test Condition	Performance	Energy Density	Power Density	Ref.
$Ti_3C_2T_x$	Clay-like MXene laser scribing	PVA/ H_2SO_4	-	25	46.6	0.77	[69]
$Ti_3C_2T_z$	Template, VAF	3 M H_2SO_4	10 mV s^{-1}	310 F g^{-1}	NA	NA	[60]
$Ti_3C_2T_z$ /rGO	Self-assembly, VAF	1 M H_2SO_4	2 mV s^{-1}	254 F g^{-1}	NA	NA	[70]
$Ti_3C_2T_z$/rGO	VAF, cast	2 M KOH	2 A g^{-1}	154.3 F g^{-1}	NA	NA	[71]
$Ti_3C_2T_x$/ rGO	Composite aerogel	PVA/ H_2SO_4	1 mV s^{-1}	34.6	0.18	2.2	[72]
$Ti_3C_2T_x$/ CNT	Spray coated layer by layer	1M H_2SO_4	10 mV s^{-1}	80	-	-	[73]
$Ti_3C_2T_x$	Writing with Pen	PVA/ H_2SO_4	-	5	-	-	[74]
$Ti_3C_2T_x$	Stamped film	PVA/ H_2SO_4	25 µA cm^{-2}	61	0.33	0.76	[65]
$Ti_3C_2T_z$	Inkjet	PVA/ H_2SO_4	4 µA cm^{-2}	12 mF cm^{-2}	NA	NA	[64]
N-$Ti_3C_2T_z$	Screen	PVA/ H_2SO_4	10 mV s^{-1}	70.1 mF cm^{-2}	NA	NA	[75]
$Ti_3C_2T_z$/ AgNWs/ $RuO_2.xH_2O$	Screen	PVA/ KOH	1 mV s^{-1}	864.2 F cm^{-3}	13.5 mWh cm^{-3}	48.5 W cm^{-3}	[76]
$Ti_3C_2T_z$	Extrusion	PVA/ H_2SO_4	2 mV s^{-1}	1035 mF cm^{-2}	51.7 µWh cm^{-2}	5.7 µW cm^{-2}	[14]
$Ti_3C_2T_z$	Extrusion	PVA/ H_2SO_4	5 µA cm^{-2}	43 mF cm^{-2}	0.32 µWh cm^{-2}	11.4 mW cm^{-2}	[64]
$Ti_3C_2T_z$/ SWCNT	Duplex	PVA/ H_3PO_4	25 µA cm^{-2}	30.76 mF cm^{-2}	8.37 µWh cm^{-2}	17.31 µW cm^{-2}	[77]
$Ti_3C_2T_x$/ CNT	Printed	PVA/ H_3PO_4	25 µA cm^{-2}	30.76	17.31	8.37	[77]
$Ti_3C_2T_z$ - 1H-5	3DFP	PVA/ H_2SO_4	2 mV s^{-1}	79 mF cm^{-2}	3.9 µWh cm^{-2}	0.05 mW cm^{-2}	This work
$Ti_3C_2T_z$- 2H-1V	3DFP	PVA/ H_2SO_4	2 mV s^{-1}	200 F g^{-1}	NA	NA	This work